Numerical computations of pressurized liquefied gas releases into the atmosphere

Mathieu Ichard

Dissertation for the degree of Philosophiae Doctor (PhD)

Department of Physics and Technology
University of Bergen

February 2012

Abstract

There is great concern about accidental releases and dispersion of toxic and flammable industrial chemicals into the atmosphere. Their toxic effects and/or flammable properties, combined with their widespread use and transport through urban areas, make most industrial chemicals very dangerous. Many industrial chemicals are transported and stored as pressurized liquefied gases in large quantities. The chemical, petrochemical and petroleum industries, as well as regulatory agencies, need realistic dispersion simulations for risk analysis purposes.

If accidentally released into the atmosphere, a pressurized liquefied gas suffers a rapid de-pressurisation and as a consequence boils violently. This process is referred to as the flashing process. Complete flashing results in the formation of a two-phase jet with high momentum. Some of the droplets may deposit on the ground and form a pool which gradually evaporates. This thesis presents the development of a Computational Fluid Dynamics (CFD) methodology for studies of pressurized liquefied gas releases into the atmosphere. The methodology is implemented in the CFD model FLACS.

The performances of existing source term models in predicting recent experimental observations are assessed. It is found that the energy balance model gives the best predictions for the mass flow rate at the exit orifice. Uncertainties are present in the quality of the predictions for the size distribution of droplets and it is recommended to perform sensitivity studies. Investigation of the dispersion of heavy particles in isotropic turbulent flows by means of the Kinematic Simulation approach allows emphasizing the importance of the inertia and crossing trajectory effects. An Euler-Euler approach based on the assumption of homogeneous flow, namely the Homogeneous Equilibrium Model (HEM), and an Euler-Lagrange approach are implemented in the FLACS CFD model in order to simulate two-phase flows. The two-phase flow models are validated against laboratory scale experiments. Improvements of the current FLACS models for liquid spreading and evaporation on the ground are developed and an algorithm is implemented in order to solve the equations of the pool model on a user-defined uniform grid.

Obstructed and non-obstructed large-scale experiments are simulated with the new methodology. The validation of the methodology with both the HEM and the Euler-Lagrange approaches is shown to be relatively successful. Its simplicity of use makes the HEM approach very attractive for industrial applications. The Euler-Lagrange approach has a wider range of physical applications and provides more options to characterize the dispersed phase and its interaction with the continuous phase. This approach should be used when the HEM approach reaches its limitations.

Acknowledgements

I am very grateful for the three-year Næring PhD grant I received from the Research Council of Norway.

I would like to thank my two supervisors Bjørn Johan Arntzen and Jens Andreas Melheim for their support and advices. I appreciate the freedom I have been given in my work. I would also like to thank Olav Roald Hansen, Trygve Skjold, Idar Storvik and Filippo Gavelli for their patience, availability and valuable inputs. Thanks are also due to all my colleagues at GexCon for their kindness and all the nice Julebord and kick-off parties !

Thanks are also due to all the "Bergen-les-bains" team for their moral support all along the thesis. Those four years have been rich in all kind of events.

Finally I want to thank my parents, my brother and my grand-parents for their continual support, love and help ! Merci beaucoup !

Bergen, February 2012
Mathieu Ichard

Contents

Abstract i

Acknowledgements iii

1 Introduction 1
- 1.1 Motivation and scope of work 1
- 1.2 About the FLACS model 3
- 1.3 Previous work and the current contribution 5
  - 1.3.1 Previous work 5
  - 1.3.2 Current contribution 6
- 1.4 Organisation of the thesis 7

2 An introduction to flashing liquids releases 9
- 2.1 The physics of flashing releases 9
  - 2.1.1 Theory of flashing liquids 9
  - 2.1.2 Description of a flashing release 10
- 2.2 Experimental observations 12
  - 2.2.1 The Von-Karman Institute tests 12
  - 2.2.2 The FLIE-INERIS tests 13
  - 2.2.3 The CCPS tests 14
  - 2.2.4 The Desert Tortoise tests 15
- 2.3 The current FLACS approach 15

3 Models for the source term of flashing jets 17
- 3.1 Mass flow rate and jet expansion 17
  - 3.1.1 Overview 17
  - 3.1.2 The Bernoulli approach 18
  - 3.1.3 The energy balance model 18
  - 3.1.4 The homogeneous non-equilibrium model 19
  - 3.1.5 The control volume model for the expansion region 20
  - 3.1.6 The model of Moreira *et al.* 21
  - 3.1.7 Inter-model comparison 22
- 3.2 Spray characteristics 25
  - 3.2.1 Overview 25
  - 3.2.2 The CCPS model 26
  - 3.2.3 The correlation of Witlox *et al.* 27

3.2.4 The CCPS correlation 28
3.2.5 The model recommended in the Yellow Book 29
3.2.6 Inter-model comparison 29
3.3 Comparisons with experimental data 30
3.3.1 Mass flow rate 30
3.3.2 Spray characteristics and expansion region 33
3.3.3 Conclusions 37

4 Single phase turbulent jet flows 39
4.1 Turbulent flow modelling in the FLACS model 39
4.1.1 Presentation of the FLACS CFD solver 39
4.1.2 A brief introduction to turbulence theory 39
4.1.3 The $k-\varepsilon$ turbulence model 42
4.2 Theory of single-phase turbulent jet flows 43
4.2.1 Neutrally buoyant jet flows 43
4.2.2 Variable density jet flows 47
4.3 Simulations of free round jets with the FLACS model 48
4.3.1 Neutrally buoyant jet flows 48
4.3.2 Variable density jet flows 50
4.4 Conclusions 52

5 Two-phase turbulent jet flows: the Euler-Lagrange approach 55
5.1 Classification of models 55
5.2 Particle phase equations 57
5.2.1 The particle momentum equation and its simplification 57
5.2.2 Background on Stochastic Differential Equations 59
5.2.3 Model for the seen instantaneous fluid velocity 62
5.2.4 Vaporization of liquid droplets 63
5.3 Source terms in the continuous phase equations 67
5.3.1 Two-way coupling through mass, momentum and energy 68
5.3.2 Turbulence modulation 68
5.4 Algorithm of the Euler-Lagrange approach 69
5.5 Validation with laboratory scale experiments 70
5.5.1 The experiments of Hardalupas *et al.* 70
5.5.2 The experiments of Sheen *et al.* 74
5.5.3 The experiments of McDonell *et al.* 77
5.6 Conclusions 81

6 Two-phase turbulent jet flows: the HEM approach 87
6.1 Description of the HEM approach 87
6.1.1 Overview 87
6.1.2 Implementation inside the FLACS code 88
6.2 Simulation of the McDonell *et al.* experiments 89
6.3 Estimation of liquid deposition in the HEM approach 92
6.3.1 Proposition of a model 92
6.3.2 Spread and vaporization of liquid on the ground 93
6.4 Conclusions 96

7 Simulations of atmospheric releases of pressurized liquefied gases 97
7.1 The atmospheric boundary layer 97
7.1.1 Introduction to atmospheric turbulence 97
7.1.2 Modelling of atmospheric turbulence in the FLACS model . . . 99
7.2 The CCPS experiments 101
7.3 The FLIE-INERIS experiments 104
7.4 The Desert Tortoise experiments 106
7.5 The Falcon experiments 114
7.6 Application to consulting projects 119
7.7 Conclusions 120

8 Conclusions and further work 121
8.1 Conclusions 121
8.2 Further work 122

A Paper I 137
A.1 Dispersion of heavy particles in turbulent-like flows 137

B Paper II 147
B.1 Validation of CFD modelling of LH_2 spread and evaporation against large-scale spill experiments 147

Nomenclature

Greek Letters

α	Gas volume fraction	-
ε	Turbulent dissipation rate	m^2/s^3
η	Ratio of orifice pressure and storage pressure	-
γ	Thermal diffusivity	m^2/s
κ	Von-Karman constant $\kappa = 0.42$	-
λ	Thermal conductivity	W/m.K
μ	Dynamic viscosity	kg/m.s
ν	Specific volume	m^3/kg
ρ	Density	kg/m^3
σ	Surface tension for a liquid	N/m
σ_0	Standard deviation of the log-normal distribution	-
τ_p	Particle relaxation time	s

Latin Letters

A	Area	m^2
B_M	Spalding mass transfer number	-
B_T	Spalding heat transfer number	-
c	Speed of sound in homogeneous two-phase mixture	m/s
C_D	Discharge coefficient	-
C_D	Drag coefficient for particles	-
C_p	Specific heat at constant pressure	J/kg.K
$\mathcal{D}$	Mass diffusivity	m^2/s
D/d	Diameter	m

f	Friction coefficient	-
f	Mixture fraction	-
$f(d)$	Probability density function for particle diameter	-
G	Mass flux	$kg/m^2.s$
g	Gravity constant	m/s^2
h	Pool liquid depth	m
H/h	Enthalpy	J/kg
k	Polytrophic constant	-
k	Turbulent kinetic energy	m^2/s^2
L	Monin-Obukhov length	m
L	Pipe/orifice length	m
L_e	Relaxation length in the homogeneous non-equilibrium model	m
L_{vap}	Latent heat of vaporization	J/kg
$\dot{m}$	Mass flow rate	kg/s
$\dot{m}_F$	Droplet vaporization mass flux	kg/s
B_0	Jet specific buoyancy flux	m^4/s^3
M_0	Jet specific momentum flux	m^4/s^2
Nu	Nusselt number	-
P	Pressure	Pa
Pr	Prandtl number	-
Q_g	Heat flux from the gas to the droplet	J/s
Q_L	Heat flux entering the droplet	J/s
r_d	Droplet radius	m
Re	Reynolds number	-
S/s	Entropy	J/K
Sc	Schmidt number	-
Sh	Sherwood number	-
T	Temperature	K
T_d	Droplet temperature	K

T_L	Fluid Lagrangian time-scale	s
U	Velocity	m/s
u_*	Friction velocity	m/s
U_s	Instantaneous fluid velocity seen by the particles	m/s
W_t	Wiener process	-
We	Weber number	-
x	Distance downstream of jet exit orifice	m
x	Gas mass fraction	-
x_0	Jet virtual origin	m
Y_i	Mass fraction of specie i	-
z_0	Roughness length	m

Subscripts

0	Initial
∞	Conditions at infinity
a	Air
atm	Ambient atmosphere
c	Critical/sonic conditions
c	Jet centreline value
F	Fuel/chemical vapour
f	Continuous phase
l	Liquid
lg	Difference between gas and liquid
ms	Metastable state
nbp	Normal boiling point
ori	Exit orifice
p	Particle phase
p	Pipe
r	Reference conditions for droplet vaporization
s	Droplet surface

sat	Saturation condition
sh	Superheat

Chapter 1

Introduction

1.1 Motivation and scope of work

Nowadays there is a great concern about accidental releases of toxic industrial chemicals into the atmosphere. Atmospheric dispersion of industrial chemicals constitutes a severe threat for people living in proximity of industries and storage areas where such materials are handled. The major part of industrial chemicals have the following properties:

- They cause health effects at relatively low concentrations.
- They are stored and transported as pressurized liquefied gases in large quantities.
- They quickly evaporate when released into the atmosphere.

Chlorine, ammonia and sulphur dioxide are often cited as the three most hazardous chemicals. Chlorine causes immediate chest pain, vomiting and cough at a concentration of 30 ppm, death at 1000 ppm for an exposure of a few minutes (EPA, 2007). A 10 min exposure to an ammonia concentration of 2700 ppm can have life threatening effects (NIOSH, 2008). These concentrations are low (maximum volume fraction of 0.27 %) compared to the lower flammability limits of very reactive gases such as hydrogen (4 % by volume) or methane (5 % by volume). It is more convenient to store and transport chemicals in the liquid state because of the large density ratio between a gas and a liquid. Since most of the toxic industrial chemicals have a normal boiling point well below common ambient atmospheric temperature (for example the normal boiling point of chlorine is -42.1 °C) they need to be pressurized in order to be transported or stored as liquids. Another effect of the low normal boiling point of toxic industrial chemicals is that they rapidly vaporize in the ambient atmosphere. They are said to be volatile. The combination of the above mentioned three features make these chemicals very hazardous. To sum-up: toxic industrial chemicals are transported in large quantities (second item), they are volatile (third item) and they cause death by inhalation at very low concentrations (first item).

Several accidental releases of industrial chemicals occurred in the last decade. On 28 June 2004, at approximately 5:03 AM at Macdona, Texas, USA, two trains collided and a 90-ton chlorine rail-car was breached (Hanna et al., 2008). It resulted in the release of 60 tons of chlorine and the subsequent death of three people and 43 injuries

Figure 1.1: *Photograph of the Graniteville accident (courtesy of the Environmental Protection Agency).*

from chlorine inhalation. A similar accident happened in Graniteville, South Carolina, USA, on January 6 2005, at 2:40 AM, about 60 tons of chlorine was released, nine people died and 250 people were treated for chlorine exposure (Hanna et al., 2008). Figure 1.1 shows a photograph of the scene. Chlorine was also involved in the Festus accident. The Festus accident began at 9:20 AM on August 14th, 2002, and the location was about 60 km north of St Louis (Hanna et al., 2009). The chlorine was being offloaded from a rail-car parked at a chemical facility. A 2.5 cm diameter hose ruptured at a height of 3.5 m near the rail-car. More than 20 tons of chlorine were released over a duration of three hours. Videos of the accident were recorded by the channel Fox News. The videos show a large visible gas cloud of depth about 1 m and width about 20 m to 30 m around the rail-car.

The accidents that were described here could have been more tragic. They happened early in the morning or even during the night and in low populated areas. One could imagine similar scenarios (trains collision or trains derailment) in highly populated areas such as a downtown city centres, in the middle of the day. The Department of Homeland Security (DHS) in the USA as well as other government agencies are considering these scenarios and fund research programs in order to get a better understanding of the physical processes involved in accidental toxic industrial chemicals releases (Britter et al., 2011). Hanna et al. (2009) present the results of simulations of hypothetical chlorine releases from rail-car tanks in downtown Chicago. The simulations were conducted with the FLACS model and will be discussed further later in the thesis. Recently, in 2010, field tests consisting of releases of pressurized liquefied ammonia and chlorine were completed in the USA and were funded by several regulatory agencies (such as DHS). The aim was to provide data sets for code development and validation. Moreover, toxic chemicals are not the only chemicals stored and transported as pressurized liquefied gases. Flammable chemicals with low normal boiling points are also stored and transported as pressurized liquefied gases. Propane or butane are examples of such flammable chemicals. The formation of a flammable gas cloud and its potential ignition represents the main hazard in this case.

Figure 1.2: *Photographs of the Festus accident taken from the Fox News video.*

The chemical, petrochemical and petroleum industries as well as regulatory agencies need high quality dispersion simulations for risk analysis purposes. Therefore, dispersion models must have an accurate prediction and description of the complex interactions between the gas cloud, atmospheric turbulence and possible obstacles surrounding the release. At present, the influence of obstacles and ground on industrial and flammable chemicals releases is neglected by most modellers. The dispersion models actually used for hazard assessments are mostly integral models (AERCLOUD, DEGADIS or PHAST for example). Even if they predict the complex physics of chemicals releases to some extent, they do not allow the user to perform realistic simulations since they describe unobstructed gas flows in flat terrain. The objective is to implement models in the 3-dimensional Computational Fluid Dynamics (CFD) model FLACS to simulate and study releases of pressurized liquefied gases in obstructed environments.

1.2 About the FLACS model

The FLACS model (Flame ACcelerator Simulator) is a 3D Computational Fluid Dynamics (CFD) model. It has been developed since the 1980s, successively by Christian Michelsen Institute (CMI), Christian Michelsen Research (CMR) and currently GexCon. The FLACS model is primarily aimed at simulating the dispersion of flammable and toxic gas in process areas and subsequent explosions of gas-air mixtures. The FLACS model solves the compressible conservation equations for mass, momentum, enthalpy and mass fraction of species on a 3D Cartesian grid using a finite volume method (FLACS, 2010).

It is important to note that the FLACS model is able to account for the effects of obstacles on the flow field. Obstructions can dramatically affect the results of both dispersion and explosion simulations. It has been shown experimentally and theoretically that explosions in congested areas were generating higher over-pressures than explosions in open, unobstructed, areas (Hjertager et al., 1984; Moen et al., 1980; van Wingerden, 1989). As the flame propagates through the gas cloud, the turbulence generated by the obstructions increases the flame speed, the higher the flame speed

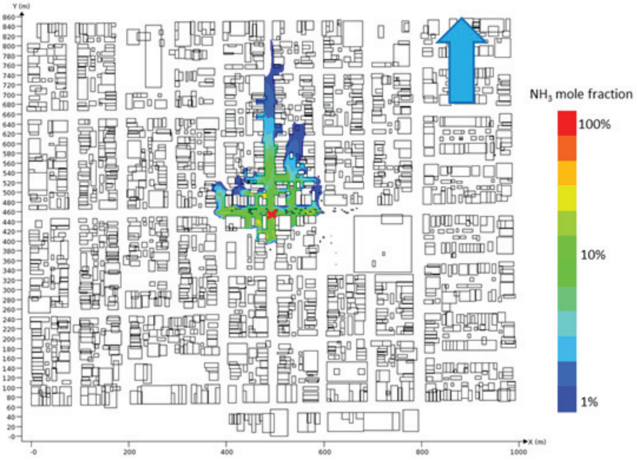

Figure 1.3: *Ammonia vapour concentration, 1.5 m above street level, in urban setting (Gavelli et al., 2011a).*

the larger the over-pressure that is generated. This concept was recently illustrated by investigating the Buncefield accident with the FLACS model (Bakke et al., 2010). On December 11th, 2005 there was a large explosion and fire at the Buncefield oil storage depot (Bakke and Brewerton, 2008). The investigation indicated that one of the large petrol tanks was overfilled and as a result a large flammable gas cloud was formed. A very dense vegetation composed of tree hedges was surrounding the whole depot. Simulations performed with the FLACS model have shown the importance of the dense vegetation. Computations without the incorporation of the vegetation into the geometry predicted maximum over-pressures of about 0.1 bar. These over-pressures could not explain the damage observed on the buildings located near the depot. Simulations with the vegetation included inside the geometry predicted over-pressures of about 10 bar, high enough to be consistent with the damages observed. When the flame enters the dense vegetation zone it accelerates due to the high degree of congestion.

The effect of obstructions on gas dispersion is multiple. Walls or fences can be used as mitigation techniques by confining the gas cloud. Flows over obstacles produce more turbulence and thus mixing between the pollutant and air is enhanced reducing the safety distances. However, the presence of obstacles does not always mitigate the hazard. In urban areas chemicals can be trapped inside the wake of buildings for several minutes, prolonging the duration of the hazard. Chemicals can also be transported "against the wind" due to the very complex pattern of flows inside network of street canyons as illustrated by Figure 1.3 (Gavelli et al., 2011a).

The FLACS model has been extensively validated against dispersion and explosion experiments. The work of Hjertager et al. (1988a,b) and Hansen et al. (2010b) report validation against explosion experiments. Hanna et al. (2004) present the results of the FLACS simulations of the Kit Fox, Prairie Grass, MUST and EMU dispersion experiments. The predictions were found to be in good agreement with the experimental observations. The dense gas dispersion experiments of the Model Evaluation Protocol (MEP) database (Ivings et al., 2007) were also simulated with the FLACS model (Hansen et al., 2010a). This database contains 33 experiments: Burro, Coyote, Falcon, Thorney Island and several more. The MEP aimed at providing a methodology for evaluating the capacity of models in accurately simulating the dispersion of gas clouds formed by accidental spills of Liquefied Natural Gas (LNG) on land. The MEP provided a set of Statistical Performance Measures (SPM) and criteria for a quantitative assessment of models. The FLACS model successfully met the criteria specified in the MEP (Hansen et al., 2010a).

1.3 Previous work and the current contribution

1.3.1 Previous work

Numerical studies of pressurized liquefied gas releases are rather rare in the literature. Polanco et al. (2010) and Bricard and Friedel (1998) gave comprehensive reviews of theoretical, experimental and numerical work on the subject. Consequences of accidental releases can either be predicted by integral models or by CFD models (this is a simplification, one could define many more classes of models in between "integral" and "CFD" which are at the two ends of the spectrum of models available and are the most widely used ones).

Integral models are based on the integration of the conservation equations for mass, momentum and energy across the cloud cross-section. They are today the current industry standard for dispersion simulations. Averaging considerably simplifies the problem but removes information about lateral variations of local variables such as the velocity or the temperature. Closure relationships need to be derived or inferred from experimental observations to somehow retrieve the information that was lost by averaging. The level of complexity varies from one integral model to another. Hanna et al. (1991) conducted an extensive validation of 14 integral models against 8 dispersion datasets. They measured the performances of each models by using a set of statistical performance measures and concluded on the most accurate models.

The models of Pattison et al. (1998a,b), Woodward et al. (1995) and Epstein et al. (1990) are some of the most detailed integral models dedicated specifically to releases of pressurized liquefied gases. The model presented by Pattison et al. (1998a,b) is composed of a set of one-dimensional conservation equations and is able to take into account condensation of water vapour, thermal non-equilibrium between the two phases and sloping terrain. The model was used to simulate the Desert Tortoise experiments (Goldwire et al., 1985) which consisted of releases of pressurized liquefied ammonia in open terrain, and the Goldfish trials in which pressurized liquefied hydrogen fluoride was discharged in open terrain (Blewitt et al., 1987). The authors report good agreement between experimental observations and numerical predictions. The model proposed by Epstein et al. (1990) is similar to the model of Pattison et al. (1998a,b) and the same experiments were used to validate the model. The predictions are said to be within a factor of three from the Desert Tortoise experimental observations and in good agreement with the Goldfish data. The model of Woodward et al. (1995), namely the Unified Dispersion Model (UDM) model can be seen as the most complete integral model for pressurized liquefied gases. The UDM model deals with all the physical processes involved in a release of pressurized liquefied gas. In Woodward et al. (1995) validation test cases are presented for each of the physical processes (rainout, pool evaporation, droplets vaporization, turbulent jets). A detailed description of these processes and their sequence is given in Chapter 2.

Integral models are able to predict the consequences of pressurized liquefied gases releases in open terrain. However, effects of obstructions cannot be properly estimated by integral models and CFD models have to be employed to deal with releases in obstructed terrains such as urban areas or chemical plants. Wurtz et al. (1996) have simulated a release of pressurized liquefied propane in obstructed terrain. The experiments that were considered are the EEC propane experiments (Heinrich and Scherwinski, 1990). In the experiment a 2 m high and 5.12 m long fence was located 48 m from the source, orthogonal to the wind direction. The numerical model is the ADREA-HF model, a 3D CFD model. Thermodynamic equilibrium is assumed and the two phases are treated as a mixture. Wurtz et al. (1996) compared the predicted concentrations with experimental observations in the far field of the release. The predictions are in good agreement with the experimental data. Aamir and Watkins (2000) conducted a numerical analysis of depressurisation of highly pressurised liquid propane. An Euler-Lagrange method was employed to model the two-phase flow. The numerical results in the near field of the jet were compared with the experimental data of Hervieu and Veneau (1996) and Allen (1998a,b). The predictions were found to be in satisfying agreement with the experimental data. Calay and Holdo (2008) have used the commercial CFD model Star-CD to simulate releases of pressurized liquefied gases. The Euler-Lagrange approach was employed to model the two-phase flow. Unobstructed releases of propane and R134-A were considered. The study was restrained to the near field of the release where the flow is two-phase and the dispersion of the chemical is controlled by the momentum of the jet. The results show a number of shortcomings. The authors highlight the importance of an accurate prediction of the source term. The quality of the source term is preponderant to obtain results in good agreement with experimental observations. To conclude, very few CFD investigations of pressurized liquefied gas releases are available in the literature. The focus is either on the near-field or on the far-field, none of the CFD studies details all the physical processes occurring during the release or consider important scenarios such as impingement on obstacles located in the near field of the release.

1.3.2 Current contribution

The current contribution to the field of hazardous gas dispersion is the development of a CFD methodology for studies of pressurized liquefied gases releases into the atmosphere. The development of the CFD methodology includes:

- Investigation of the capacities of existing source term models in predicting recent experimental observations: mass flow rate and distribution of droplet size.

- Implementation of two-phase flow models in the FLACS model to simulate droplets laden flows. An Euler-Euler approach based on the assumption of homogeneous equilibrium flow (HEM) and an Euler-Lagrange approach are considered.

- Investigation of the dispersion of heavy particles in isotropic turbulent flows by means of the Kinematic Simulation approach (Ichard and Melheim, 2010). The experiments of Snyder and Lumley (1971) were simulated and very good agreement was seen between experimental data and numerical predictions.
- Proposition of a rain-out model in connection with the HEM approach.
- Validation of the newly implemented two-phase flow models with laboratory scale experiments. Three experiments are simulated: two experiments on solid particles laden turbulent jet flows and one spray experiment.
- Improvements of the current FLACS models for liquid spreading and evaporation on the ground. An algorithm has been developed and implemented in order to solve the equations of the pool model on a user-defined uniform grid having a finer resolution compared to the grid used to solve the surrounding flow field.
- The methodology developed in the thesis is used to simulated large scale releases of pressurized liquefied gases. Four experiments are considered and the results of the numerical computations compare well with experimental observations.

In addition to the work on pressurized liquefied gases, efforts have been dedicated to the validation of the FLACS dispersion model and include:

- Simulations of the Burro, Coyote, Maplin Sands, Falcon and Thorney Island tests series (Hansen et al., 2010a). These experiments are part of the model validation database of the model evaluation protocol for Liquefied Natural Gas (LNG) vapour dispersion (Ivings et al., 2007). As a result of this validation exercise the FLACS model is currently the only approved model for the simulation of all LNG vapour dispersion scenarios required for the siting of an onshore LNG facility in the United States (GexCon, 2011).
- Simulations of the LH_2 NASA spill (Middha et al., 2011) and the LH_2 releases performed at the Health and Safety Laboratory (HSL) (Ichard et al., 2011).
- Simulation of the Festus accident which involved a release of chlorine at an industrial site (Hanna et al., 2009).

1.4 Organisation of the thesis

Chapter 2 explains the sequence of physical processes which occur when a pressurized liquefied gas is released into the ambient atmosphere. Flashing is one of the processes discussed in details. The explanation is based on both theory and recent experimental observations. The experiments presented in Chapter 2 are used as test cases in later chapters.

Chapter 3 investigates the performance of different models in predicting the source term and pseudo-source term when simulating releases of pressurized liquefied gases. The chapter concludes with the recommendation of models.

Chapter 4 presents simulations of single-phase, variable density, turbulent jets performed with the FLACS model. The chapter aims at introducing the FLACS model in more details and at assessing its performance in simulating the "simple case" of single phase turbulent jet before moving on to more complex, two-phase flows.

In Chapter 5 we discuss the Euler-Lagrange model that is implemented in the FLACS model. Laboratory-scale validation test cases are simulated and the results presented. The experiments of Hardalupas et al. (1989); McDonell and Samuelsen (1995); Sheen et al. (1994) are considered.

Chapter 6 deals with the implementation of the Euler-Euler model based on the homogeneous equilibrium flow assumption, the HEM approach. As for the Euler-Lagrange model, laboratory-scale experiments are simulated. A model for liquid deposition on the ground or on obstacles is proposed. Improvements to the current FLACS model for liquid spreading and evaporation are presented.

In Chapter 7 the methodology that has been developed is used to simulate large-scale experiments. Four large-scale experiments in open and obstructed terrain are considered: the CCPS, FLIE-INERIS, Desert Tortoise and Falcon experiments.

Appendix A contains the paper Ichard and Melheim (2010). Investigation of the dispersion of heavy particles in isotropic turbulent flows by means of the Kinematic Simulation approach is presented. It illustrates important concepts of the dispersion of heavy particles in a turbulent flow field such as the inertia effect and the crossing-trajectory effect.

Appendix B contains the paper Middha et al. (2011). The contribution to this paper is the simulation of the NASA LH_2 spill experiment. The current FLACS models for liquid spreading and evaporation on the ground are validated with LH_2 and the importance of atmospheric stability conditions and their effects on the dispersion of the H_2 gas cloud are emphasized.

Chapter 2

An introduction to flashing liquids releases

2.1 The physics of flashing releases

2.1.1 Theory of flashing liquids

In the previous chapter it was explained that many toxic and flammable chemicals are stored and transported as pressurized liquids. The pressure inside the reservoir is larger than the ambient atmospheric pressure. If accidentally released into the atmosphere (through a breach in the tank envelope for example) the liquid suffers a rapid depressurisation and as a consequence boils violently. This is the flashing process. Figure 2.1 illustrates the saturation line for a hypothetical volatile substance in a pressure-temperature (P,T) diagram. The point (P_0,T_0) represents the storage conditions. The terms subcooling and superheat appearing on the (P,T) diagram are used to characterise flashing releases. For a given mass of liquid at conditions (P_0,T_0), the liquid is said to be sub-cooled if the temperature T_0 is less than the boiling point temperature at the pressure P_0, and superheated if the temperature T_0 is greater than the boiling point temperature at the pressure P_0. In most flashing releases the liquid inside the reservoir is sub-cooled or saturated with reference to the storage conditions (T_0,P_0), i.e. $T_0 \leq T_{sat}(P_0)$, and superheated with reference to atmospheric conditions (T_{atm},P_{atm}), i.e. $T_0 > T_{sat}(P_{atm})$. During the release of a pressurized liquid through a pipe or a sharp-edged orifice, the sudden depressurization causes the liquid to reach a meta-stable state, noted (T_{ms},P_{ms}) in Figure 2.1. The liquid is unable to boil at a sufficiently high rate to maintain its pressure-temperature equilibrium, and the material stays in liquid phase at temperatures significantly above the boiling point. The liquid temperature is governed by processes associated to mass transport, which are slower than the depressurization process.

The flashing process can also be represented on a (P,v) diagram as it is often the case in the literature (Polanco et al., 2010; Sher et al., 2008). In their review of flash atomization Sher et al. (2008) give a detailed description of the physics involved in the flash process. Flashing of an initially subcooled liquid can either be obtained by isobaric heating or by an isothermal pressure drop (lines OA and OB in Figure 2.1). In our work flashing occurs mostly via an isothermal pressure drop since pressurized liquids are often stored at ambient temperature. On a (P,v) diagram the metastable region is bounded by the spinodal curve. The spinodal curve determines the thermodynamic extent to which the liquid can be brought without vaporization (Sher

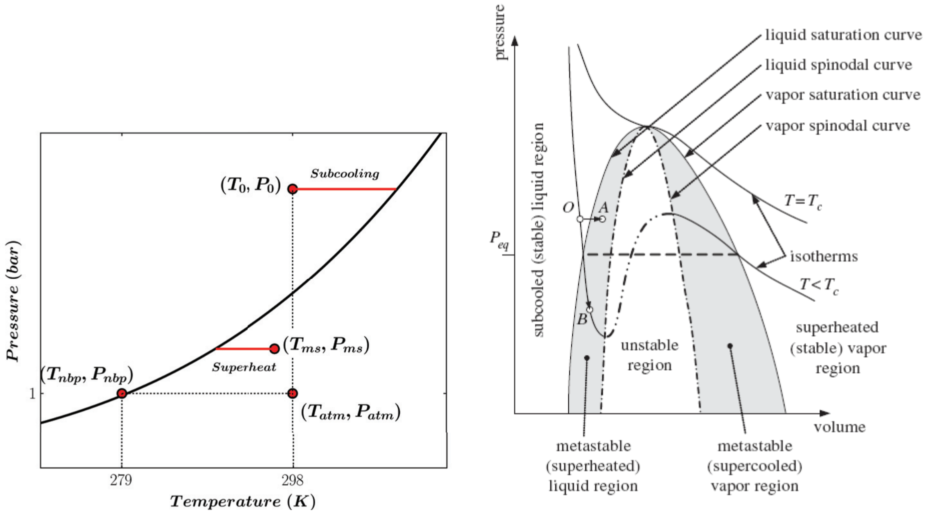

Figure 2.1: ***Left plot***, *Pressure-Temperature (P,T) diagram with a saturation line for a hypothetical chemical substance.* ***Right plot***, *pressure volume diagram for a hypothetical chemical substance (taken from Sher et al. (2008)).*

et al., 2008). Local thermodynamic fluctuations in the metastable liquid result in nuclei generation of the stable phase. Two types of nucleation can take place. Homogeneous nucleation occurs in the volume of the superheated liquid and heterogeneous nucleation initiates from wall boundaries or dissolved impurities. Nucleation theory gives the number of bubbles generated per unit time and per unit volume. From bubble nucleation the process goes on with bubble growth and shattering of the liquid phase. The term flash atomization is employed to describe the disintegration of the liquid flow. The process ends with a two-phase mixture in thermodynamic equilibrium. The review of Sher et al. (2008) and references therein provide more details on specific aspects such as bubble nucleation, bubble growth and flashing incept.

2.1.2 Description of a flashing release

Complete flashing results in a high momentum two-phase jet with droplets and vapour in thermodynamic equilibrium as illustrated on Figure 2.2. The spray is said to be polydispersed and the largest droplets may deposit on the ground. Therefore, accidental releases of pressurized liquids may yield to the formation of liquid pools on the ground. This is the rain-out process. The rain-out process can largely be enhanced if the two-phase jet impinges on an obstacle. The effect of rain-out on downstream gas concentrations is two-fold. On one hand it has a positive effect because the mass of chemical inside the jet is reduced and thus are the downstream gas concentrations. On the other hand it may have a negative effect because the duration of the hazard might be increased: the liquid pool may continue to evaporate long after the release has stopped. The momentum of the jet progressively dies out and further dilution of the chemical is controlled by atmospheric turbulence. Due to their molecular weight greater than air,

Figure 2.2: *Photograph of an impinging propane release taken during one of the FLIE-INERIS tests (taken from Bonnet et al. (2005)).*

many toxic and flammable chemicals behave as dense clouds. The dense cloud effect is enhanced by the presence of liquid droplets inside the cloud. Here is a list of all the different models needed in order to simulate the release of a pressurized liquefied gas with a CFD code:

- source term: compute the mass flow rate and gas mass fraction at the exit orifice (Chapter 3).
- pseudo-source term: compute the parameters of the jet when complete flashing and expansion have occurred (Chapter 3).
- two-phase jet: simulate droplet-laden turbulent jets with a CFD code (Chapter 5 and 6).
- rain-out: simulate the deposition or impact of droplets on obstacles (Chapter 5, 6 and 7).
- pool: simulate the spread and vaporization of the pool formed by rain-out (Chapter 6 and 7)
- atmospheric dispersion: simulate gas dispersion in the atmosphere (Chapter 7)

Several reviews of flashing jet studies are available in the literature: Bricard and Friedel (1998); Sher et al. (2008); Witlox and Bowen (2002). In this thesis the scenario of interest is the flashing jet scenario. Accidental releases of pressurized liquefied gas can also yield to a boiling liquid expanding vapour explosion (BLEVE). Such a scenario occurs when a vessel is ruptured. Due to the large breach the pressure drops suddenly inside the vessel causing the liquid to boil violently and liberating large amount of vapour. This scenario is not investigated in this thesis but could be included in future work. Abbasi and Abbasi (2007) provide a review of the BLEVE phenomenon.

2.2 Experimental observations

Recent experiments on releases of pressurized liquids are reviewed in this section. The review provides an illustration of the concepts we have introduced in the previous section. The experiments discussed below will also be used as validation test cases later in the thesis.

2.2.1 The Von-Karman Institute tests

The experiments performed at the Von-Karman Institute in 2004 as part of the EU funded research project FLIE (Flashing Liquids in Industrial Environment) were aimed at studying the influence of initial storage conditions on two-phase jet characteristics in case of a sudden release of a pressurized liquefied gas (Yildiz et al., 2004). Pressurized liquefied R134-A was released horizontally in eight different tests. Optical based techniques (Particle Image Velocimetry and Phase Doppler Anemometry) were used to measure droplet diameter and velocity distributions and pictures of the flashing jet from high-speed videos gave the possibility to investigate the break-up pattern of the flashing jets.

Yildiz et al. (2004) tried to investigate the break-up length of flashing jets by studying pictures extracted from high-speed videos. The break-up length of flashing jets corresponds to the location where the jet is fully expanded and atomized. It appeared that the break-up of a flashing jet was a random process and that consequently the break-up length was a random variable. The probability density function of this random variable should be determined by treating a large number of pictures of flashing jet break-up. (Yildiz et al., 2004) reported that the number of pictures was not enough to conduct a proper statistical study and thus only sparse data for the break-up length were obtained. Lienhard and Day (1970) were able to perform such a study for water and nitrogen. The data obtained by Lienhard and Day (1970) seem to show that the break-up length is around 20-30 orifice diameters and that for the same degree of superheat an increase in the nozzle diameter greatly reduces the break-up length.

Yildiz et al. (2004) studied the effect of the degree of super-heat on the velocity and diameter of the droplets. On one hand, they observed bigger droplets on the centreline axis of the jet having the lowest degree of superheat and, on the other hand, they observed a wider jet envelope with bigger droplets on the edges of the jet having the largest degree of superheat. This means that the intensity of the atomization process increases with the degree of superheat producing smaller droplet on the jet axis and pushing some of the big droplets on the edges of the jet. It is also interesting to note that the axial velocity of the droplets on the jet axis did not change as the degree of superheat increased. Therefore, an atomization process that is due to bubble generation inside the liquid fragments (explosive boiling) rather than due to aerodynamic break-up, explains the differences in droplets size on the centreline axis. The effect of the storage pressure was also investigated. The increase in storage pressure implied an increase in droplet velocity and a decrease in droplet size due to a more efficient aerodynamic break-up process. The effect of storage pressure was noted on the droplet velocity distribution counts; the distribution was shifted to higher velocity values without any changes in the pattern.

The experimental work conducted at the Von-Karman Institute gave some useful indications on how the droplet size and velocity are affected by the release conditions and underlined the difficulty in estimating the break-up length for flashing releases. However, the tests involved releases of one chemical substance only and were performed at laboratory scale. It would therefore be of interest to discuss a set of experiments performed at a larger scale, closer to the industrial scale and involving different substances.

2.2.2 The FLIE-INERIS tests

The FLIE-INERIS test series consisted of 94 large-scale flashing jet releases carried out from March to October 2004 by INERIS in France (Bonnet et al., 2005). Two different liquefied gases were used, 64 tests were performed with propane and 30 tests with butane. The aim of the experiments was to investigate the properties of flashing jets at a relatively large-scale closer to the industrial scales. The influence of several parameters on the behaviour of a flashing jet was investigated. In addition to the vapour pressure of the liquefied gas; 0, 1, 3 or 6 bar over-pressure in the storage tank was added using nitrogen. Circular orifices of diameters ranging from 2 mm to 25 mm as well as rectangular and square orifices were used. The tests were conducted outdoor.

The diameter, axial velocity and vertical velocity of droplets were measured using Phase Doppler Anemometer (PDA), a non-intrusive optical measurement technique. A double PDA system was built in order to simultaneously measure two components of the droplet velocity vector (axial and vertical) and the droplet diameter. PDA measurements conducted outdoor are a lot more challenging than PDA measurements in controlled and confined environments such as laboratories. For example, abrupt changes of wind direction and speed during the tests lead to a deviation of the jet from the measurement volume created by the laser beams of the PDA system. Another example is the effect of high relative humidity of the ambient atmosphere, causing failures of the measurement technique due to the high opacity of the cold, two-phase jet. Due to these difficulties, from the 313 measurement locations tested only 178 locations gave exploitable results, a success rate of 57 %. As regards to the number of droplets detected at each measurement position, a number of 5000 drops and a maximum waiting time of 10 s have been set. Investigation of the effect of the number of drops on the quality of the statistics was performed for a test where 20000 droplets were detected. The difference in the arithmetic mean droplet diameter computed with 20000 droplets and 1000 consecutive droplets is on average 3.6 % (maximum of 5 %). This average difference goes down to 0.8 % (maximum of 2.3 %) if 3000 droplets are used for the statistic computations.

Retention tanks were placed on weight indicators below the jet and then the rain out was measured for free and impinging jets. Impingement distances of 0.83, 1.60 and 2.57 m between the exit orifice and the wall were tested. For free flashing jets of propane INERIS reported that no pool formation took place. For butane, a maximum value of 10 % for the rain-out percentage has been observed in some tests. As we would expect the presence of obstacles in the near field of flashing jets increases the amount of liquid that deposits on the ground. For an obstacle at 0.83 m of the exit orifice, 45 % of the mass released was observed to rain-out for a butane test. Only 15 % of the mass released was observed to rain-out for a propane test with an obstacle at the same distance of the exit orifice, i.e. 0.83 m. Temperature data along the jet axis and jet edges are also available. Thermo-couples were used to obtain the temperature data along the centreline axis of the jets.

2.2.3 The CCPS tests

The US Center for Chemical Process Safety (CCPS) began a research program in 1988 to investigate the behaviour of droplets which are formed when a pressurized liquefied gas is accidentally released into the atmosphere (Johnson and Woodward, 1999). The main point was to understand how much of a release is likely to rain-out on the ground near the release point. The CCPS experiments were carried out in two phases. The first one, the Oklahoma experimental program, occurred in the summer of 1989 and consisted of 49 releases of super-heated water and 15 releases of super-heated CFC-11. The second test series, the Nevada experimental program, was conducted in the summer of 1990 and involved 22 releases of chlorine, 18 releases of methylamine and 20 releases of cyclohexane. The development of a numerical model for superheated liquid releases, the RELEASE model, was also part of the research program (Johnson and Woodward, 1999). In all tests, the storage reservoir was padded with nitrogen and the pipe connecting the bottom of the reservoir to the exit orifice was kept as short as possible in order to minimize flashing prior to the release in the ambient atmosphere.

The rain-out data were presented as a single value for each test, i.e. no information available on rain-out distribution as a function of the distance from the orifice. All of the tests involved horizontal releases 1.22 m above the liquid collection system and a range of exit orifice diameters was tested (6.4, 12.7 and 3.2 mm). The influence of releases direction and elevation on the amount of rain-out was not investigated. The releases were operated inside a greenhouse tunnel in order to protect them from strong winds. Figure 2.3 shows the observed rain-out for water and CFC-11. There is a noticeable difference between the dependence of rain-out on the degree of superheat for water and for CFC-11. The water releases (non-volatile liquid, i.e. the normal boiling point is above the ambient temperature) show a linear decrease in the amount of rain-out as the degree of super-heat increases whereas for the CFC-11 releases (volatile liquid, i.e. the normal boiling point is below the atmospheric temperature) a critical degree of superheat seems to exist. The size of the exit orifice appears to have no influence on the amount of rain-out. The authors reported that the greenhouse tunnel might have been saturated with water vapour at some point and then that the evaporation rate of the droplets in flight would have been decreased enhancing the amount of rain-out. However, as we would see in Chapter 7, the CCPS data for water do compare quite well with other recent experiments performed at the laboratory scale (Bigot et al., 2005).

The phase two tests were carried out outdoor in the Nevada desert. As for phase one, the tests involved horizontal releases 1.22 m above the liquid collection system and the same range of exit orifice diameter was tested. In order to prevent premature evaporation of the rain-out liquid, the capture pans were cooled by spraying water from below for the cyclohexane tests and a chemical reaction inside the pans was used for the chlorine and methylamine tests. However, Johnson and Woodward (1999) mention that those precautions might not have been enough to protect the captured liquid from evaporation. They propose a set of corrected data, said to be free of premature evaporation. The corrections are based on droplet evaporation and pool evaporation

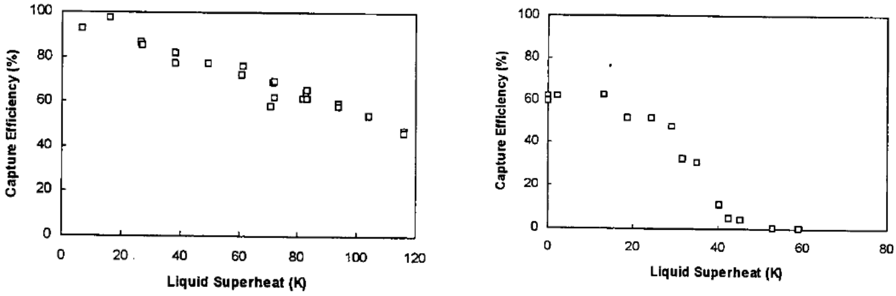

Figure 2.3: *Rain-out as a function of the degree of super-heat for water [left plot] and CFC-11 [right plot]. The plots are taken from Ramsdale and Tickle (2000).*

modelling with the UDM code (Woodward and Papadourakis, 1995). The dependence of liquid rain-out on the degree of superheat for all three chemicals is found to be similar to that of the CFC-11. Finally, it can be mentioned that a comprehensive review of these experiments was performed by Ramsdale and Tickle (2000).

2.2.4 The Desert Tortoise tests

The Desert Tortoise series was conducted by the Lawrence Livermore National Laboratory (LLNL) at the Frenchman Flat area of the Nevada Test Site (USA) during the summer of 1983 (Goldwire et al., 1985). The series was designed to document atmospheric transport and diffusion of ammonia vapour resulting from a cryogenic release of liquid ammonia. Four releases of pressurized liquefied ammonia were performed. Ammonia was released from a spill pipe pointing downwind at a height of 0.8 m above the ground. The liquid ammonia flashed as it was exiting the pipe producing a two-phase jet with a high momentum. Mass flow rates ranged from 80 kg/s to 130 kg/s. Rain-out was observed for some of the tests. All tests but one were performed under neutral atmospheric conditions. Gas concentrations and cloud temperature were measured at two rows of sensors, 100 m and 800 m downwind. Figure 2.4 shows a photograph of one of the test. Pools of water on the ground are clearly visible on the photograph and were due to some heavy rains that had occurred before the experimental series. Therefore, the tests were conducted with a significant variation in humidity and unusual surface conditions.

2.3 The current FLACS approach

From the previous sections we know that the release of a pressurized liquid results in the formation of a high momentum two-phase jet. The droplets gradually vaporize as air is entrained into the jet and at some distance from the exit denoted L_{gas}, the jet becomes a pure vapour jet. In the current commercial version of the FLACS model the 3D computations start at the location L_{gas} by specifying the parameters of a gas leak (FLACS, 2010). A one-dimensional utility program called *flash* is used to compute the

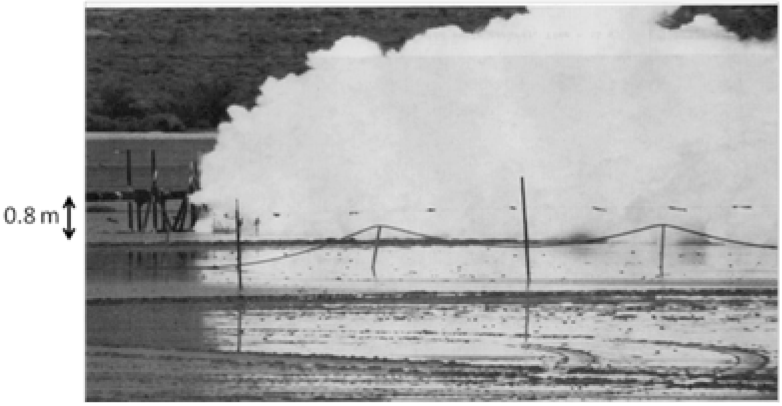

Figure 2.4: *Photograph of the Trial 2 of the Desert Tortoise field experiment, 35 s after start of release. Photograph taken from Goldwire et al. (1985).*

parameters of this gas leak as well as the amount of rain-out. The utility program *flash* is described in details in Salvesen (1995).

The utility program *flash* was applied to an hypothetical release of chlorine from a rail car tank in downtown Chicago (Hanna et al., 2009) and illustrates the weaknesses of the current approach in the FLACS model. The release was forming a 45 ° angle with the centreline axis. Chlorine was pressurized inside the rail car tank and the tank pressure was about 7 bar. The utility program *flash* was applied to simulate the jet out to a point where the pressure reduced to ambient and the aerosol evaporated. The aerosols were estimated to evaporate by a distance of 24 m. At this distance, a chlorine vapour source jet was defined for input to the FLACS model with cross section area of 26 m^2, velocity of 14 m/s, temperature of -70 °C.

The calculations of the utility program *flash* assume that there is no impingement on objects during the evaporation and expansion process. However, in this scenario the release direction is at 45° downward. The jet would therefore impinge on the ground after only a few meters, and the pseudo-source shape would be flattened. The user has to define the shape of the source in order to artificially reproduce the effect of jet impingement. One other effect of the jet impingement would be to increase the amount of rain-out. But again this cannot be accounted for in the utility program *flash*. More errors would be introduced if in between the orifice and the distance L_{gas} (24 m in this case) a large wall were standing. The current approach would fail for such a scenario which is quite common in congested areas. One solution would be to start the CFD computations at the location where flashing and atomization of the jet is complete. This is the objective of the thesis.

Chapter 3

Models for the source term of flashing jets

3.1 Mass flow rate and jet expansion

3.1.1 Overview

The first step in any CFD simulations of accidental releases of pressurized liquefied gases is the computation of the source term; i.e. the computation of both the mass flow rate and the vapour mass fraction at the exit orifice. It can also be necessary to compute a pseudo-source term at some distance from the exit orifice where the flow has reached thermodynamic and mechanical equilibrium. In the reservoir the material is in the liquid state and is either subcooled or saturated. Many types of scenarios can occur. The chemical substance can be released through a hole in the wall of a tank. The term sharp-edge orifice is then employed. Another scenario could consist in the release of a substance through a long pipe connecting the bottom of a storage tank to an exit orifice. Upon release, due to the depressurization, the flow can progressively change state and be two-phase at the exit orifice.

There exist different classes of models for single phase and two-phase releases. They range from full 3D computations of the flow field from the reservoir to the orifice to simplified analytical-based approach. The 3D models can solve with limited assumptions the most complex release scenarios (consider for example the release with a change of phase through a network of pipes with elbows, sudden restrictions or expansions) but they require far more computational resources than the analytical models. These 3D, complex, models can accurately describe interfacial phenomena that occur between a liquid and a vapour flowing in a pipe. They are mainly used in the nuclear industry (computer codes: RELAP5, RAMONA-4B, see Fthenakis, Rohatgi, and Chung (2003)) to simulate accidental loss of coolants. Research on phase transition in metastable liquids and its application to flashing releases provide a deeper understanding of the physical phenomena involved (Saurel et al., 2008). The "metastable-approach" presented by Moreira and co-workers (Simoes-Moreira and Bullard, 2003; Simoes-Moreira et al., 2002) is discussed further in this work along with two analytical models: the energy balance model (Woodward, 2009) and the homogeneous non-equilibrium model (Fauske and Epstein, 1988). Analytical models have been extensively used in the past to compute the source term of accidental releases. We refer to the review of MRS (1992) and Elias and Lellouche (1994) for more details on the numerous existing analytical models.

3.1.2 The Bernoulli approach

The Bernoulli approach assumes a pure liquid flow at the exit orifice. The flow is incompressible and the mass flow rate is given by a Bernoulli type equation:

$$\dot{m} = A_{ori} C_D \sqrt{2\rho_{l,0}\left(P_0 - P_{atm}\right)} \tag{3.1}$$

where A_{ori} is the area of the exit orifice and C_D is the discharge coefficient which accounts for the vena contracta effect at the exit (Batchelor, 1967). For liquid and two-phase flows through orifices the discharge coefficient is set to 0.62 whereas for pure gas flow a value of 0.8 is used (Britter et al., 2011). Note that the pressure at the exit orifice is the atmospheric pressure, i.e. the ambient pressure. The predictions obtained with Equation (3.1) are conservative and agree well with experimental data for releases through sharp-edge orifices and for releases through pipes with $D_{ori}/D_p \ll 1$, where D_{ori} is the diameter of the exit orifice and D_p is the pipe diameter (Richardson et al., 2006; van Den Akker et al., 1983). For cases where the diameter of the exit orifice is not much smaller than the pipe diameter the flow might be two-phase at the exit and the mass flow rate is largely over-estimated by Equation (3.1). Models that can account for friction and phase change through pipes and orifices are presented in the sections below.

3.1.3 The energy balance model

The energy balance model is described by Woodward (2009). The general case where a pipe of diameter D_p and length L connects a storage tank to an exit orifice of diameter D_{ori} is considered. Release through a sharp-edge orifice occurs when the length of the pipe is zero. The idea beyond the energy balance model is to assume that the available pressure drop is divided between the pipe and the orifice. The pressure drop across the pipe is noted $\triangle P_p = P_0 - P_1$ and the mass flux through the pipe is noted G_p. The pressure drop through the orifice is $\triangle P_{ori} = P_1 - P_{ori}$ and the mass flux is G_{ori}. One has to find the pressures P_1 and P_{ori} such that $G_p = G_{ori}$. An iterative method is employed. As a starting point the mass flow rate G_p is guessed. The pressure P_1 is found by integrating the momentum balance equation through the horizontal pipe of length L:

$$v_l dP + G_p^2 v_l dv_l + \left(4 f_l \frac{dx}{D_p} + K\right) \frac{1}{2} G_p^2 v_l^2 = 0 \tag{3.2}$$

The fanning friction factor f_l is obtained from the Colebrook-White correlation (van den Bosch and Weterings, 1997), K is a correction coefficient for pipe bends, valves or sudden pipe contractions and v_l is the specific volume of the liquid. The substance is assumed to stay in the liquid state inside the pipe. The liquid temperature is controlled by processes which are associated to mass transport. These processes act on a time-scale which is larger than the depressurization time-scale and thus, inside the pipe, the pressure decreases but the temperature remains constant. The change of state, if any, occurs through the orifice. The flashing begins at the saturation pressure corresponding to the stagnation temperature as assumed by Leung and Grolmes (1988). The pressure P_1 obtained from Equation (3.2) is used to find G_{ori} and P_{ori} by solving the energy balance equation. Following Woodward (2009), across the orifice the energy balance equation reduces to:

$$U_{ori} = \sqrt{2\left(H_1 - H_{ori}\right)} \tag{3.3}$$

The assumption is made that the flow follows an isentropic expansion path through the orifice. The pressure is gradually decreased from P_1 down to P_{ori}. At each intermediate state (P_n, T_n) with $T_n = T_{sat}(P_n)$ the flash fraction is estimated from:

$$x_n = \frac{S_{l,1} - S_{l,n}}{S_{g,n} - S_{l,n}} \tag{3.4}$$

where $S_{*,*}$ is the specific entropy of the substance. Assuming homogeneous flow the specific enthalpy is estimated from:

$$H_n = xH_{g,n} + (1-x)H_{l,n} \tag{3.5}$$

The mass flux across the orifice is given by:

$$G_{ori} = \frac{U_n}{v_n} \tag{3.6}$$

The pressure is decreased until either G_{ori} is maximised or the ambient pressure is reached, i.e. $P_{ori} = P_{atm}$. If $G_{ori} = G_p$ the iterative process stops and the source term has been computed. If $G_{ori} \neq G_p$ then G_p is decreased and the procedure that has just been described is repeated.

3.1.4 The homogeneous non-equilibrium model

A method that does not require any numerical integration or iterative process to compute the mass flow rate is now discussed. The homogeneous non-equilibrium method originates from the $\omega - method$ of Leung (1986). The $\omega - method$ uses a general equation of state for two-phase expansion:

$$\frac{v}{v_{l,0}} = \omega\left(\frac{P_0}{P} - 1\right) + 1 \tag{3.7}$$

and the ω parameter, for saturated or subcooled liquid, is expressed as:

$$\omega = \frac{C_{p_{l,0}} T_0 P_{sat}(T_0)}{v_{l,0}} \left(\frac{v_{lg,0}}{H_{lg,0}}\right)^2 \tag{3.8}$$

The ω parameter reflects the compressibility of the substance due to phase change or flashing upon depressurization. The critical mass flux writes :

$$G_{\omega,\eta_c} = \eta_c \sqrt{\frac{P_0}{v_{l,0}\omega}} \tag{3.9}$$

where η_c is the critical pressure ratio (Moncalvo and Friedel, 2010):

$$\eta_c = \begin{cases} \sqrt{2\omega}\left(1+\sqrt{2\omega}\right)^{-1} & \text{if } 0 \leq \omega \leq 1 \\ \left[(\omega+3)\sqrt{2\omega}+4\omega\right]\left[\left(2+\sqrt{2\omega}\right)\left(\omega+\sqrt{2\omega}+\sqrt{3+2\sqrt{2\omega}}\right)\right]^{-1} & \text{if } \omega > 1 \end{cases} \tag{3.10}$$

Fauske and Epstein (1988) combine the expression G_{ω,η_c} with a Bernoulli-like equation to estimate the mass flux of saturated and subcooled liquids through sharp-edge orifices or short pipes:

$$G_{HNE} = \left(G_l^2 + N_{ne} G_{\omega,\eta_{ne}}^2\right)^{0.5} \tag{3.11}$$

The mass flux G_l is given by a Bernoulli-like equation with the exit pressure set to the saturation pressure at the storage temperature. The first term under the radical in Equation (3.11) accounts for subcooled initial conditions and goes to zero as saturation conditions are approached. The second term contains all the compressibility effects due to potential flashing. Initially, in Equation (3.11), Fauske and Epstein (1988) assumed $G_{\omega,1}$. Our formulation is slightly different, the non-equilibrium critical pressure ratio is expressed as:

$$\eta_{ne} = \begin{cases} 0, & \text{if } \eta_c > \eta_s. \\ \eta_c, & \text{if } \eta_c \leq \eta_s. \end{cases} \tag{3.12}$$

where $\eta_s = P_{sat}(T_0)/P_0$. The parameter N_{ne} has been added to reflect the non-equilibrium effects. It has been experimentally observed that for pipe lengths shorter than $L_e = 0.1$ m, the residence time of the liquid inside the pipe is too short to permit the onset of bubble nucleation and the liquid undergoes a delay in flashing (Darby et al., 2001). Following Fauske (1985) for $L < L_e$ we have:

$$\frac{1}{N_{ne}} = \frac{v_{l,0} H_{lg,0}^2}{2\left(P_0 - P_{sat}(T_0)\right) v_{lg,0}^2 T_0 C_{p_{l,0}}} + \frac{L}{L_e} \tag{3.13}$$

This method cannot properly model the pressure losses due to pipe friction which are non-negligible when the pipe length is greater than the relaxation length L_e. Therefore, the homogeneous non-equilibrium method is only applied to scenario with a short pipe (i.e. $L < L_e$). If the predicted pressure at the exit orifice is larger than the atmospheric pressure, Equations 3.14, 3.15 and 3.16 are used to compute the jet expansion.

3.1.5 The control volume model for the expansion region

From the exit orifice it is necessary to compute the "flash expansion" of the jet. The expansion process is modelled as a one-dimensional homogeneous flow without air entrainment. A control volume can be drawn around the expansion region and the application of the conservation of mass, momentum and energy to this control volume yields (Britter, 1995; Witlox and Bowen, 2002):

$$\dot{m}_{ori} = \dot{m}_{atm} \tag{3.14}$$

$$\dot{m}_{atm} U_{atm} = \dot{m}_{ori} U_{ori} + (P_{ori} - P_{atm}) A_{ori} \tag{3.15}$$

$$\dot{m}_{atm}\left(H_{atm} + \frac{1}{2}U_{atm}^2\right) = \dot{m}_{ori}\left(H_{ori} + \frac{1}{2}U_{ori}^2\right) \tag{3.16}$$

The change of kinetic energy is often negligible compared to the phase change enthalpy and thus we assume that an isenthalpic flash calculation is acceptable. The control volume model is used in connection with the energy balance and homogeneous non-equilibrium models.

3.1.6 The model of Moreira *et al.*

Moreira and co-workers have extensively studied the physics of highly expanded flashing jets (Simoes-Moreira, 2000; Simoes-Moreira and Bullard, 2003; Simoes-Moreira and Shepherd, 1999; Simoes-Moreira et al., 2002). Their experiments on flashing jets have allowed identifying 3 main physical phenomenon:

- Metastable liquid flows
- Regimes of liquid evaporation
- Supersonic flows and shock waves

The metastable property of liquid flashing flows has been discussed briefly previously. Metastability is associated with the departure from thermodynamic equilibrium just prior to flashing and it creates a so-called under-pressure of vaporization (Simoes-Moreira and Bullard, 2003). Depending on the degree of metastability, 3 different regime of liquid evaporation or flashing have been observed (Simoes-Moreira and Bullard, 2003). Moreira and co-worker focus on regime 3 of liquid evaporation which corresponds to the highest degree of metastability. A high degree of metastability is often related to a large $P_{sat}(T_0)/P_{atm}$ ratio. Our region of interest is in region 2 (low to moderate degree of metastability). The speed of sound in two-phase mixtures is generally quite low (order of 30 m/s) and thus a two-phase flow can easily reach a supersonic state. Experimental observations of Moreira and co-workers clearly show the presence of shock waves for highly metastable flashing jets.

Based on the work of Simoes-Moreira and Bullard (2003); Simoes-Moreira et al. (2002) we propose the following procedure to compute the source and pseudo-source terms of a flashing jet:

- Assume a degree of metastability π and deduce the pressure P_1 (state 1) at the exit orifice via Equation (3.17). The metastable liquid temperature T_1 is taken equal to the stagnation temperature and the metastable specific volume is the saturated specific volume at the stagnation temperature.

$$\pi = \frac{P_{sat}(T_0) - P_1}{P_{sat}(T_0)} \tag{3.17}$$

- The metastable liquid recovers thermodynamic equilibrium through an evaporation wave at the exit orifice (Simoes-Moreira and Shepherd, 1999). The flow properties downstream of the evaporation wave (state 2) are found by solving the two equations below which correspond to the Chapman-Jouguet solution for

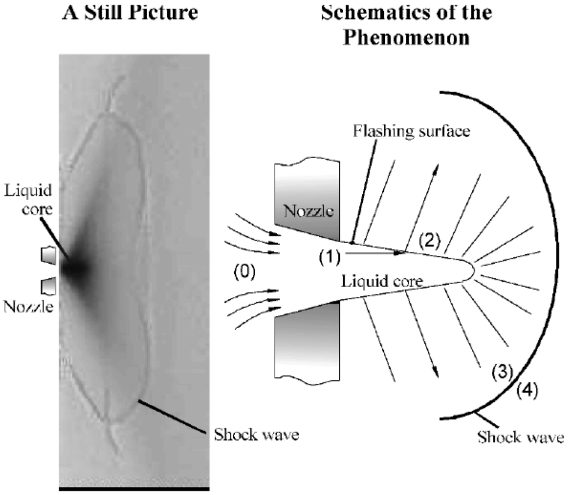

Figure 3.1: *Illustration of an under-expanded flashing jet with shock waves (taken from Simoes-Moreira et al. (2002)).*

evaporation waves (Hahne and Barthau, 2000; Kuznetsov and Vitovskii, 2007):

$$\frac{dv_2}{dT_2} = \frac{v_2 - v_1}{P_2 - P_1}\frac{dP_2}{dT_2} \tag{3.18}$$

$$x_2 = \frac{2\left(H_1 - H_{l,2}\right) + \left(v_{l,2} + v_1\right)\left(P_2 - P_1\right)}{2\left(H_{g,2} - H_{l,2}\right) - \left(v_{g,2} - v_{l,2}\right)\left(P_2 - P_1\right)} \tag{3.19}$$

- The flow downstream of the evaporation wave is sonic and undergoes a further expansion (because $P_2 > P_{atm}$), thus reaching a supersonic state. The supersonic two-phase flow adjusts to atmospheric pressure via shock wave structures. The standard jump equations for a normal shock are solved and the properties of the pseudo-source after expansion are obtained (Simoes-Moreira et al., 2002).

The mass flux is computed from the Chapman-Jouguet solution and the homogeneous mixing rule applies (i.e. $H_2 = x_2 H_{g,2} + (1 - x_2) H_{l,2}$):

$$G = \frac{\sqrt{2\left(H_1 - H_2\right)}}{v_2} \tag{3.20}$$

3.1.7 Inter-model comparison

The predictions of the three approaches (energy balance model, homogeneous non-equilibrium model and model of Moreira *et al.*) for a hypothetical release of propane are compared. This inter-model comparison should allow a better understanding of the strengths and weaknesses of each model. First we consider releases of saturated propane through an orifice of diameter 15 mm attached to a pipe of varying length (see

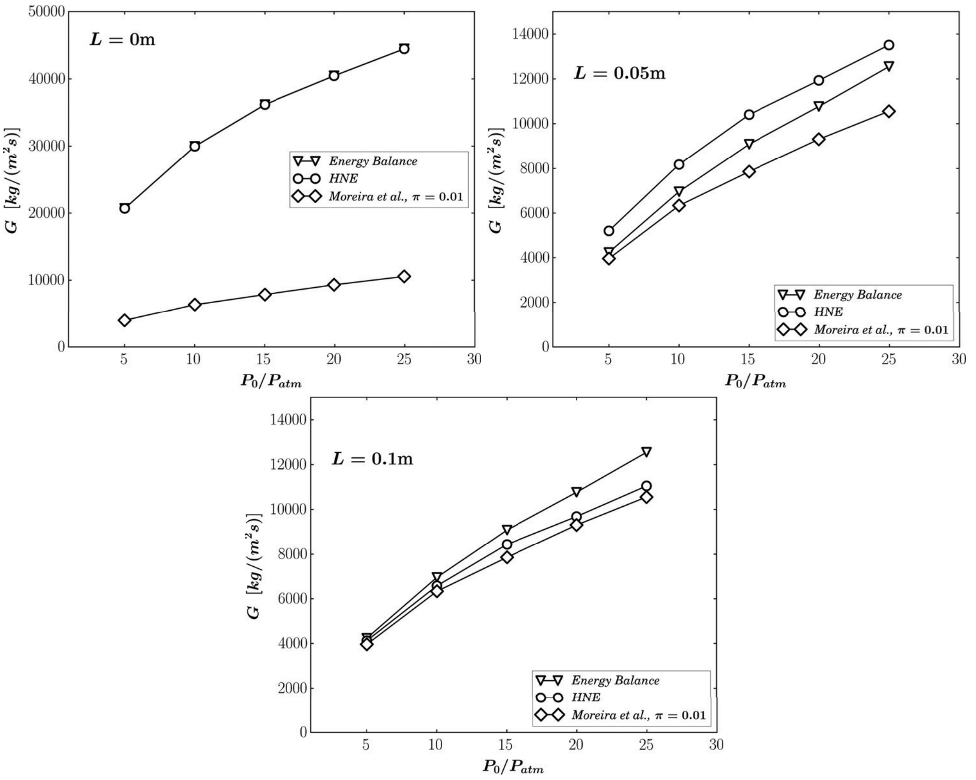

Figure 3.2: *Variation of mass flux with pipe length and storage pressure for different models.*

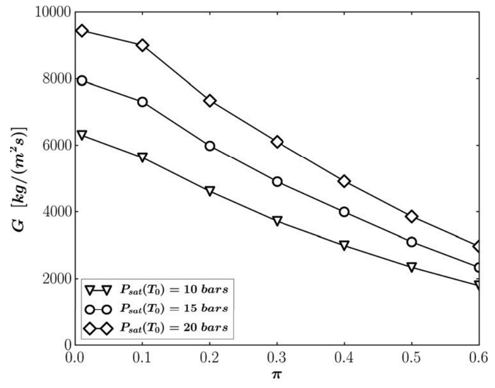

Figure 3.3: *Variation of mass flux with the degree of metastability for different stagnation pressure. The length of the pipe is* 0.1 *m.*

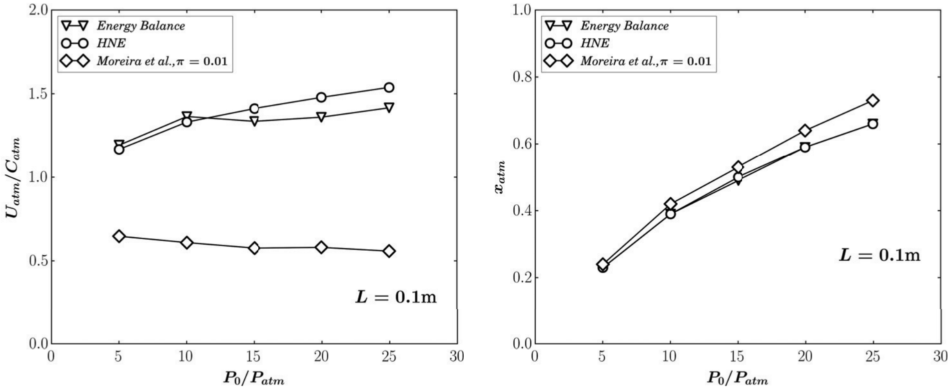

Figure 3.4: *Variation of expanded velocity (left plot) and gas mass fraction (right plot) with stagnation pressure for different models.*

Figure 3.2). The pressure inside the tank is the saturated pressure at the stagnation temperature $P_0 = P_{sat}(T_0)$. For a sharp-edge orifice the energy balance model and the homogeneous non-equilibrium model give the same predictions. These two models, in this case, reduce to the Bernoulli equation 3.1 and predict the maximum possible mass flux. As a consequence of its assumptions (liquid metastability and vapour generation at the exit orifice), for a sharp-edge orifice, the model of Moreira *et al.* predicts mass fluxes that are much lower compared to the mass fluxes obtained with the energy balance and homogeneous non-equilibrium models. As the length of the pipe increases the predictions of the different models converge. This convergence provides a first "validation" of the models. It is important to note that in the model of Moreira *et al.* the physical effects related to the pipe length are not directly taken into account. These effects can be taken into account indirectly via the degree of metastability. The mass fluxes predicted by the model of Moreira *et al.* can be seen as lower asymptotic bounds. The metastability degree has been set to $\pi = 0.01$ in the model of Moreira *et al.* corresponding to a very low degree of metastability. For the same hypothetical propane release, Figure 3.3 shows the variation of the mass flux with the degree of metastability. As the degree of metastability increases, the magnitude of the under-pressure of vaporization increases and thus does the mass fraction of gas generated through the evaporation wave. Therefore, the mass flux decreases when the degree of metastability increases.

The expansion models are now discussed. Two approaches have been presented, one based on a control volume approach omitting the possible presence of shock waves and one approach incorporated inside the model of Moreira *et al.* which tackles the possible presence of shock waves and supersonic two-phase flows. It is worth recalling that in all models we assume homogeneous flows. The speed of sound in homogeneous two-phase mixtures can be estimated by (Brennen, 2005):

$$\frac{1}{c^2} = [\rho_l(1-\alpha_g) + \rho_g \alpha_g] \left[\frac{\alpha_g}{kP} + \frac{(1-\alpha_g)}{\rho_l c_l^2} \right] \tag{3.21}$$

where α_g is the gas volume fraction and $k = 1.4$ is the polytrophic constant. Figure 3.4

shows the predicted velocity and gas mass fraction after expansion. A saturated propane release through a 15 mm orifice diameter and $L = 0.1$ m long pipe is considered. The velocity is normalized by the speed of sound in the mixture after expansion 3.21. The velocities obtained with the energy balance and homogeneous non equilibrium models are larger than the speed of sound given by Equation (3.21) whereas the model of Moreira *et al.* yields subsonic velocities. The values for the speed of sound can be subject to discussions due to the homogeneous flow and perfect gas assumptions. However, based on the current knowledge, we would except to obtain a subsonic flow at the end of the expansion region. The three models give very similar results for the gas mass fraction at the end of the expansion region.

3.2 Spray characteristics

3.2.1 Overview

At the end of the expansion region the flow is two phase and the liquid spray has to be characterized. We assume a homogeneous flow, meaning that the velocity and temperature of the droplets are equal to the velocity and temperature of the surrounding vapour. The drop-velocity and drop-temperature distributions are uniform. The drop-size distribution is not uniform but poly-dispersed. Many types of drop-size distribution exist (Babinsky and Sojka, 2002; Sowa, 1992). The droplets are assumed to be spherical and the droplet diameter is denoted d. The distribution function $f(d)$ gives the number of droplets having diameter d. For the mathematical description of distributions we refer to Crowe et al. (1998). Some analytical approaches exist to derive drop-size distribution and we can cite for example the Maximum Entropy Formalism and the review by Dumouchel (2009). However, currently we must mostly rely on empirical based approaches to predict drop-size distributions. The Sauter Mean Diameter is often used to characterise a liquid spray. The Sauter Mean Diameter is an average droplet diameter which is proportional to the ratio of the total liquid volume in a spray to the total droplet surface area in a spray. It is denoted d_{32} and computed via:

$$d_{32} = \frac{\int_0^\infty d^3 f(d)\mathrm{d}d}{\int_0^\infty d^2 f(d)\mathrm{d}d} \tag{3.22}$$

The general expression for an average droplet diameter d_{mn} is:

$$d_{mn} = \left(\frac{\int_0^\infty d^m f(d)\mathrm{d}d}{\int_0^\infty d^n f(d)\mathrm{d}d}\right)^{\frac{1}{m-n}} \tag{3.23}$$

The number mean diameter or mean of the distribution $f(d)$ is denoted d_{10}. Four models and correlations that predict the Sauter Mean Diameter are presented and tested in the following sections. Two drop-size distributions, namely the log-normal distribution and the Rosin-Rammler distribution, are also discussed. The log-normal distribution is recommended by the CCPS model (Johnson and Woodward, 1999) whereas the Rosin-Rammler distribution is recommended by Witlox et al. (2010). The chapter ends with an inter-model comparison for an hypothetical release of propane.

3.2.2 The CCPS model

The CCPS model is described in Johnson and Woodward (1999). There exists two main mechanisms for liquid atomization: mechanical break-up and flash atomization. The representative diameter for droplets formed by the mechanical break-up process is denoted d_{p1} and the representative diameter for droplets formed by the flash atomization process is denoted d_{p2}. The representative diameter of the spray is taken as:

$$d_{pn} = min\left(d_{p1}, d_{p2}\right) \tag{3.24}$$

Drop break-up by aerodynamic forces has been observed to occur when the drop Weber number attains a critical value between 10 and 20 (Clift et al., 2005). The droplet Weber number is expressed as the ratio of the aerodynamic force acting on the surface of the droplet and the liquid surface tension force. The representative diameter associated with the mechanical break-up process is given by:

$$d_{p1} = \frac{We_c \sigma}{\rho_a U_{atm}^2} \tag{3.25}$$

where ρ_a is the air density and u_{atm} is the expanded velocity of the jet which is assumed to be equal to the relative velocity between the drop (a more appropriate term would be liquid sheet since the process of atomization is on-going) and the ambient. Johnson and Woodward (1999) take the base value of 10 for the critical Weber number.

For the flash-atomization process an acceleration velocity is first defined as the difference between the exit velocity and the expanded velocity:

$$U_{acc} = U_{atm} - U_{ori} \tag{3.26}$$

Then a relative velocity is introduced as the vector sum of the acceleration velocity and a bubble growth velocity:

$$U_{rel} = \left(U_{acc}^2 + U_{bub}^2\right)^{1/2} \tag{3.27}$$

The bubble velocity is derived from a simplified version of the theory of flashing break-up by bubble growth (Forester and Zuber, 1954; Lienhard and Day, 1970). Flash atomization is assumed to occur by rapid growth of bubbles in the super-heated liquid after a small induction period (Johnson and Woodward, 1999). The expression for the bubble growth velocity writes:

$$U_{bub} = \phi^2 C_{bub}^2 N_d^{1/3} \tag{3.28}$$

where N_d is the nucleation site density in the liquid and ϕ is an adjustable correction factor for finding the bubble growth rate (Johnson and Woodward, 1999). These two parameters are thus tuning constants for the model. The recommended values are $N_d = 10^{10}\ {}^{\text{sites}}\!/_{m^3}$ and $\phi = 1$. The bubble growth rate C_{bub} is expressed as a function of the Jacob number and liquid thermal diffusivity:

$$C_{bub} = \frac{C_{p_l}\left(T_{ori} - T_{nbp}\right)\rho_{l,atm}}{H_{gl,atm}\rho_{g,atm}}\left(\pi\gamma_l\right)^{1/2} = Ja\left(\pi\gamma_l\right)^{1/2} \tag{3.29}$$

Finally, the expression for the representative drop size d_{p2} is similar to the one used for d_{p1} (the same value of the critical Weber number is recommended):

$$d_{p2} = \frac{We_c \sigma}{\rho_g U_{rel}^2} \tag{3.30}$$

The representative diameter d_{pn} is the number median of a log-normal distribution. A very useful relationship for the manipulation of the log-normal distribution is (Crowe et al., 1998):

$$d_{pn}^k e^{\ln(\sigma_G)^2 k^2/2} = \int_0^\infty d^k f(d)\mathrm{d}d \tag{3.31}$$

Thus, the Sauter Mean Diameter is obtained from the equation below with the recommended value of 1.8 for σ_G (Johnson and Woodward, 1999):

$$SMD = d_{pn} e^{2.5\ln(\sigma_G)^2} \tag{3.32}$$

3.2.3 The correlation of Witlox *et al.*

Witlox et al. (2010) and Kay et al. (2010) report the results of experiments on releases of pressurized liquefied gases. The work was divided in three phases. The first phase consisted in a literature review on flashing jets (Witlox and Bowen, 2002) and the two last phases dealt with experimental work and the derivation of correlations for the prediction of droplet sizes (Cleary et al., 2007; Witlox et al., 2007). Releases of sub-cooled and superheated water, cyclohexane, butane, propane and gasoline were conducted. Effects on droplet sizes of different storage conditions, nozzle diameters and pipe length to nozzle diameter ratios were investigated. A non-intrusive optical measurement technique, namely a Phase Doppler Anemometer (PDA) system was used. Data for droplet sizes are presented as global Sauter Mean Diameter (*SMD*) at one location downstream of the nozzle. The authors assume that at the picked downstream location complete atomization of the jet had occurred and no investigation of the break-up length is reported. Witlox et al. (2010) provide an empirical correlation for the *SMD* of the spray. They propose that the variation of the *SMD* with the degree of superheat can be split into three distinct regimes that can be modelled separately: mechanical break-up, transition to flashing and fully flashing. In the first regime, the mechanical break-up regime, the superheat is low and the *SMD* values are rather large. In this regime the *SMD* is expressed as a function of the aspect ratio L/D_{ori}, the liquid Reynolds number $Re_{l,ori}$ and the liquid Weber number $We_{l,ori}$:

$$\begin{aligned} \frac{SMD}{D_{ori}} &= 74 We_{l,ori}^{-0.85} Re_{l,ori}^{0.44} \left(\frac{L}{D_{ori}}\right)^{0.114} \left(\frac{\mu_{l,ori}}{\mu_{water,stp}}\right)^{0.97} \\ &\quad \left(\frac{\sigma_{l,ori}}{\sigma_{water,stp}}\right)^{-0.37} \left(\frac{\rho_{l,ori}}{\rho_{water,stp}}\right)^{-0.11} \end{aligned} \tag{3.33}$$

The subscripts (l,ori) refer to liquid properties taken at exit conditions and the subscripts $(water,stp)$ indicate properties of water taken at standard temperature and pressure (1 atm and 273 K). Cut-off values $L/D_{ori} = 0.1$ and $L/D_{ori} = 50$ are applied.

The second regime, namely the transition to fully flashing, starts when the superheat attains the value defined by:

$$T_{sh_A} = 48 \frac{H_{lg,ori}\rho_{v,ori}}{C_{p_{l,ori}}\rho_{l,ori}} We_{v,ori}^{-1/7} \phi^{-1} \tag{3.34}$$

and ends at the value:

$$T_{sh_B} = 108 \frac{H_{lg,ori}\rho_{v,ori}}{C_{p_{l,ori}}\rho_{l}} We_{v,ori}^{-1/7} \phi^{-1} \tag{3.35}$$

where $We_{v,ori} = \rho_{v,ori}U_{ori}^2 D_{ori}/\sigma_{l,ori}$ and $\phi = 1 - e^{-2300\rho_{v,ori}/\rho_{l,ori}}$. The third regime, the fully flashed regime, starts at point B and the fully flashed SMD is taken to be 80 μm. Beyond the point B the SMD decreases at a constant rate of 0.1 μm/K until a cut-off value of 10 μm is reached. It is important to note that this correlation is an empirical correlation. Its derivation is based on a particular set of experiments. Therefore, the application of this correlation outside the range of initial conditions covered in the experiments is questionable. We refer to Kay et al. (2010) for the experimental conditions tested.

In addition to the correlation for the SMD, Witlox et al. (2010) have also proposed a droplet size distribution correlation. The distribution follows the form of a Rosin-Rammler distribution:

$$F_m(d) = 1 - e^{-a_{RR}(d/SMD)^{b_{RR}}} \tag{3.36}$$

In Equation (3.36), $F_m(d)$ represents the mass fraction of droplets with diameter less than d. In the mechanical break-up region and fully flashed region the coefficients a_{RR} and b_{RR} take constant values: $a_{RR} = 0.4, b_{RR} = 2.0$ in the first region and $a_{RR} = 0.79, b_{RR} = 0.97$ in the fully flashed region.

3.2.4 The CCPS correlation

The derivation of the CCPS correlation for the Sauter Mean Diameter is based on both experimental observations and numerical predictions (Johnson and Woodward, 1999). The CCPS experiments consisted of releases of five different chemicals and measurements of subsequent rain-out, see Chapter 2. For a given test, the Unified Dispersion Model (UDM) (Woodward and Papadourakis, 1995) was used to estimate the SMD of the spray so that as to match the CCPS experimental measurement of rain-out. This procedure was repeated for each of the tests. Then, different correlators were tested in order to develop a correlation that would predict the above mentioned set of $SMDs$. The best correlator was found to be the partial expansion energy expressed as:

$$E_p = -\triangle H - v_0\left(P_{sat}(T_0) - P_{atm}\right) + v_0\left(P_0 - P_{sat}(T_0)\right) \tag{3.37}$$

and the correlation writes:

$$SMD = \begin{cases} 823 \times 10^{-6} - 72.1 \times 10^{-6}\ln(E_p) & \text{if } E_p < 89400 \\ 1.0 \times 10^{-6} & \text{otherwise} \end{cases} \tag{3.38}$$

However, as pointed out in (Witlox et al., 2007), the CCPS correlation has to be used in connection with an isentropic expansion model. In this work, the two expansion models that are tested are not isentropic. The control volume approach is isenthalpic and Britter (1995) has shown that the isenthalpic assumption for the expansion region of flashing jets gives better results than the isentropic assumption. Consequently, the CCPS correlation will not be considered further in this work.

3.2.5 The model recommended in the Yellow Book

The Yellow book (van den Bosch and Weterings, 1997) recommends a model based on the work of Appleton (1984). In his work Appleton (1984) compared the predictions of his model with data from an experiment involving releases of water-steam mixtures and he found reasonably good agreement (van den Bosch and Weterings, 1997). As in the CCPS model, the two shattering mechanisms (mechanical break-up and flash atomization) are competing. For flash atomization to rule over mechanical break-up the exit temperature has to exceed a shatter temperature, $T_{shatter}$, defined as:

$$\frac{T_{shatter} - T_{nbp}}{T_{shatter}} = C_{shatter} \tag{3.39}$$

where $C_{shatter}$ is in the range $0.07 - 0.1$ (van den Bosch and Weterings, 1997). The correlation for the SMD writes:

$$SMD = \begin{cases} 3.78 r_{atm} \left(1 + 3\frac{We^{1/2}}{Re}\right)^{1/2} & \text{if } We < Re^{-0.45} \times 10^6 \text{ and } T_{ori} < 1.11 T_{nbp} \\ (We_c \sigma) / \left(U_{atm}^2 \rho_a\right) & \text{otherwise} \end{cases} \tag{3.40}$$

The critical Weber number is set to a recommended value of 15, r_{atm} is the radius of the jet after expansion and the Reynolds and Weber numbers are based on post-expansion properties:

$$Re = \frac{2 r_{atm} U_{atm}}{\nu_{l,atm}} \quad We = \frac{2 r_{atm} U_{atm}^2 \rho_{l,atm}}{\sigma} \tag{3.41}$$

In the Yellow book (van den Bosch and Weterings, 1997) the distribution of droplet diameters is assumed to be uniform.

3.2.6 Inter-model comparison

We compare the predictions given by the models and correlations for the spray *SMD*. A hypothetical saturated propane release is considered. The orifice diameter is 15 mm and the pipe length is 0.1 m. The mass flow rate and jet expansion are either computed with the energy balance model or with the Moreira *et al.* model. The results obtained with the homogeneous non equilibrium model are very similar to the ones obtained with the energy balance model. Figure 3.5 clearly shows that the correlation of Witlox *et al.* predicts larger *SMDs* than the "physically based models". The *SMDs* are decreasing with increasing $P_0/P_{atm} = P_{sat}(T_0)/P_{atm}$ ratio and thus with increasing degree of stagnation super-heat $T_{sh,0} = T_0 - T_{nbp}$. Because the Moreira *et al.* model, compared to the energy balance model, provides lower, subsonic, velocities at the end of the expansion region, the *SMDs* predicted by the "physically based models" are slightly larger.

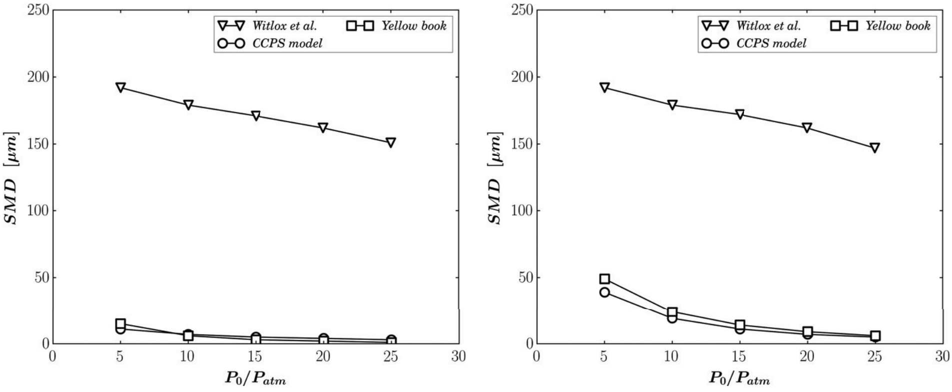

Figure 3.5: *Variation of SMD with stagnation pressure. The energy balance model has been used to compute the mass flow rate and jet expansion in the left plot and the Moreira et al. model has been used in the right plot.*

3.3 Comparisons with experimental data

3.3.1 Mass flow rate

The first comparison with experimental data is made for a single phase, sub-cooled water discharge through pipes of varying lengths. This case can be seen as the base case, the most "simple" case. The data are from Uchida and Nariari (1966) who used a 4 mm diameter pipe. The water was stored at a temperature of $T_0 = 293\,\mathrm{K}$ under 4 different pressures. The comparison is carried out with the energy balance model only since the two other models do not account for pipe friction and are not designed for single phase releases. Figure 3.6 shows that the predictions of the energy balance model match experimental data reasonably well for all storage pressures and for pipe length up to $L = 1$m. Some discrepancies appear at $L = 2.5\,\mathrm{m}$ and could be due to a failure of the correlation for pipe friction.

The second comparison is made with the data of Sozzi and Sutherland (1975) who measured flashing water discharge rates through pipes of diameter 12.7 mm. The water was stored under saturated conditions and the temperature ranged between 540 and 550 K. The energy balance model gives the overall best predictions as it can be observed on Figure 3.6. The mass fluxes predicted by the homogeneous non-equilibrium model are smaller than the ones predicted by the energy balance model for pipe lengths $0 < L < 0.1$ m. The Moreira *et al.* model acts as a lower asymptotic bound.

van Den Akker et al. (1983) released saturated refrigerant 12 through short pipes. The comparison with the data of van Den Akker et al. (1983) confirms that the energy balance model is the most accurate model and that the homogeneous non-equilibrium model under-estimates mass fluxes for pipe lengths in between 0.005 m and 0.03 m (see Figure 3.7). The under-estimation could be due to the non-equilibrium correction term. The model of Moreira *et al.* has also been used to simulate the experiments of van Den Akker et al. (1983). On Figure 3.8 a very good agreement is seen between predictions and observations for the scenario with the longest pipe length $L = 150\,\mathrm{mm}$.

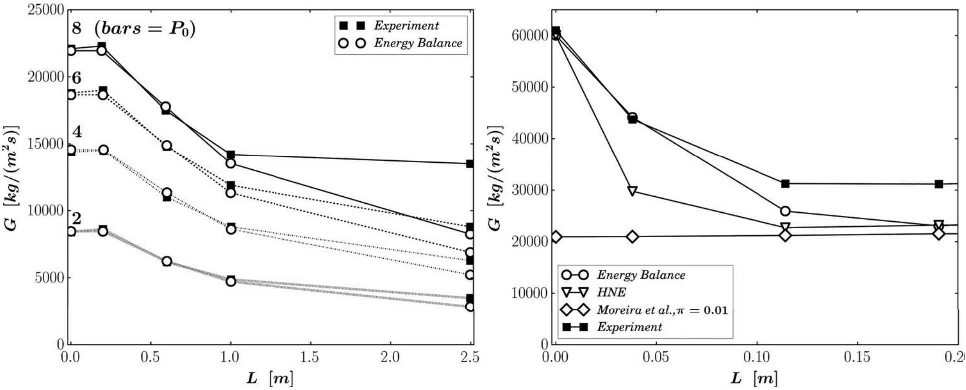

Figure 3.6: ***Left plot***: *predicted and measured mass fluxes for the experiments of Uchida and Nariari (1966).* ***Right plot***: *predicted and measured mass fluxes for the experiments of Sozzi and Sutherland (1975).*

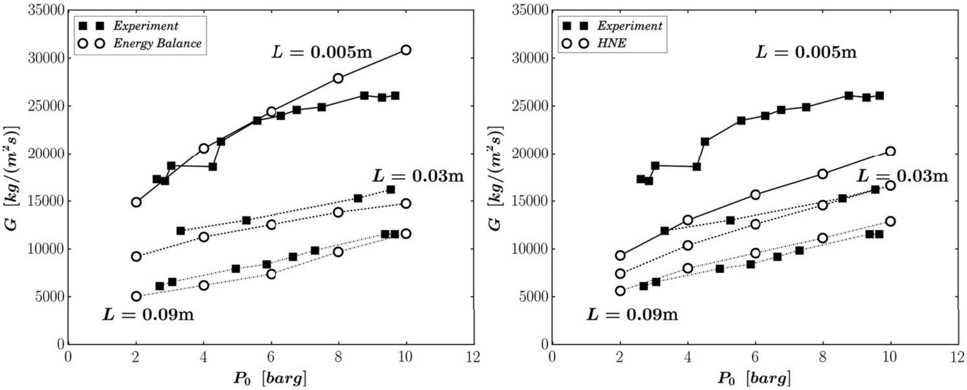

Figure 3.7: *Predicted and measured mass fluxes for the experiments of van Den Akker et al. (1983). The predictions are made with the energy balance model and homogeneous non-equilibrium model.*

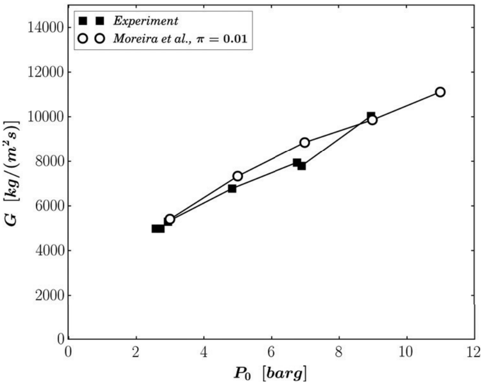

Figure 3.8: *Predicted and measured mass fluxes for the experiment of van Den Akker et al. (1983). The length of the pipe is 0.15 m and the predictions are made with the model of Moreira et al..*

Mass flow rates were also measured during the FLIE-INERIS experiments (Bonnet et al., 2005). The conversion of mass flow rates to mass fluxes has been done by using a discharge coefficient of $C_D = 0.62$. In Figure 3.9 we consider propane releases through orifices with diameters 2, 5, 10, 15, 20 and 25 mm. The same experimental set-up was used for all tests. First we try to interpret the experimental observations. In Figure 3.9 a clear variation of the mass flux with orifice diameter is noted. The dependence shown in Figure 3.9 is not "exact" in the sense that the stagnation pressure was not the same for all the tests. The pressure variation was however moderate from one test to another. For example, for the test with $D_{ori} = 2\,\text{mm}$ the stagnation pressure was $P_0 = 8\,\text{bar}$ with $P_0/P_{sat}(T_0) = 1.3$; and for the test with $D_{ori} = 15\,\text{mm}$ the stagnation pressure was $P_0 = 9\,\text{bar}$ and $P_0/P_{sat}(T_0) = 1.33$. Increasing the stagnation pressure should yield to an increase in the mass flux (see Figure 3.2). However, in this case the experimental data show that the mass flux is decreasing when the stagnation pressure increases (the mass flux for the 2 mm diameter with $P_0 = 8\,\text{bar}$ is $22589\,\text{kg}/\text{m}^2\text{s}$ and for the 15 mm diameter with $P_0 = 9\,\text{bar}$ the mass flux is $14600\,\text{kg}/\text{m}^2\text{s}$). Note that the two tests have the same degree of subcooling. We conclude that the orifice diameter must have an effect on the mass flux. The orifice diameter should be compared to the pipe diameter. When the ratio D_{ori}/D_p increases, phase change is facilitated, the flow is likely to be two-phase at the exit orifice and thus the mass flux decreases. Now the numerical predictions are discussed. The results obtained with the energy balance model with $L = 1.7\,\text{m}$ compare very well with experimental data for orifice diameters ranging from 2 mm to 10 mm but over-estimate the data for diameters ranging from 15 mm to 25 mm. It indicates that the ratio D_{ori}/D_p starts to affect the mass flux at around $D_{ori}/D_p = 0.2 - 0.3$. In the energy balance model we take this effect into account by increasing the length of the pipe. By doubling the length of the pipe the predictions of the energy balance model match the experimental data. The sharp-edge orifice predictions are conservative but largely over-estimate mass fluxes for $D_{ori}/D_p > 0.3$. For $D_{ori}/D_p < 0.2$ the sharp-edge orifice assumption is satisfying. Finally, we note that the estimate given by by the model of Moreira *et al.* agrees well with experimental observation for $D_{ori} = 25\,\text{mm}$

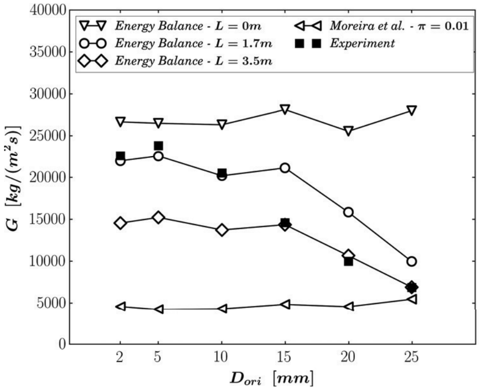

Figure 3.9: *Predicted and measured mass fluxes for the FLIE-INERIS experiments.*

3.3.2 Spray characteristics and expansion region

Two experiments are used to validate the models for jet expansion and spray characteristics: the Von-Karman Institute (VKI) flashing jets experiment (Yildiz et al., 2004) and the FLIE-INERIS experiments (Bonnet et al., 2005). These experiments have been extensively presented and discussed in Chapter 2. Figure 3.10 shows the predicted and measured velocities and *SMD* for a VKI test: release of refrigerant R134 through an orifice of 5 mm diameter with $P_0 = 6.63$ bars and $T_0 = 298$ K. The pipe length was not reported and from pictures of the experimental set-up a pipe length of $L = 0.1$ m is assumed. The measured velocity corresponds to the mean velocity of the droplets. Assuming homogeneous flow, the droplet mean velocity should be equal to the gas phase velocity. It is worth noting that the measured velocity increases until around $20D_{ori}$ and that over the same distance a sharp decrease in the measured *SMD* is observed. It indicates that the expansion and the atomization of the jet might be complete only at a distance of $20D_{ori}$ downstream of the exit orifice. This is an estimation of the break-up length for a flashing jet. The experimental expanded velocity is taken to be the measured velocity at $20D_{ori}$. The experimental expanded velocity compares well with the prediction of the Moreira *et al.* model. The energy balance model largely over-estimates the observed expanded velocity (it gives an expanded velocity of 94 m/s) which demonstrates the importance of shock waves effects in this case. We now turn to the prediction of the *SMD* for the same VKI test. The *SMD* obtained from the models corresponds to the "expanded *SMD*" and should be compared with the *SMD* measured at $20D_{ori}$. The comparison is only conducted with the model of Moreira *et al.* since this model gives the best prediction for the expanded velocity. All models give the correct order of magnitude for the *SMD*. The two best predictions are from the correlation of Witlox et al. (2010) and from the model recommended by the Yellow Book.

As far as the mass distribution of droplet diameters is concerned, the Yellow book (van den Bosch and Weterings, 1997) assumes a uniform distribution and the correlation of Witlox et al. (2010) provides a Rosin-Rammler distribution (see Equation (3.36)). The distribution is of course not uniform. The distribution measured during

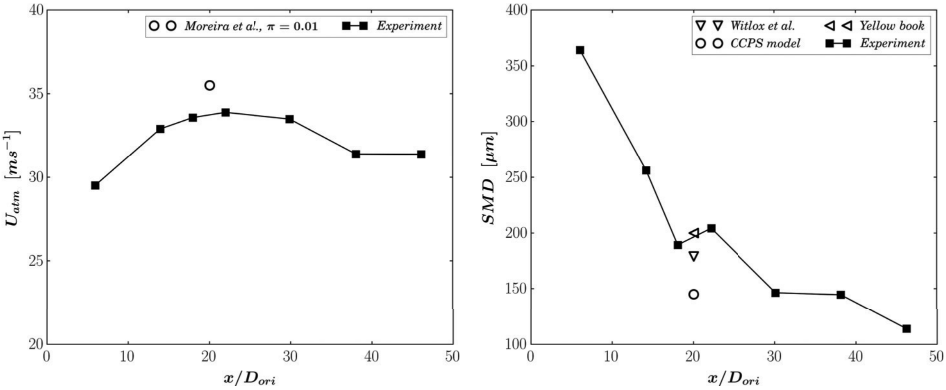

Figure 3.10: *Comparison between predicted and measured expanded velocity and Sauter Mean Diameter for the VKI test.*

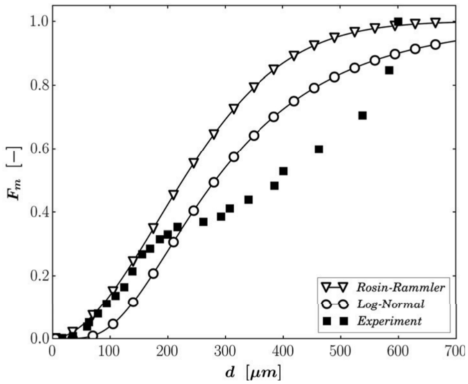

Figure 3.11: *Comparison between measured and predicted mass droplet distributions* $20D_{ori}$ *downstream of the exit orifice for the VKI test.*

the VKI test at $20D_{ori}$ downstream of exit orifice is compared with the Rosin-Rammler distribution of Witlox et al. (2010) and with the log-normal distribution as proposed in the CCPS model Johnson and Woodward (1999). The log-normal distribution is used in connection with the *SMD* predicted by the model recommended in the Yellow Book. Both distributions give satisfying predictions. The Rosin-Rammler distribution follows almost perfectly the measured distribution until $d = 200\,\mu$m and then the slope of the measured distribution changes drastically. This change of slope is also observed in the measured FLIE-INERIS distribution (see Figure 3.13) and could be due to a failure of the PDA (Phase Doppler Anemometer) in measuring large droplets size. In Witlox et al. (2010), referring to large scale flashing jets of butane, it is said that the maximum droplet size that could be measured was around 700-800 μm. The authors add that larger droplets may be missed resulting in a possibly inaccurate droplet volume distribution. This observation could partly explains the deviations between the predicted and observed mass distribution. Bigot et al. (2005) have also discussed the importance of large drops in estimating the Sauter Mean Diameter and drop-size distribution. Bigot et al. (2005) released superheated water through different orifice sizes and shapes and a PDA system allowed the measurement of droplets size and velocity. They observed that, on one hand, the large drops play a predominant role in the computation of the *SMD* because of their large volume to surface ratio; and on the other hand, the number of large drops detected by the measuring device is quite small compared to the total number of droplets in a sample. As a consequence, in Bigot et al. (2005), the experimental uncertainty in the value of the *SMD* is estimated to be around 100 μm for a sample of 3000 droplets. This is a quite large uncertainty compared to common *SMD* values (between 100 and 300 μm). Moreover, Bigot et al. (2005) also note that the small droplets, i.e. in the range 0-150 μm, represent a large number of the droplet population (for example more than 90 % when the storage temperature is larger than 136 °C) but they account for only a few percent of the mass released (from 0.5 % to 17 %). The large droplets (diameter greater than 150 μm) on the other hand, transport the rest of the mass, between 83 % and 99 % in the experiments discussed here. Therefore, roughly 10 % of the droplets contain more than 85 % of the liquid mass.

One of the FLIE-INERIS experiment is now discussed. A release of propane through a 2 mm diameter orifice attached to a pipe of diameter $D_p = 0.05$ m is considered. The stagnation conditions were $P_0 = 8.1$ bar and $T_0 = 282$ K. The mass flow rate was measured and taking a value of $C_D = 0.62$ for the discharge coefficient we obtain a value of $G_{exp} = 22589\,{}^{\mathrm{kg}}\!/\!{}_{m^2\mathrm{s}}$ for the mass flux. Assuming a sharp-edge orifice, the energy balance model predicts a mass flux of $G_{EB} = 26662\,{}^{\mathrm{kg}}\!/\!{}_{m^2\mathrm{s}}$ in satisfying agreement with the experimental measurement. On the other hand the model of Moreira *et al.* largely under-estimates the mass flux, $G_{Moreira} = 4584\,{}^{\mathrm{kg}}\!/\!{}_{m^2\mathrm{s}}$. Therefore, the propane was in the liquid state at the exit orifice and flashing occurred outside. The energy balance model and the associated expansion model (see Equations 3.14, 3.15 and 3.16) predict a value of $46\,{}^{\mathrm{m}}\!/\!{}_{\mathrm{s}}$ for the expanded velocity, in satisfying agreement with the experimental value (see Figure 3.12). As far as the *SMD* value is concerned, the CCPS model yields the best estimation. Turning to the distribution of droplet diameters, we note that the FLIE-INERIS experimental distribution has a shape which is similar to the shape of the VKI experimental distribution. The computed distribution is a log-normal distribution has recommended in the CCPS model (Johnson

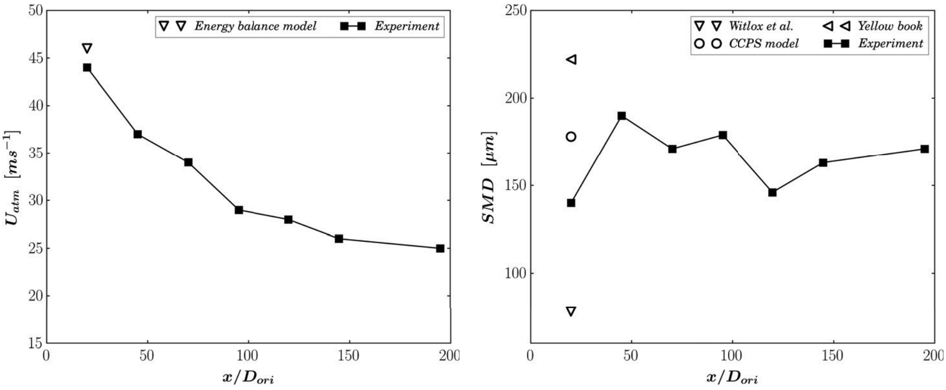

Figure 3.12: *Comparison between predicted and measured expanded velocity and Sauter Mean Diameter for the FLIE-INERIS test.*

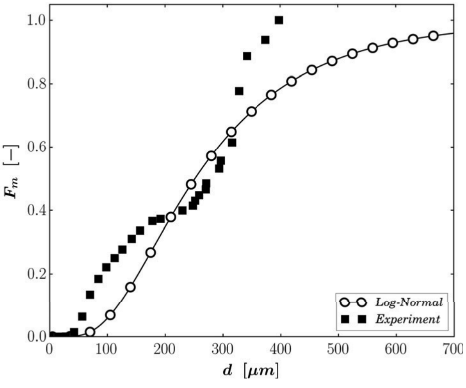

Figure 3.13: *Comparison between measured and predicted droplet distributions* $20D_{ori}$ *downstream of the exit orifice for the INERIS test.*

and Woodward, 1999). There is a relatively good agreement between the predictions and the observations for small to moderate diameters but the discrepancies are large (as for the VKI experiment) for the biggest droplets.

3.3.3 Conclusions

The performances of several models in estimating the pseudo-source of releases of pressurized liquids have been assessed. The energy balance model, the homogeneous non-equilibrium model and the model proposed by Moreira *et al.* have been used to predict the mass flow rate at the exit orifice. The mass flow rate is a critical parameter in risk analysis studies. It controls the quantity of chemical released into the atmosphere. A conservative model must be employed. The energy balance model gives conservative predictions for the mass flow rate with a satisfying degree of accuracy. The flash expansion of the jet is computed with Equations 3.14, 3.15 and 3.16, the CV approach. The CV approach is the approach recommended and widely used in the literature (Britter et al., 2011). We have shown that it might be needed to account for shock wave effects in the expansion region. However, further work is necessary before shock wave models in two-phase flows could be employed for risk analysis studies. As far as the characteristics of the droplets are concerned, additional theoretical and experimental works are needed in order to gain confidence in model and correlation predictions. We have shown that large differences can exist in the predictions. For drop size, we recommend to use a mean of model predictions and perform sensitivity studies to see how the drop size affects the results.

Chapter 4

Single phase turbulent jet flows

4.1 Turbulent flow modelling in the FLACS model

4.1.1 Presentation of the FLACS CFD solver

The FLACS model solves the compressible conservation equations for mass, momentum, enthalpy and mass fraction of species on a 3D Cartesian grid using a finite volume method. Hjertager (1985, 1986) describes the basic equations used in the FLACS model and Hjertager et al. (1988a,b) present the results of explosions experiments used to develop and validate the FLACS model initially. The numerical model uses a second order central differencing scheme for resolving diffusive fluxes and a second order "kappa" scheme (hybrid scheme with weighting between 2^{nd} order upwind and 2^{nd} order central difference, with delimiters for some equations) to resolve the convective fluxes. The solver is implicit in nature. The time stepping scheme used in the FLACS model is a first order backward Euler scheme. Based on extensive validation, guidelines for time stepping have been established in order to get accurate results. These are based on CFL (Courant-Friedrich-Levy) numbers based on speed of sound and flow velocity. The discretized equations are solved using the BiCGStab iterative method with the SIMPLE pressure correction algorithm (Versteeg and Malalasekera, 2007).

The FLACS model uses a distributed porosity concept which enables the detailed representation of complex geometries using a Cartesian grid. Large objects and walls are represented on-grid and smaller objects are represented sub-grid. Geometrical details can be characterized while maintaining reasonable simulation times. Geometrical details are represented as porosities for each control volume. Each control volume is then fully open, fully blocked or partly blocked. For partly blocked control volumes, the porosity is defined as the fraction of the volume that is available for fluid flow. Subgrid objects contribute to flow resistance and turbulence generation, and the geometry representation has been optimized so that the dependency on grid size, shape and translation is as low as possible. We refer to Arntzen (1998) for further details on the porosity concept and its implementation in the FLACS model.

4.1.2 A brief introduction to turbulence theory

Before discussing the details of the turbulence model used in the FLACS model we give a brief introduction to turbulence theory and turbulence modelling. In a turbulent flow

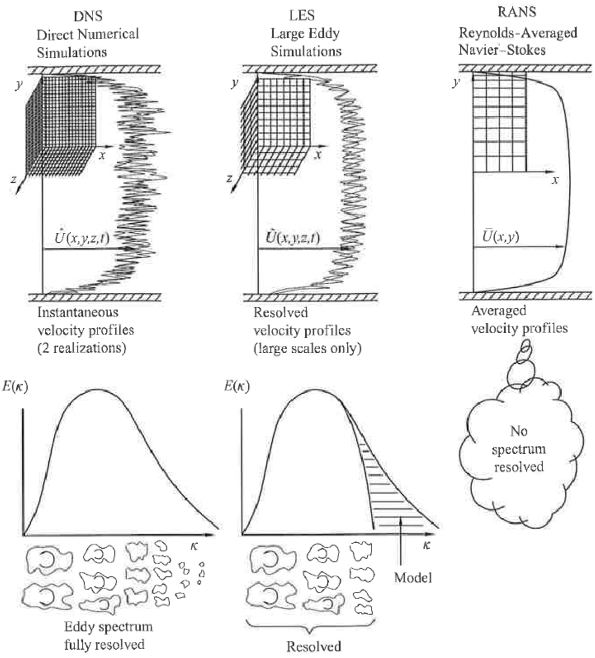

Figure 4.1: *Illustration of the level of details in the DNS, LES and RANS modelling techniques. The example of a fully developed pipe flow is considered. The top plots show the instantaneous velocity profile obtained with DNS, the filtered profile obtained with LES and the averaged profile obtained with RANS. The energy spectrum shows the size of the scales which are resolved by each of the modelling techniques (taken from Hanjalic and Launder (2011)).*

the instantaneous velocity field $\mathbf{U}(\mathbf{x},t)$ is 3D, time dependent and random. Turbulent flows are characterized by a broad range of scales. The largest scales of the flow are as large as the geometrical obstructions present in the flow field, let's denote them L, and the smallest scales of the flow, η vary as (Pope, 2000):

$$\eta \sim Re_L^{-3/4} \tag{4.1}$$

where Re_L is the Reynolds number based on the large scale of the flow L. Therefore, if we consider the flow around an obstruction of size L, as the Reynolds number increases (corresponding to either an increase in the velocity or a decrease in the viscosity) the smallest scale of the flow decreases and thus the range of scales one has to resolve is getting broader. The energy spectrum illustrated in Figure 4.1, shows the distribution of energy in wavenumber space among the various scales of a turbulent flow. Most of the energy is initially contained into the large scale eddies and it is transferred to the small scale eddies via a cascade-like process through the inertial subrange. The energy is finally dissipated by the small scale eddies. Therefore, if one wants to solve exactly a turbulent flow field, one has to resolve the whole range of scales and perform a Direct Numerical Simulation (DNS). The DNS solves numerically the Navier-Stokes equations but its application is limited to low-Reynolds number flows due to the dependence of η on Re_L (Equation (4.1)). For now, DNS cannot be used to simulate practical, engineering, high Reynolds number flows. A modelling step is necessary to make engineering computations feasible. There exists merely two modelling approaches: the Large Eddy Simulation (LES) approach and the Reynolds Averaged Navier Stokes (RANS) approach.

In the LES method the large scale eddies are resolved and the effects of the small scale eddies (mostly the dissipation of turbulent energy) are modelled. Spatial filtering is employed to separate the resolved from the unresolved scales. The LES approach is well suited to handle bluff-body flows such as the flow around buildings or in urban areas. Some engineering or large-scale scenarios can be treated with the LES approach (Harms et al., 2011; Salim et al., 2011). In the FLACS model a RANS approach is used. The RANS approach is based on an ensemble average of the Navier-Stokes equations. An ensemble average is obtained by performing an average over N realizations of the same turbulent flow field; i.e. the N turbulent flow fields have the same initial and boundary conditions. The averaging procedure gives rise to the turbulent closure problem by producing six new unknowns, the turbulent Reynolds-stresses. The instantaneous flow field can be decomposed into a mean flow field and a fluctuating flow field. This is called the Reynolds decomposition and for the velocity field it gives:

$$U_i^{inst} = u_i + \overline{U_i} \quad i = 1,2,3 \tag{4.2}$$

where u_i is the fluctuating velocity and $\overline{U_i}$ is the mean velocity. In the following the over-bar is omitted in the notation of the mean velocities and for simplification we note $\overline{U_i} := U_i$. When there could be some confusion between averaged and instantaneous values the over-bar would be inserted. The compressible Reynolds Averaged Navier Stokes equations write:

$$\frac{\partial}{\partial t}(\beta_v \rho) + \frac{\partial}{\partial x_j}(\beta_j \rho U_j) = S_{m_{p\to f}} \tag{4.3}$$

$$\begin{aligned} \frac{\partial}{\partial t}(\beta_v \rho U_i) + \frac{\partial}{\partial x_j}(\beta_j \rho U_i U_j) &= -\beta_v \frac{\partial P}{\partial x_i} + \frac{\partial}{\partial x_j}(\beta_j \tau_{ij}) \\ &\quad - \frac{\partial}{\partial x_j}(\beta_j \rho \overline{u_i u_j}) \\ &\quad + S_o + \beta_v (\rho - \rho_0) g_i + \rho S_{U_{p\to f},i} \end{aligned} \tag{4.4}$$

$$\frac{\partial}{\partial t}(\beta_v \rho H) + \frac{\partial}{\partial x_j}(\beta_j \rho U_j H) = \frac{\partial}{\partial x_j}\left(\beta_j \rho \overline{h u_j}\right) + \beta_v \frac{DP}{Dt} + \dot{q} + S_{H_{p\to f}} \tag{4.5}$$

where H is the mean specific enthalpy of the fluid, S_o is the source term accounting for the flow resistance due to the presence of subgrid objects, β_v and β_j are the volume and area porosities of the cell respectively. For a compressible Newtonian fluid the stress tensor τ_{ij} writes:

$$\tau_{ij} = \mu \left(\frac{\partial U_i}{\partial x_j} + \frac{\partial U_j}{\partial x_i} - \frac{2}{3} \frac{\partial U_k}{\partial x_k} \delta_{ij} \right)$$

The source terms $S_{m_{p\to f}}$, $S_{U_{p\to f},i}$ and $S_{h_{p\to f}}$ model the effects of the dispersed phase on the continuous phase in the Euler-Lagrange approach. The exact expression of these terms is given in Chapter 5. In the RANS approach models need to be developed to estimate the Reynolds-stresses $\overline{u_i u_j}$ and enthalpy transport by turbulent fluctuations $\overline{u_i h}$. Several models exist with different degrees of complexity. We can cite the three most common models: the $k-\varepsilon$ model, the $k-\omega$ model and the Reynolds-stress model. We refer to Wilcox (1993) for an extensive description of these models. The $k-\varepsilon$ is the only turbulence model implemented in the FLACS model.

4.1.3 The $k-\varepsilon$ turbulence model

The $k-\varepsilon$ model is the model implemented in FLACS as well as in most of the commercial CFD codes. It has the broadest range of applicability: combustion, multiphase flows, atmospheric flows to cite a few of its domain of applications. Jones and Launder (1972) are credited with developing the standard $k-\varepsilon$ model. The $k-\varepsilon$ model is a turbulent viscosity model. According to the turbulent viscosity hypothesis the Reynolds stresses are given by:

$$\rho\overline{u_i u_j} = -\mu_t\left(\frac{\partial U_i}{\partial x_j}+\frac{\partial U_j}{\partial x_i}-\frac{2}{3}\frac{\partial U_k}{\partial x_k}\delta_{ij}\right)+\rho\frac{2}{3}k\delta_{ij} \tag{4.6}$$

The Einstein notation is used. The turbulent viscosity hypothesis is directly analogous to the relation for the viscous stresses in a Newtonian fluid (Pope, 2000). Two transport equations, one for k the turbulent kinetic energy and one for ε the turbulent dissipation rate, are solved and it is assumed that the turbulent viscosity μ_t is only dependent on k and ε. Thus from dimensional arguments:

$$\mu_t = C_\mu \rho \frac{k^2}{\varepsilon} \tag{4.7}$$

and $C_\mu = 0.09$ is one of the five model constants. The transport equations for k and ε write:

$$\begin{aligned}\frac{\partial}{\partial t}(\beta_v \rho k)+\frac{\partial}{\partial x_j}(\beta_j \rho u_j k) &= \frac{\partial}{\partial x_j}\left[\left(\beta_j\frac{\mu_{eff}}{\sigma_k}\right)\frac{\partial k}{\partial x_j}\right]\\ &\quad +\beta_v\wp+\beta_v\mathcal{G}-\beta_v\rho\varepsilon+S_{k_{p\to f}}\end{aligned} \tag{4.8}$$

$$\begin{aligned}\frac{\partial}{\partial t}(\beta_v \rho \varepsilon)+\frac{\partial}{\partial x_j}(\beta_j \rho u_j \varepsilon) &= \frac{\partial}{\partial x_j}\left[\left(\beta_j\frac{\mu_{eff}}{\sigma_\varepsilon}\right)\frac{\partial \varepsilon}{\partial x_j}\right]\\ &\quad +\beta_v\rho C_{\varepsilon_1}(\wp+\mathcal{G})\left(1+C_{\varepsilon_3}R_f\right)\frac{\varepsilon}{k}\\ &\quad -\beta_v\rho C_{\varepsilon_2}\frac{\varepsilon^2}{k}+S_{\varepsilon_{p\to f}}\end{aligned} \tag{4.9}$$

where $\wp$ is the production of turbulent kinetic energy by the flow shear stress and $\mathcal{G}$ is the production or destruction of turbulent kinetic energy due to buoyancy forces. The production of turbulent kinetic energy by the flow shear stress writes:

$$\wp = -\rho\overline{u_i u_j}\frac{\partial U_i}{\partial x_j} \tag{4.10}$$

The approach of Rodi and for Hydraulic Research (1993) is used to model buoyancy effects in the k and ε equations:

$$R_f = -\left(\frac{\mathcal{G}}{\wp + \mathcal{G}}\right)\frac{|\mathbf{u_n}|}{|\mathbf{u}|} \tag{4.11}$$

where $\mathbf{u_n}$ is the velocity vector normal to the gravity vector. The production or destruction of turbulent energy by buoyancy force writes:

$$\mathcal{G} = -\frac{1}{\rho}\left(\frac{\mu_t}{\sigma_b}\right) g_i \frac{\partial \rho}{\partial x_i} \tag{4.12}$$

In the FLACS model the effective viscosity $\mu_{eff} = \mu + \mu_t$ is used in the turbulent transport of scalars. The source terms $S_{k_{p\to f}}$ and $S_{\varepsilon_{p\to f}}$ represent the production or destruction of turbulent kinetic energy due to the presence of a dispersed phase. The mathematical expressions of these source terms is given in Chapter 5. The standard values of all the model constants are (Launder and Sharma, 1974):

$$C_\mu = 0.09 \quad C_{\varepsilon_1} = 1.44 \quad C_{\varepsilon_2} = 1.92 \quad C_{\varepsilon_3} = 0.8 \quad \sigma_k = 1.0 \quad \sigma_\varepsilon = 1.3 \quad \sigma_b = 0.8 \tag{4.13}$$

The performance of the standard $k-\varepsilon$ model is usually acceptable for simple flows (2D thin shear flows in which the mean streamlines curvature and mean pressure gradient are small) but it can be quite inaccurate for complex flows (impinging jets for example) in the sense that the mean flow patterns are qualitatively incorrect (Pope, 2000). The standard values for the model constants represent a compromise, even though they are often referred to as universal constants. For any particular flow it can be that the accuracy of the results are improved by adjusting the constants.

4.2 Theory of single-phase turbulent jet flows

4.2.1 Neutrally buoyant jet flows

The axisymmetric turbulent round jet is one of the most commonly studied free shear flow. The category of free shear flows also includes wakes and mixing layers. Figure 4.2 shows a sketch of a turbulent round jet. The round jet is represented in polar coordinates $[x, r, \theta]$ and the velocity components are denoted $[U, V, W]$ respectively. The velocity at the nozzle exit is noted U_j and the local centre-line velocity is U_c. The jet half radius denoted $r_{1/2}$ is determined by $U_{r_{1/2}} = \frac{1}{2}U_c$. In the streamwise x-direction, three different regions are identified. The first region is the near field region which contains the potential core. The near field region extents from the exit orifice until $x/D \sim 6$ and the flow characteristics are largely affected by those of the nozzle exit (Fellouah et al., 2009). The second region is the intermediate field region which goes until $x/D \sim 30$. The near field and intermediate field region contain the development portion of the jet. In the far field region, for $x/D > 30$, the jet is fully developed. The far field region is also referred to as the self-similar region. The concept of self-similarity will be defined below in this section. Another three regions are defined in the radial direction. The centre-line region is where the longitudinal velocity is at its maximum

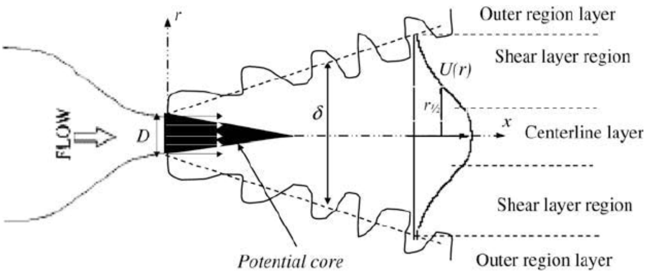

Figure 4.2: *Sketch of a turbulent round jet (taken from Fellouah et al. (2009)).*

and the outer region is where the velocity is 10 % of the local centre-line velocity. The shear layer region is located in between of these two regions and is characterized by strong velocity gradients in the radial direction.

Ball and Pollard (2007) provide a detailed review of theoretical and experimental works on turbulent round jets. The far field region of turbulent round jets is the region that has received most of the attention. One of the first experimental work was conducted by Wygnanski and Fiedler (1969) and consisted of extensive measurements of mean velocities, second and third order single point correlations, energy balances and length scales. Subsequently, many other studies have focused on the far field region of the round jet. We can cite the work of Panchapakesan and Lumley (1993a,b), Hussein et al. (1994) and Uddin and Pollard (2007). The main purpose of these studies was to examine the concept of universal self-similarity. Georges in his 1989 paper (George, 1989) gives the following definition of self-similarity: *"Self preservation (or similarity) is said to occur when the profiles of velocity (or any other quantity) can be brought into congruence by simple scale factors which depend on only one of the variables"*. In order to illustrate this concept, Figure 4.3 shows radial profiles of mean axial velocity, $U(x,r)$ (axisymmetric implies $U(x,r,\theta) = U(x,r)$), in the far field region of a turbulent round jet. All profiles have a similar shape. Following the concept of self-similarity we scale the axial velocity by $U_c(x)$ and the radial direction by $r_{1/2}(x)$. The scaled profiles are shown on Figure 4.3 and collapse perfectly on the same curve. A turbulent flow reaches self-preservation when dynamical equilibrium has been attained. All dynamical changes evolve together and no further dynamical adjustments are needed.

The self-similar solutions for the turbulent round jets are derived by first considering the Reynolds Averaged Navier-Stokes equations in their boundary layer form (George, 1989). For an axisymmetric turbulent round jet the turbulent boundary layer equations are:

$$\frac{\partial U}{\partial x} + \frac{1}{r}\frac{\partial rV}{\partial r} = 0 \tag{4.14}$$

$$U\frac{\partial U}{\partial x} + V\frac{\partial U}{\partial r} = -\frac{1}{r}\frac{\partial r\overline{uv}}{\partial r} \tag{4.15}$$

Equation (4.14) is the continuity equation and Equation (4.15) is the conservation equation of momentum in the longitudinal direction. Multiplying Equation (4.15) by r and using Equation (4.14) to write the convective terms in conservative forms we

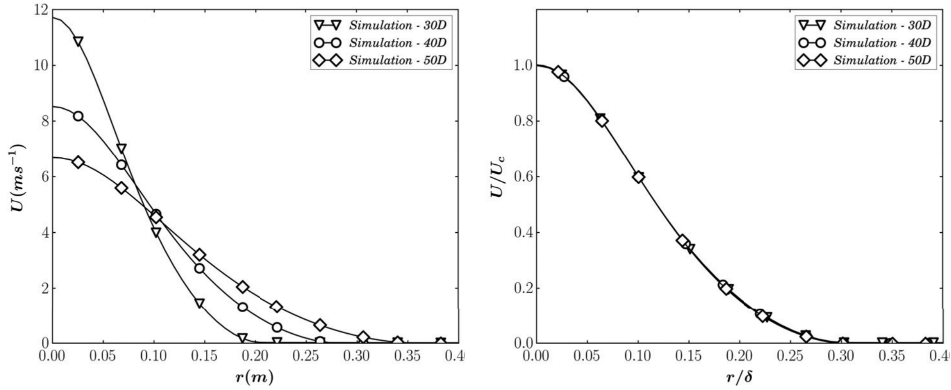

Figure 4.3: *Illustration of the concept of self-similarity: radial profiles of mean axial velocity of a turbulent round jet.*

obtain:

$$\frac{\partial}{\partial x}\left(rU^2\right)+\frac{\partial}{\partial r}\left(rUV+r\overline{uv}\right)=0 \tag{4.16}$$

By integrating Equation (4.16) from $r=0$ to $r=\infty$ and since the product of mean velocities UV goes to zero faster than $1/r$ we derive the longitudinal variation of the momentum integral:

$$\frac{\partial}{\partial x}\left(\int_0^\infty rU^2dr\right)=0 \tag{4.17}$$

The momentum integral is constant and independent of x and it is equal to the rate at which momentum is injected at the source. Following George (1989) the momentum injected at the source is denoted ρM_0 where M_0 is the kinematic momentum rate (also denominated specific momentum flux):

$$M_0=2\pi\int_0^\infty rU^2dr \tag{4.18}$$

We seek self-similar solutions of the following form:

$$\begin{aligned} U(x,r) &= U_c(x,M_0)f(\eta) && (4.19)\\ -\overline{uv}(x,r) &= R_c(x,M_0)g_{12}(\eta) && (4.20)\\ \eta &= \frac{r}{\delta(x)} && (4.21)\end{aligned}$$

The profile functions $f(\eta)$ and $g_{12}(\eta)$ account for all of the radial variation. If they are properly defined the profiles of mean velocities and Reynolds stresses should collapse into a single curve at every downstream locations (provided that the location is in the far field region). The functions $U_c(x,M_0)$, $R_c(x,M_0)$ and $\delta(x)$ incorporate the streamwise variations. The differentiation of $U(x,r)$ with respect to x now gives:

$$\begin{aligned}\frac{\partial U}{\partial x} &= \frac{\partial}{\partial x}(U_c(x,M_0)f(\eta)) \\ &= f(\eta)\frac{\mathrm{d}U_c}{\mathrm{d}x}+U_c\frac{\mathrm{d}f(\eta)}{\mathrm{d}x} \\ &= f(\eta)\frac{\mathrm{d}U_c}{\mathrm{d}x}-U_c f'\frac{\eta}{\delta}\frac{\mathrm{d}\delta}{\mathrm{d}x}\end{aligned} \tag{4.22}$$

Following the same procedure for the differentiations with respect to r and rewriting the conservation equation of momentum in the longitudinal direction yield:

$$\left[\frac{\delta}{U_c}\frac{\mathrm{d}U_c}{\mathrm{d}x}\right]f^2-\left(\left[\frac{\delta}{U_c}\frac{\mathrm{d}U_c}{\mathrm{d}x}\right]+2\left[\frac{\mathrm{d}\delta}{\mathrm{d}x}\right]\right)\frac{f'}{\eta}\int_0^{\eta}f\hat{\eta}\mathrm{d}\hat{\eta}=\left[\frac{R_c}{U_c^2}\right]\frac{(\eta g_{12})'}{\eta} \tag{4.23}$$

For self-similar solutions to exist all terms in brackets must have the same x dependence. The momentum integral writes:

$$M_0=\left[U_c^2\delta^2\right]2\pi\int_0^{\infty}f^2\eta\mathrm{d}\eta \tag{4.24}$$

It follows that in order to have the same x dependence all terms in brackets in Equation (4.23) must be constant which implies that $\delta\sim x$, $U_c\sim x^m$ and $R_c\sim x^{2m}$. For now the exponent m is unknown. The momentum integral written in self-similar variables, Equation (4.24), requires $U_c^2\delta^2=cte$. Therefore, $m=-1$ and $U_c\sim x^{-1}$. The final form of the self-similar solutions is:

$$U(x,r) = \frac{BM_0^{1/2}}{x}f(\eta) \tag{4.25}$$

$$-\overline{uv}(x,r) = \frac{B^2M_0}{x^2}g_{12}(\eta) \tag{4.26}$$

$$\eta = \frac{r}{\delta(x)} \tag{4.27}$$

$$\delta(x) = x \tag{4.28}$$

The self-similar solutions have been extensively tested against experimental data. Some authors have found that the self-similar region had minimal dependence on initial conditions justifying the assumption $U_c=U_c(x,M_0)$ (Dowling and Dimotakis, 1990). On the other hand some authors think that the self-similar region is not universal and is dependent on initial conditions. George (1989) shows that if one assumes $U_c=U_c(x,M_0,m_0)$ where m_0 is the rate at which mass is added to the flow, jets can spread at any power of x, i.e. the power of x (noted m previously) is undefined. Boersma et al. (1998) support this assumption because they found that different nozzle outlet conditions were affecting the mean and fluctuating velocities. Mi et al. (2001) have also reported observations which confirm the influence of initial conditions on the self-similar region.

4.2.2 Variable density jet flows

The influence of density variations on flow properties of turbulent round jets is now investigated. The configuration of interest concerns the release of a fluid having a density ρ_j at the exit orifice into an ambient fluid having a density $\rho_\infty \neq \rho_0$. Turbulent flows with variable density can be obtained from temperature variations or from mixture composition by mixing components with different molecular weight. The main objective of this section is to get some insights in the effects of density variations on turbulence mixing in jets. The question of whether jets of variable density exhibit a self similar behaviour will also be investigated.

In addition to the specific momentum flux M_0 with units $^{m^4}/_{s^2}$ the specific buoyancy flux B_0 is another important parameter which characterizes variable density turbulent jets. The specific buoyancy flux has units $^{m^4}/_{s^3}$. A length scale which defines the relative effect of momentum and buoyancy is written as (Papanicolaou and List, 1988):

$$l_s = \frac{M_0^{3/4}}{B_0^{1/2}} \tag{4.29}$$

Momentum is significant close to the exit orifice where $x/l_s \ll 1$ and buoyancy does not become significant until the distance from the source is much larger than the length scale l_s, i.e. $x/l_s \gg 1$. The specific momentum and buoyancy fluxes are written as:

$$M_0 = \left(\frac{\pi}{4}\right)^{1/4} D^2 U_0^2 \tag{4.30}$$

$$B_0 = \left(\frac{\pi}{4}\right)^{1/4} D^2 U_0 \left(\frac{\rho_\infty - \rho_0}{\rho_0}\right) g \tag{4.31}$$

Equation (4.29) can be rewritten as:

$$l_s = \left(\frac{\pi}{4}\right)^{\frac{1}{4}} DFr \tag{4.32}$$

where Fr is the Froude number:

$$Fr = \frac{U_0}{\left(\frac{|\rho_\infty - \rho_0|}{\rho_0} Dg\right)^{1/2}} \tag{4.33}$$

Papanicolaou and List (1988) conducted measurements of axial and radial velocity components and concentration in a turbulent buoyant jet and found that for $x/l_s < 1$ the flow was behaving like a momentum jet and that for $x/l_s > 5$ the flow was behaving like a plume. Chen and Rodi (1980) use a slightly different expression for the length scale l_s and they predict a shorter momentum dominated region.

Provided that the momentum region extents beyond $x/D \sim 30$ the self-similar profiles derived previously (see Equations 4.25, 4.26, 4.27 and 4.28) can be used for the mean velocities and turbulent properties. Self-similar profiles for the concentration can also be derived by following the same approach. Indeed, the conservation equation for concentration C is similar to the conservation equation of momentum (Equation 4.15):

$$U\frac{\partial C}{\partial x} + V\frac{\partial C}{\partial r} = -\frac{1}{r}\frac{\partial r\overline{vc}}{\partial r} \tag{4.34}$$

Thus, the self-similar solution for the concentration has the following form (Chen and Rodi, 1980):

$$C(x,r) = B_c \frac{C_0 r_\varepsilon}{x} h(\eta) \tag{4.35}$$

where B_c is the rate of the centre-line decay for the concentration. The effective radius r_ε is defined to be:

$$r_\varepsilon = \frac{m_0}{(\pi \rho_\infty M_0)^{\frac{1}{2}}} \tag{4.36}$$

From a physical point of view the effective radius represents the radius of a hypothetical jet with density ρ_∞ and the same mass flux m_0 and momentum flux M_0 than the jet under consideration (Richards and Pitts, 1993).

In the buoyancy dominated region it is not clear whereas self-similar profiles can be derived or not. From basic dimensional analysis the centre-line axial velocity varies like $x^{-\frac{1}{3}}$ and the centre-line concentration varies like $x^{-\frac{5}{3}}$. The experimental data of Papanicolaou and List (1988) follows these trends.

4.3 Simulations of free round jets with the FLACS model

In this section we want to investigate the performance of the FLACS model in simulating turbulent round jets of both neutral and variable densities.

4.3.1 Neutrally buoyant jet flows

Previous numerical studies of turbulent round jets have shown that the $k-\varepsilon$ model over-predicts the decay rate and spreading rate of the jet (Pope, 1978). Different methods exist to prevent this over-prediction. One group of methods consist in modifying the constants C_μ, C_{ε_1} and C_{ε_2}. The constants are functions of the decay rate and spreading rate. For example, McGuirk and Rodi (1979) suggests the following modification to the constant C_{ε_1}:

$$C_{\varepsilon_1} = 1.14 - 5.31 \frac{r_{1/2}}{U_c} \frac{\mathrm{d}U_c}{\mathrm{d}x} \tag{4.37}$$

Launder et al. (1972); Morse (1977) have proposed similar expressions. Pope (1978) has derived a more elaborate fix to this problem. An extra term, ψ, is added to the dissipation equation and accounts for the non-dimensional stretching of vortices which reduces the turbulent viscosity. The objective here is not to implement and test these modifications because we want to be able to simulate in the same run different types of turbulent flows: jet flows, atmospheric turbulent flows, bluff body flows and multiphase flows. Therefore, we want to keep the $k-\varepsilon$ model as "universal" as possible. We now assess the performances of the FLACS model (with the standard $k-\varepsilon$ model) in simulating turbulent jet flows.

A neutrally buoyant turbulent round jet is first considered and the concepts of self-similarity discussed in the previous section are used to present the results. The jet Reynolds number is $Re = 9.5510^4$ based on the jet exit velocity U_j; the same jet Reynolds number as in the experiment of Hussein et al. (1994). The inflow velocity profile is modelled as a top-hat profile, i.e. the flow inside the nozzle is not simulated

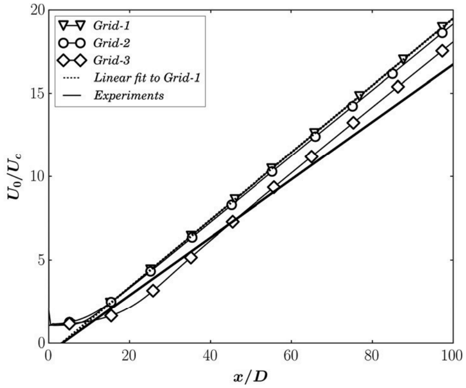

Figure 4.4: *Grid sensitivity for a turbulent round jet. The axial profiles of mean axial velocity are shown.*

with the FLACS model. First, a grid sensitivity study is performed to assess the influence of grid resolution on the flow parameters. Three grids are considered, Grid-1 has 4.10^6 cells and a resolution of 8 mm close to the exit orifice; Grid-2 has 2.10^6 cells and a resolution of 13 mm close to the exit orifice; and Grid-3 has 9.10^5 cells and a resolution of 26 mm close to the exit orifice. The exit orifice has a diameter of $D = 25.4$ mm. Figure 4.4 shows the results of the grid sensitivity study. By decreasing the grid resolution we show that the results converge, i.e. Grid-2 gives almost the same results than Grid-1. On Figure 4.4 we note that after a short establishment zone the centre-line mean velocity decays as $1/x$ in accordance with Equation (4.25) which implies:

$$U_c(x) = \frac{B' M_0^{1/2}}{x} \tag{4.38}$$

and writing the kinematic momentum rate M_0 at the jet exit as:

$$M_0 = \frac{1}{4}\pi U_0^2 D^2 \tag{4.39}$$

we obtain:

$$\frac{U_0}{U_c(x)} = \frac{1}{B'}\left(\frac{x}{D}\right) = \frac{1}{B}\left(\frac{x}{D} - \frac{x_0}{D}\right) \tag{4.40}$$

where B is the decay constant and x_0 is the virtual origin. The linear fit on Figure 4.4 gives $B = 4.96$ and $x_0/D = 3.26$. Fellouah et al. (2009) report experimental values for B and x_0. The mean of all reported experimental values gives $B = 5.772$ and $x_0/D = 3.38$. As expected the FLACS model with the standard $k - \varepsilon$ model over-estimates the decay rate of the jet but does a relatively good job in predicting the position of the virtual origin. The radial profiles of mean axial and mean radial velocities are now inspected via the self-similarity theory. Self-similarity implies:

$$\frac{U(x,r)}{U_c(x)} = f\left(\frac{r}{x - x_0}\right) \tag{4.41}$$

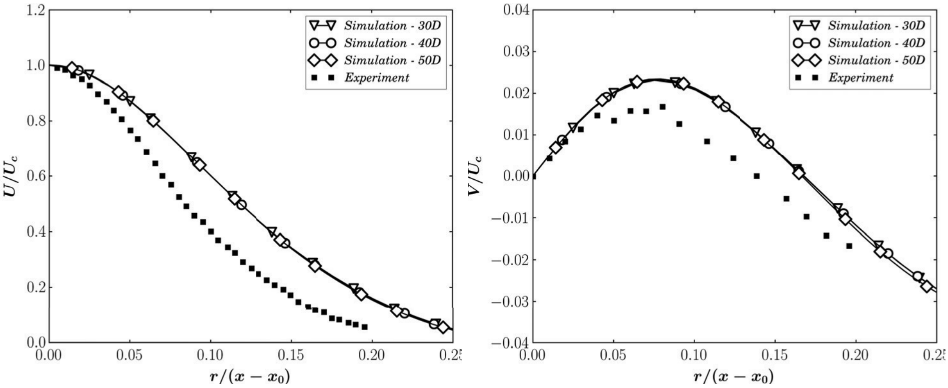

Figure 4.5: *Radial profiles of mean axial and mean radial velocities.*

The radial profiles of mean axial and mean radial velocities are presented on Figure 4.5. The experimental data are from citethussein1994]. Different axial positions are considered in order to illustrate the self-similarity concept. All axial positions lay in the far field region of the jet where self-similarity should prevail ($x/D > 30$). The spread of the round jet is slightly over-estimated in the simulation as expected. This is a known feature of the $k-\varepsilon$ model and several authors have proposed different methods to fix it as we have already discussed. The profiles at different x locations collapse on the same curve validating the application of the self-similarity theory to the mean velocities. As far as the turbulent quantities are concerned, the turbulent kinetic energy can be scaled in two ways. Either the square of the centre-line mean velocity is used or the centre-line turbulent kinetic energy is used. Figure 4.6 shows both options. The experimental data in Hussein et al. (1994) were reported as scaled values by the square of the centre-line mean velocity. The turbulent kinetic energy is over-estimated in the simulation which is coherent with the observations made on the mean velocities profiles. Indeed, an increase of turbulent kinetic energy would lead to an increase in the turbulent diffusion of momentum and consequently a larger spreading rate of the jet. When scaled by the square of the mean centre-line velocity the curves do not collapse at different x locations as they were collapsing for the mean velocities. However, when scaled by the centre-line turbulent kinetic energy the curves do collapse showing the sensibility to the scale factors.

4.3.2 Variable density jet flows

Numerical simulations of variable density jets are rather scarce. The LES simulations of Foysi et al. (2010) and Wang et al. (2008) provide detailed investigations of variable density jets. Foysi et al. (2010) considered plane and round jets of varying density ratios $s = \rho_j/\rho_\infty$ and discussed the similarity theory. For the round jets they found that scaling x and U_c by $s^{-1/4}$ as recommended by Chen and Rodi (1980) was collapsing the data. Wang et al. (2008) used LES and simulated the round jet experiments of Amielh et al. (1996) and Djeridane et al. (1996). The experiments consisted in confined round jets of air, helium and CO_2 exiting into a low speed air co-flow. Wang et al. (2008)

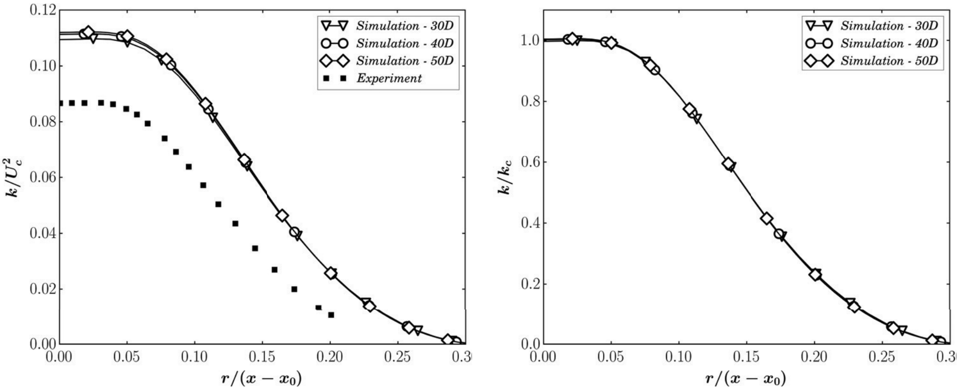

Figure 4.6: *Radial profiles of turbulent kinetic energy.*

reported excellent agreement between the experiments and the simulations.

The experiments of Amielh et al. (1996) and Djeridane et al. (1996) are simulated with the FLACS model. As in the work of Wang et al. (2008) three round jets of air, helium and CO_2 issuing into a low speed air co-flow are investigated. The density ratio ranges from 0.14 for the helium jet to 1.52 for the CO_2 jet. In the experiments the jets were discharging from a long pipe of diameter 26 mm into an air co-flow confined by an outer pipe. The diameter of the outer pipe was eleven times larger than the diameter of the discharging pipe and thus we can assume that the confinement is weak. The flow inside the discharging pipe is not modelled and a top-hat velocity profile (point source of momentum) is used in the simulations. The co-flow velocity was $U_{cf} = 0.9\,\mathrm{m/s}$. It is worth noting that the momentum flux is the same for all three jets $M_0 = 0.1\,\mathrm{N}$. The results are compared in the momentum controlled region of the jet (by opposition to the buoyancy controlled region) and thus it is important that all jets have the same momentum flux. From Equation (4.32) we obtain $l_s = 0.65\,\mathrm{m}$ for the helium jet and $l_s = 0.87\,\mathrm{m}$ for the CO_2 jet. Following Papanicolaou and List (1988) the jets behave like pure momentum jets for $x/l_s < 1$ which means that the helium jet is a pure momentum jet from the pipe exit down to $25D$ and the CO_2 jet is a pure momentum jet down to $33D$. The comparison between simulations and experiments is made down to $35-40D$. The whole momentum region is covered as well as a small part of the intermediate region (the pure buoyant region starts at $5l_s$). No grid sensitivity is reported for the variable density jets since it was already done for the neutrally buoyant jets (the exit diameters are almost equal and Grid-1 is used in these computations).

A comparison of the axial mean velocity and mean concentration is shown on Figure 4.7. For the velocity profiles the agreement is almost perfect but some disagreement is noted for the CO_2 concentration profile. The concentration profile of the helium jet is well predicted. The dilution rate of the CO_2 concentration is over-estimated in the simulation. The transport equation for the mass fraction of any given substance writes:

$$\frac{\partial}{\partial t}(\beta_v \rho Y) + \frac{\partial}{\partial x_j}(\beta_j \rho U_j Y) = \frac{\partial}{\partial x_j}\left(\beta_j \frac{\mu_{eff}}{\sigma_Y}\frac{\partial Y}{\partial x_j}\right) \tag{4.42}$$

where σ_Y is the turbulent Schmidt number associated with the mass fraction of the

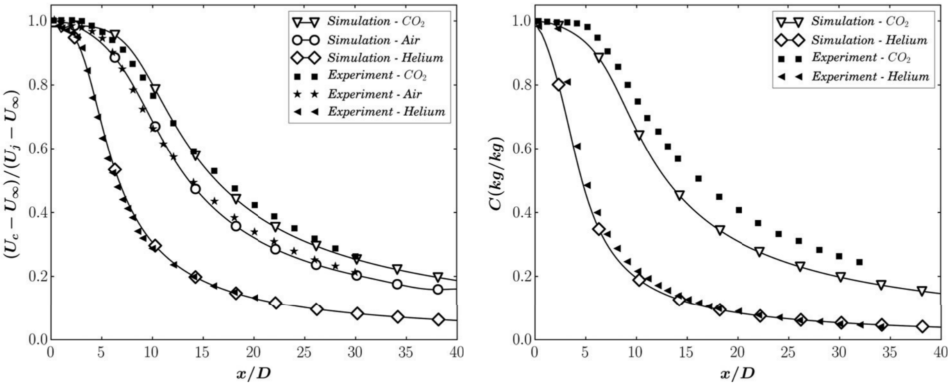

Figure 4.7: *Axial profiles of mean axial velocities and concentrations. Comparison between numerical predictions and the data of Amielh et al. (1996) and Djeridane et al. (1996).*

substance. In the FLACS model a value of $\sigma_Y = 0.7$ is used as recommended by Chen and Rodi (1980). Instead, the turbulent Schmidt number might be a function of the density ratio. The value $\sigma_Y = 0.7$ seems to give good results for the helium jet but it appears to be too low for the CO_2 jet. The influence of density on the axial decay of velocity and axial dilution of concentration is clear. The helium jet decays and is diluted much faster than the air jet and CO_2 jet. Since the three jets have the same momentum flux, it can be inferred that the differences in the decay and dilution rates are due to a more efficient turbulent mixing for low density jets.

Turning to the radial profiles a good agreement between experiment and simulation is seen for the velocity profiles (Figure 4.8). The radial profiles of CO_2 concentration match the experimental data close to the orifice. Away from the orifice, for example at $15D$, large discrepancies are noted. The dilution of CO_2 by turbulent mixing is too large resulting in an almost flat radial profile compared to the experimental data. For the helium jet close to the orifice ($x/D < 5$) and on the centre-line axis, the concentration is under-estimated in the simulation. This might be due to the top-hat initial condition for the leak. Compared to the CO_2 jet the helium jet is more sensitive to the initial conditions.

4.4 Conclusions

The FLACS solver was presented. Turbulence modelling was briefly discussed and the RANS equations solved in the FLACS model were given. The $k - \varepsilon$ turbulence model of Jones and Launder (1972) with the universal set of constants proposed by Launder and Sharma (1974) is implemented in the FLACS model. The self-similarity theory of turbulent round jets as presented by George (1989) was discussed and the performance of the FLACS model in simulating single-phase high Reynolds number round jets was investigated. The predictions of the FLACS model were compared with the experiments of Hussein et al. (1994). As expected the FLACS model with the universal set of constants for the $k - \varepsilon$ turbulence model over-estimates the decay rate

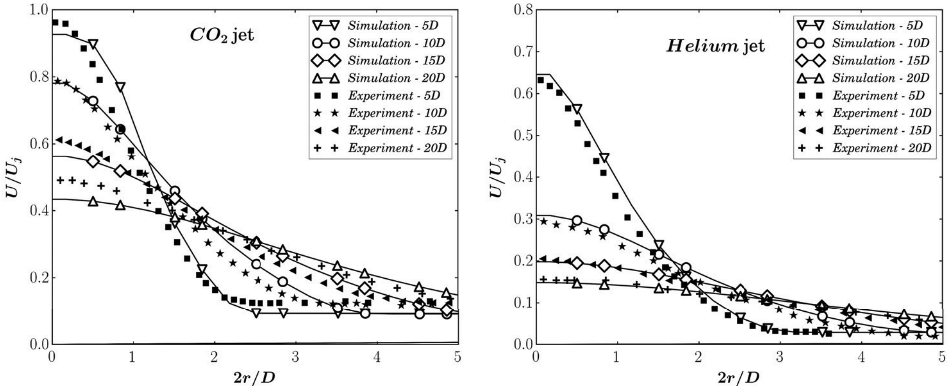

Figure 4.8: *Radial profiles of mean axial velocities for the CO_2 and Helium jets. Comparison between numerical predictions and the data of Amielh et al. (1996) and Djeridane et al. (1996).*

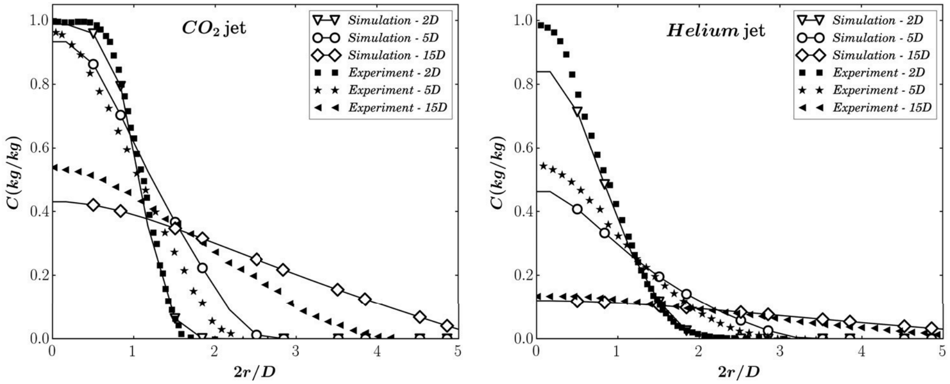

Figure 4.9: *Radial profiles of CO_2 and Helium concentrations. Comparison between numerical predictions and the data of Amielh et al. (1996) and Djeridane et al. (1996).*

of the air turbulent round jet by 14 %. The radial profiles of mean axial velocity are shown to be self-similar. The variable density jets experiments of Amielh et al. (1996) and Djeridane et al. (1996) were simulated. The results obtained are in good agreement with experimental data. Helium being lighter than CO_2, the mean axial velocity and concentration of the helium jet decay faster than the mean axial velocity and concentration of the CO_2 jet. Buoyant jets dilute faster in the surrounding atmosphere compared to dense jets. The FLACS model was shown to give acceptable predictions for the mean fields of single phase variable density jets. The next chapter of the thesis deals with the implementation of two-phase flow models into the FLACS code in order to be able to simulate high momentum two-phase jets.

Chapter 5

Two-phase turbulent jet flows: the Euler-Lagrange approach

5.1 Classification of models

The different classes of models employed to perform CFD simulations of multiphase flows are first introduced. The particle phase refers to the liquid droplets whereas the continuous phase refers to the gas phase (the term "fluid" is also used, for example in the expression particle-fluid interactions). Multiphase flows can be said to be either dense or dispersed. The flow is said to be dispersed if particle-fluid interactions control the transport of the particle phase. In dispersed flows particle-particle interactions are neglected and thus collisions, coalescence or particle-particle fluid dynamic interactions are not taken into account (Crowe, 2006). When particle-particle interactions dominate the flow is said to be dense. Figure 5.1 illustrates the concepts of dispersed and dense flows and their dependence on the mass or volume fraction of the particle phase. For dispersed flows several levels of coupling exist between the particle phase and the continuous phase. One-way coupling always exists because the particle phase is always affected by the continuous phase. As the volume or mass fraction of the particle phase increases it might be necessary to model two-way, three-way or four-way coupling effects. Two-way coupling exists when the particle phase modifies the properties of the continuous phase. Modulation of the gas phase turbulence is an example of two-way coupling effects. The particles, depending on their size and mass loading, can either enhance or dampen the level of fluid turbulence. For very low particle volume fraction the term dilute flows is used and in such a case one-way and two-way coupling are preponderant, three-way and four-way coupling can be neglected. In this work the volume fraction of the particle phase is of order 10^{-3} and following Elghobashi (1994) the flow is assumed to be dilute.

The continuous phase is usually solved in the Eulerian reference frame. For the particle phase both Eulerian and Lagrangian reference frames are commonly used. In the Euler-Lagrange class of models the continuous phase is solved in the Eulerian reference frame and the particle phase is solved in the Lagrangian reference frame. In the Euler-Euler class of models both the continuous and particle phases are solved in the Eulerian reference frame. The Euler-Euler approach is best suited to model dense multiphase flows. Indeed, in the Euler-Euler approach conservation equations for the particle phase are derived by assuming that the particle phase can be viewed

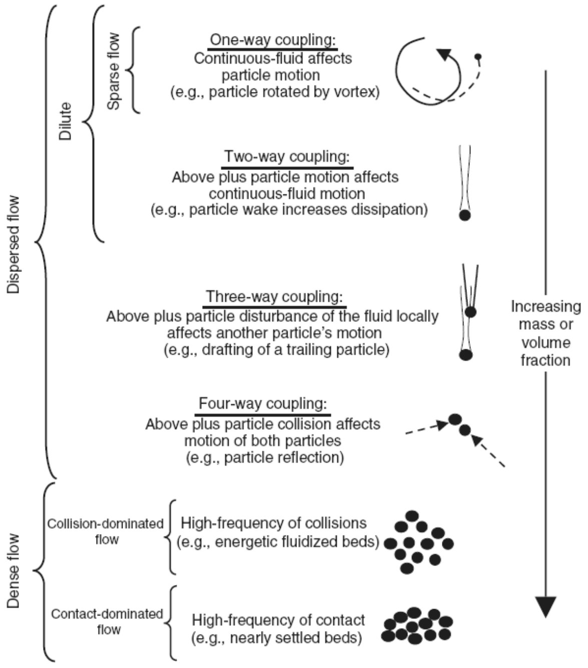

Figure 5.1: *Illustration of the different class of models (taken from (Crowe, 2006)).*

as a continuum. Phenomena like jet break-up or coalescence are well reproduced with an Eulerian treatment of the dispersed phase. DNS methods have been employed to simulated such processes. The continuous and dispersed phases are treated as a single fluid with a jump in the fluid properties at the position of the interface (Scardovelli and Zaleski, 1999; Tryggvason et al., 2001). For engineering flows the two-fluid or multi-fluid models are employed (Crowe, 2006). In these models Euler equations for the dispersed phase are either obtained by volume averaging or by ensemble averaging and inter-phase terms and Reynolds stress like terms have to be modelled in order to close the set of equations. Several closure methods exist, a recent closure approach is the probability density function approach of Simonin et al. (1993). The Euler-Euler approach can handle an infinite number of particles and this constitutes its main strength. However, the modelling of different particle sizes is rather tedious as it requires the creation of a particle phase for each particle size. On the other hand, poly-dispersed and dilute flows are often treated with an Euler-Lagrange approach. Several degrees of complexity exist in the Lagrange description of the dispersed phase. In the so-called immersed boundary method or resolved volume method the particles are larger that the grid cell size and the forces acting on the particles are solved over the particle surface. As the particle size becomes several order of magnitude smaller than the grid cell size the point particle method can be employed (Loth, 2000). In the point particle method particle averaged expressions for the forces acting on the particle need to be derived. The point particle approach is the method that is used in this work to compute the properties of the dispersed phase.

5.2 Particle phase equations

When dealing with poly-dispersed turbulent two-phase flows the Lagrange reference frame appears to be the natural frame for treating the particle phase. Indeed, in the Lagrangian approach individual particles, or representative particles, are tracked and their characteristics are evaluated as they move throughout the turbulent flow field. Moreover, this approach is well adapted for modelling particle interactions with obstacles and particle settling (Crowe, 2006) which are some of the processes that need to be accounted for in this work. We consider non-compressible, non-reacting fluid particle flows without collisions between particles. The physical phenomena of interest are particles dispersion, particles vaporization, particles deposition and coupling between the continuous phase and particle phase. The restrictions imposed on the types of phenomenon modelled must not be seen as limitations of the Euler-Lagrange method but rather as a choice due to the final industrial application of this work. The Euler-Lagrange formalism is well suited for the extension to more complex physics such as combustion. Gouesbet and Berlemont (1998); Loth (2000); Mashayek and Pandya (2003) give comprehensive reviews of the particle phase equations.

5.2.1 The particle momentum equation and its simplification

The trajectory of an individual particle is obtained by solving the following set of differential equations:

$$\frac{\mathrm{d}\mathbf{x}_p}{\mathrm{d}t} = \mathbf{U}_p \tag{5.1}$$

$$m_p \frac{\mathrm{d}\mathbf{U}_p}{\mathrm{d}t} = \sum \mathbf{F}_{\to p} \tag{5.2}$$

The mathematical expressions of the forces acting over a particle have been subject to some controversy in the literature (Gouesbet and Berlemont, 1998). Basset (1984); Boussinesq (1903); Oseen (1927) first derived the momentum equation for a spherical particle moving through a stagnant fluid. This equation is often referred to as the BBO equation. Several authors extended the BBO equation to cases where the fluid is no longer at rest: Buevich (1966); Corrsin and Lumley (1956); Tchen (1947) to name a few but not all. However, their attempts in proposing a general equation for the particle momentum were not successful. The equation proposed by Maxey and Riley (1983) is accepted today as the correct equation for the momentum of a single spherical particle moving in a turbulent flow field and writes:

$$\begin{aligned} m_p \frac{\mathrm{d}\mathbf{U}_p}{\mathrm{d}t} = & \frac{\pi d_p^3}{6} \rho_f \frac{D\mathbf{U}_s}{Dt} + \frac{\pi d_p^3}{6} \left(\rho_p - \rho_f\right) \mathbf{g} \\ & + \frac{\pi d_p^2}{8} \rho_f C_D |\mathbf{U}_s - \mathbf{U}_p| \left(\mathbf{U}_s - \mathbf{U}_p\right) \\ & + \frac{\pi d_p^3}{12} \rho_f \left(\frac{D\mathbf{U}_s}{Dt} - \frac{\mathrm{d}\mathbf{U}_p}{\mathrm{d}t} \right) \\ & + \frac{3}{2} d_p^2 \rho_f \sqrt{\pi \nu_f} \int_{-\infty}^{t} \frac{\mathrm{d}}{\mathrm{d}\tau} \left(\mathbf{U}_s - \mathbf{U}_p\right) \frac{\mathrm{d}\tau}{\sqrt{t-\tau}} \end{aligned} \tag{5.3}$$

The terms on the right hand side of 5.3 represent the pressure-gradient force, the buoyancy force, the drag force, the added mass force and the Basset history force.

Armenio and Fiorotto (2001) conducted an analysis of the importance of the different forces that act on a particle in a turbulent flow field. A wide range of particle-fluid density ratios has been studied from $\rho_p/\rho_f \sim 1$ to $\rho_p/\rho_f \sim 1000$. Compared to the drag force, the added mass force is always negligible. For a density ratio of order 1 the pressure-gradient force is relevant but its influence dramatically decreases for larger density ratio. Lastly, the Basset history force is also found to be negligible, being one order of magnitude smaller than the drag force over the range of density ratios tested. The density ratio of interest in our work is of order 10^2 or higher therefore the equation of motion of a particle simplifies to:

$$\frac{\mathrm{d}\mathbf{U}_p}{\mathrm{d}t} = \frac{1}{\tau_p}\left(\mathbf{U}_s - \mathbf{U}_p\right) + \mathbf{g} \tag{5.4}$$

In 5.4 τ_p is the particle relaxation time and it is expressed as:

$$\tau_p = \frac{\rho_p}{\rho_f}\frac{4d_p}{3C_D|\mathbf{U}_s - \mathbf{U}_p|} \tag{5.5}$$

In order to have a physical interpretation of the particle relaxation time we need to define a representative time-scale for the turbulent flow field. Let's define a macroscopic time-scale (by opposition to the Kolmogorov time-scale) for the mean flow field as:

$$\tau_f = \frac{L_f}{U_f} \tag{5.6}$$

where L_f is a macroscopic characteristic length-scale of the flow and U_f is a characteristic mean velocity scale. Variations of the fluid velocity occur over the time τ_f. Therefore, particles with a larger τ_p, i.e. $\tau_p \gg \tau_f$, are not able to respond to changes in the mean fluid velocity field whereas particles with a small τ_p, i.e. $\tau_p \ll \tau_f$, respond quasi-immediately to changes in the mean fluid velocity field. In the limit $\tau_p \to 0$ particles are defined as fluid particles or tracer particles. The effect of the relaxation time on the turbulent dispersion of the particles will be discussed further in the following sections. In 5.5 and 5.3 C_D is the drag coefficient which is a non-linear function of the particle Reynolds number:

$$Re_p = \frac{d_p|\mathbf{U}_s - \mathbf{U}_p|}{\nu_f} \tag{5.7}$$

Several expressions for C_D exist in the literature and they are discussed in length in Clift et al. (2005). The drag coefficient is expressed as a function of the particle Reynolds number via the Schiller-Naumann correlation which is the most commonly used correlation in the literature:

$$C_D = \begin{cases} \frac{24}{Re_p}\left(1 + 0.15Re_p^{0.687}\right) & \text{if } Re_p \leq 1000, \\ \\ 0.44 & \text{if } Re_p > 1000. \end{cases} \tag{5.8}$$

The only remaining unknown in (5.4) is the variable $\mathbf{U}_s = \mathbf{U}_s(t, \mathbf{x}_p(t))$ which is the instantaneous fluid velocity seen by the particle. One of the key issue in computing the particle motion in a turbulent flow field resides in estimating the seen instantaneous fluid velocity $\mathbf{U}_s$. The first reason is that only first and second velocity moments are available from the RANS computations of the continuous, gas, phase. Moreover, on a more general view, instantaneous fluid velocities of the continuous phase for high Reynolds number flows of practical interest are not yet available even with the method of Direct Numerical Simulation (DNS) which is still limited to low Reynolds flows (need a reference). The second reason is that we are dealing with heavy particles. Ichard and Melheim (2010) (see Annex A) have investigated the dispersion of heavy particles in isotropic turbulent flows. The dispersion of heavy particles in turbulent flows is greatly affected by the particle inertia (via τ_p) and by the crossing trajectory effect which is due to the gravity force acting on the particle. In Ichard and Melheim (2010), the inertia and crossing trajectory effects were shown to have an impact on the seen instantaneous fluid velocity. Therefore, a model that accounts for these effects needs to be employed to obtain $\mathbf{U}_s$

Two main approaches to estimating the seen instantaneous fluid velocity have been developed and used during the last three decades. The first class of models is referred to as random walk models (MacInnes and Bracco, 1992). The instantaneous velocity is approximated as the sum of the local mean fluid velocity extracted from the continuous phase computations and a random fluctuating velocity. The fluctuating velocity is sampled from a Gaussian distribution having a zero mean and a variance related to the turbulent velocity scale obtained from the solution of the mean fluid equations. However, models belonging to this class are subject to spurious effects when used in non-homogeneous turbulent flow field (Oesterlé, 2009). In the second class of models Stochastic Differential Equations (SDE) are solved to obtain the seen instantaneous velocity. The model implemented in our work is issued from this second class of models.

5.2.2 Background on Stochastic Differential Equations

Before discussing the physical modelling of the seen instantaneous velocity it is worth introducing and defining mathematical concepts and tools related to stochastic calculus. It will help in interpreting the significance of the model and identifying its strong and weak points. SDE are often introduced from the historical example of Brownian motion as they first appeared as a model for the erratic motion of a grain of pollen on a water surface, i.e. the Brownian motion. Following the work of Einstein (1905) on Brownian motion, Langevin (1908) tried to formulate the dynamics of such motions in terms of differential equations. They proposed an equation written as:

$$\frac{\mathrm{d}X_t}{\mathrm{d}t} = a\,(t, X_t) + b\,(t, X_t)\,\xi_t \tag{5.9}$$

The velocity of the small particles is expressed as the sum of a drift, deterministic, term $a\,(t, X_t)$ and a noisy, highly fluctuating, diffusive term $b\,(t, X_t)\,\xi_t$ where ξ_t is a random Gaussian variable for each time t and $b\,(t, X_t)$ is a space dependent intensity factor.

The random Gaussian variable ξ_t is also known as white noise. It has an infinite variance and thus it cannot be defined directly which means that equation 5.9 has no mathematical sense. However, a way around this difficulty is to write the following integral:

$$W(t) = \int_0^t \xi(t')\mathrm{d}t' \Leftrightarrow \mathrm{d}W_t = \xi_t \mathrm{d}t \tag{5.10}$$

It can be shown that W_t is the Wiener process which is a continuous Gaussian Markov process with the properties (Gardiner, 1985):

- a mean $\langle W_t \rangle = 0$
- a covariance $\langle (W_t - \langle W_t \rangle)(W_{t'} - \langle W_{t'} \rangle) \rangle = min(t,t')$
- trajectories are continuous but nowhere differentiable
- the increments of W_t, $\mathrm{d}W_t = W_{t+\mathrm{d}t} - W_t$ over small time-steps are stationary and independent. Each increment is a Gaussian variable with mean $\langle \mathrm{d}W_t \rangle = 0$ and variance $\langle (\mathrm{d}W_t)^2 \rangle = \mathrm{d}t$
- the trajectories are of infinite variation in every finite time interval which implies the need for the definition of a stochastic integral

Most of these properties, of fundamental importance for the physical modeling, cannot be properly understood without defining some mathematical stochastic tools. As it has been mentioned previously, the Wiener process is a Gaussian Markov process. A Markov process is a special kind of stochastic process. Stochastic processes are defined based on the concept of stochastic variables.

The first mathematical tool to be defined is the stochastic variable. The terms random and stochastic are equivalent. In order to be in line with the example of Brownian motion one may consider the set $A(pollen)$ of events. We can define the notation:

$$\omega(d_1) \in A \tag{5.11}$$

to indicate that the event $\omega(d_1)$ that a particle is a grain of pollen with diameter d_1 is one of the event contained in A. A random variable is some function G of ω denoted $G(\omega)$. The values taken by $G(\omega)$ usually belongs in physics to the space of real numbers $\Re$. In applied physics random variables are often defined via their probability density functions. The probability that the random variable G takes a value between x and $x + \mathrm{d}x$ with $x, \mathrm{d}x \in \Re$, is:

$$P(x < G(\omega) < x + \mathrm{d}x) = p(x)\mathrm{d}x \tag{5.12}$$

where $p(x)$ is the probability density function associated with the stochastic variable G. Moments of different orders are computed via the probability density function. For example the mean is obtained by:

$$\langle G(\omega) \rangle = \int_{-\infty}^{\infty} G(\omega)p(x)\mathrm{d}x \tag{5.13}$$

A stochastic process is a family of stochastic variables indexed by a parameter which in the field of applied physics is usually the time t. Stochastic processes are denoted $G(\omega,t)$ or even G_t. A stochastic process is defined by its N points probability density function:

$$p(t_1,x_1;t_2,x_2;...;t_n,x_n) \quad t_n > t_{n-1} > ... > t_2 > t_1 \tag{5.14}$$

at N different times. This probability density function describes completely the system of interest but its manipulation is becoming very complex as the value N increases. One can simplify this problem assuming that it is sufficient to know the present to predict the future. This assumption leads to Markov processes and it is expressed via the tool of conditional probabilities:

$$p(t_{n+1},x_{n+1}|t_1,x_1;t_2,x_2;...;t_n,x_n) = p(t_{n+1},x_{n+1}|t_n,x_n) \tag{5.15}$$

and

$$p(t_{n+1},x_{n+1}|t_n,x_n) = \frac{p(t_{n+1},x_{n+1};t_n,x_n)}{p(t_n,x_n)} \tag{5.16}$$

The Chapman-Kolmogorov formula is derived from the Markov propery and it writes (Gardiner, 1985):

$$p(t,x|t_0,x_0) = \int_{-\infty}^{+\infty} p(t,x|t_1,x_1)p(t_1,x_1|t_0,x_0)\mathrm{d}x_1 \tag{5.17}$$

This relation says that the probability to go from the initial state (t_0,x_0) to a given state (t,x) at any time t is given by the sum over all intermediate states (x_1,t_1). We have seen that the Langevin equation for Brownian motion could be expressed as a function of the Wiener process which is a Markov process. It then implies that the future state of the particles is only dependent on their present state. From 5.10 the Langevin equation can be re-written in the following form:

$$\mathrm{d}X_t = a\,(t,X_t)\,\mathrm{d}t + b\,(t,X_t)\,\mathrm{d}W_t \tag{5.18}$$

which shows that the correct interpretation of the Langevin equation is in terms of increments of the variable X_t over a time-interval dt. Equation (5.18) can be expressed as a stochastic integral equation:

$$X_t = X_{t_0} + \int_{t_0}^{t} a(t',X_{t'})\mathrm{d}t' + \int_{t_0}^{t} b(t',X_{t'})\mathrm{d}W_{t'} \tag{5.19}$$

where the second integral is a stochastic integral.

The treatment of stochastic integrals do not obey the rules of classical (Riemann-Stiejles) integration. This is due to the property of infinite variation of the Wiener process on every finite time interval. In classical integration the limit of the following sum ($\tau_k \in [t_k,t_{k+1}]$):

$$\int_{t_0}^{t} b(t',X_{t'})\mathrm{d}W_{t'} = \lim_{N\to\infty} \sum_{k=0}^{N} b(\tau_k,X_{\tau_k})(W_{t'_{k+1}} - W_{t'_k}) \tag{5.20}$$

should be independent of the choice of τ_k. However, because of the infinite variation property of the Wiener process this limit does dependent on τ_k. Two main approaches exist in the literature, the Itô and Stratonovich definitions. In the Itô definition $\tau_k = t_k$ while in the Stratonovich definition $2\tau_k = t_k + t_{k+1}$. Both methods have their advantages and disadvantages (Peirano et al., 2006). In this work all stochastic integrals are interpreted in the Itô sense and thus 5.20 becomes:

$$\int_{t_0}^{t} b(t',X_{t'})\mathrm{d}W_{t'} = \lim_{N\to\infty}\sum_{k=0}^{N} b(t'_k,X_{t'_k})(W_{t'_{k+1}} - W_{t'_k}) \tag{5.21}$$

In the Itô sense the rules of ordinary differential calculus are no longer valid but the properties of zero mean and isometry hold (Peirano et al., 2006). The Itô sense is preferred to the Stratonovich sense because the zero mean and isometric properties are extensively used in the derivation of the second order numerical scheme employed to solve the system of stochastic differential equations (Minier et al., 2003; Peirano et al., 2006).

5.2.3 Model for the seen instantaneous fluid velocity

Langevin equations have been used for some years to simulate single phase turbulent flow field (particles are fluid particles in this case). Each one of the three components of the instantaneous velocity vector of fluid particles is given by a Langevin equation. Minier and Pozorski (1997); Pope (1985) present the derivation of the drift and diffusion coefficients and they have showed that the stochastic equation that is obtained have a clear correspondence to Reynolds Stress Models. Heavy particles (i.e. the particle relaxation time is not zero) do not follow the trajectories of fluid particles and thus the Langevin equation must be modified to predict the instantaneous fluid velocity seen by the heavy particles. Minier and Peirano (2001) derived a modified Langevin equation for the seen instantaneous fluid velocity. For simplicity, we only give the expression of the Langevin equation when the first axis of the reference system is assumed to be aligned with the mean relative velocity . The general expression is given in Minier and Peirano (2001). The Langevin equation for the seen instantaneous fluid velocity writes:

$$\begin{aligned}
\mathrm{d}U_{s,i} &= -\frac{1}{\rho_f}\frac{\partial\overline{P}}{\partial x_i}\mathrm{d}t \\
&+ \left(\overline{U}_{p,j} - \overline{U}_{f,j}\right)\frac{\partial\overline{U}_{f,i}}{\partial x_j}\mathrm{d}t \\
&- \frac{1}{T^*_{L,i}}\left(U_{s,i} - \overline{U}_{f,i}\right)\mathrm{d}t - S_{U_{p\to f},i}\mathrm{d}t \\
&+ \sqrt{\varepsilon\left(C_0 b_i\tilde{k}/k + \frac{2}{3}\left(b_i\tilde{k}/k - 1\right)\right)}\,\mathrm{d}W_i(t)
\end{aligned} \tag{5.22}$$

where the $\overline{*}$ mean operator is explicitly mentioned to avoid confusion between instantaneous and mean variables. In the above equation the mean gas phase properties ($\overline{U}_{f,j}$, $\overline{P}$, ρ_f, ε, k) are interpolated at the particle position and $\overline{U}_{p,j}$ is the cell averaged mean velocity of the particle. The source term $S_{U_{p\to f},i}$ accounts for two-way coupling effects. According to Csanady's analysis (Csanady, 1963) the integral time-scale of the seen instantaneous velocity differs from the fluid Lagrangian integral time-scale T_L. The difference is due to the crossing trajectory effect, a consequence of the action of the gravity field on the particles. The modified time-scale is expressed as:

$$T^*_{L,3} = \frac{T_L}{\sqrt{1+\beta^2 \frac{|\overline{\mathbf{U}}_r|^2}{2k/3}}} \tag{5.23}$$

$$T^*_{L,1} = T^*_{L,2} = \frac{T_L}{\sqrt{1+4\beta^2 \frac{|\overline{\mathbf{U}}_r|^2}{2k/3}}} \tag{5.24}$$

The gravity field is assumed to be aligned with the direction labelled 3 and the parameter β is the ratio of the fluid Lagrangian time-scale to the fluid Eulerian time-scale. The ratio is taken to be $\beta = 0.714$ which was obtained by simulation of isotropic turbulence (Ichard and Melheim, 2010). The fluid Lagrangian time-scale is given by the following expression:

$$T_L = \frac{k}{\varepsilon\left(\frac{1}{2}+\frac{3C_0}{4}\right)} \tag{5.25}$$

In the above equation, C_0 is the Kolmogorov constant which is supposed to be an universal constant. The value $C_0 = 2.1$ is often quoted in the literature (Pope, 1985). However, it has be shown that C_0 might be Reynolds number dependent and increases with Reynolds number up to an asymptotic value of 6 to 7 (Walpot et al., 2007). In our work we use the relation proposed by Fox and Yeung (2003):

$$C_0 = 6.5\left[1+\frac{8.1817}{\mathrm{Re}_\lambda}\left(1+\frac{110}{\mathrm{Re}_\lambda}\right)\right]^{-1} \tag{5.26}$$

The Taylor Reynolds number can be calculated using (Walpot et al., 2007):

$$\mathrm{Re}_\lambda = \sqrt{\frac{20k^2}{3\varepsilon\nu}} \tag{5.27}$$

Finally, in Equation (5.22) the weighted kinetic energy is given by the following expression:

$$\tilde{k} = \frac{3}{2}\frac{\sum_{i=1}^{3} b_i \overline{u_{f,i}^2}}{\sum_{i=1}^{3} b_i} \qquad b_i = \frac{T_L}{T^*_{L,i}} \tag{5.28}$$

In the equation above, $u_{f,i}$ represents the fluctuating fluid velocity.

5.2.4 Vaporization of liquid droplets

The vaporizing droplet problem is a challenging issue in fluid dynamics. It is part of many engineering situations involving the transport and computation of sprays: fuel injection, spray painting, aerosol spray, flashing releases. In most of these engineering situations there is a relative motion between the droplet and the surrounding gas. The gas flow over the droplet has many features of the gas flow over a rigid sphere: pressure gradient, viscous boundary layer, wake. In addition to these common flow features one can also mention the internal liquid circulation phenomenon driven by surface-shear forces and the boundary layer blowing effect. One of the key parameters which characterizes the gas flow over the droplet is the droplet Reynolds number based on the relative velocity, droplet diameter and gas phase properties. The features of the gas flow have a critical impact on the exchanges of mass, momentum, and energy between the gas and the liquid phases and thus, they have to be properly accounted for in any vaporizing droplet model. The time evolution of the droplet radius, r_d, and droplet temperature, T_d, can be computed by solving the following set of ordinary differential equations (Crowe et al., 1998):

$$\frac{\mathrm{d}r_d}{\mathrm{d}t} = -\frac{\dot{m}_F}{4\pi r_d^2 \rho_L} \tag{5.29}$$

$$\frac{\mathrm{d}T_d}{\mathrm{d}t} = \frac{Q_L}{\frac{4}{3}\pi r_d^3 \rho_L C_{pL}} \tag{5.30}$$

where, ρ_L is the liquid density, $\dot{m}_F$ is the vaporization rate of the droplet, C_{pL} is the liquid specific heat at constant pressure and Q_L is the heat flux entering the droplet. The heat flux entering the droplet can be expressed as (Crowe et al., 1998):

$$Q_L = Q_g - \dot{m}_F L_{vap} \tag{5.31}$$

where Q_g is the heat flux from the gas to the droplet surface and L_{vap} is the latent heat of vaporization.

Isolated spherically symmetric droplet vaporization case

A single, pure component droplet is considered and the gas phase is assumed to behave as an ideal gas. For now, we assume that there is no relative motion between the droplet and the gas, $Re_d = 0$. A spherically symmetric field exists for the gas field surrounding the droplet. Analytical expressions for $\dot{m}_F$ and Q_g are found by considering heat and mass transfer processes in the gas film surrounding the droplet (Abramzon and Sirignano, 1989). The droplet vaporizes and creates a radial flow field in the gas film. Vapour from the droplet is transported away from the surface by convection and diffusion, and heat is conducted radially against the convection toward the droplet interface. This process is called Stefan convection, or Stefan flow (Sirignano, 1999).

It is assumed that the gas phase heat and mass transfer processes are quasi-steady and that the thermo-physical properties might be considered as constant. The assumption of quasi-steadiness of the gas phase finds its limitation in situations in which the gas film surrounding the droplet is in a near-critical state or in a situation in which the gas field is submitted to an acoustic field. The assumption of constant thermo-physical properties is found to be satisfying provided that the properties are

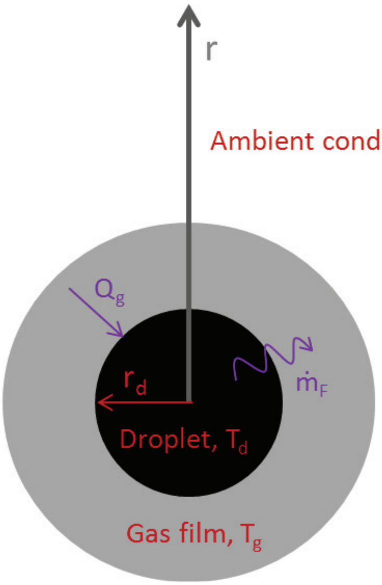

Figure 5.2: *Sketch of a vaporizing droplet.*

evaluated at some reference conditions (Hubbard et al., 1975):

$$T_r = T_s + A_r (T_\infty - T_s) \tag{5.32}$$

$$Y_r = Y_{F,s} + A_r (Y_{F,\infty} - Y_{F,s}) \tag{5.33}$$

where T_r is the reference temperature, T_s is the temperature at the droplet surface, T_∞ is the temperature of the gas far away from the droplet surface, Y_r is the reference fuel mass fraction, $Y_{F,s}$ is the fuel mass fraction at the droplet surface and $Y_{F,\infty}$ is the fuel mass fraction far away from the droplet surface. Hubbard et al. (1975) recommend the ”1/3” averaging rule:

$$A_r = \frac{1}{3} \tag{5.34}$$

The expression for the droplet vaporization rate is given by:

$$\dot{m}_F = 4\pi \rho_g \mathcal{D} r_d \ln(1 + B_M) \tag{5.35}$$

and

$$B_M = \frac{Y_{F,\infty} - Y_{F,s}}{Y_{F,s} - 1} \tag{5.36}$$

where B_M is the Spalding mass transfer number and $\mathcal{D}$ is the mass diffusivity. Phase equilibrium is assumed at the droplet surface and the mole fraction of fuel vapour at the droplet surface is obtained via the use of Clapeyron's equation. The following equation for Q_g can be derived:

$$Q_g = 4\pi r_d \lambda_g \frac{\ln(1+B_T)}{B_T}(T_\infty - T_d) \tag{5.37}$$

where λ_g is the thermal conductivity of the gas and B_T is the Spalding heat transfer number. The rate of vaporisation for the droplet can be expressed as a function of the Sherwood number Sh. The Sherwood number describes the non-dimensional mass transfer rate to the droplet. The expression for the droplet vaporization rate can be re-written as:

$$\dot{m}_F = 2\pi r_d \mathcal{D} \rho_g B_M \,\mathrm{Sh} \tag{5.38}$$

Similarly, the conductive heat transfer from the gas to the droplet can be expressed as a function of the Nusselt number. The Nusselt number describes a non-dimensional heat transfer rate to the droplet. We obtain:

$$Q_g = 2\pi r_d \lambda_g \mathrm{Nu}(T_\infty - T_d) \tag{5.39}$$

The relative motion between a droplet and the gas results in an increase of the heat and mass transfer rates in the gas film surrounding the droplet. A convective boundary layer and a wake can surround the droplet. Furthermore, the shear force on the liquid surface causes an internal circulation that enhances the heating of the liquid. As a consequence, the vaporization rate increases with the droplet Reynolds number. Many different models exist for the single convective droplet vaporization case.

The infinite liquid conductivity model

Vaporizing droplet models can be seen to belong to six different classes (Sirignano, 1999):

- constant droplet temperature model ($d^2 law$) *(i)*.
- infinite liquid conductivity model *(ii)*.
- spherically symmetric transient droplet heating model *(iii)*.
- effective conductivity model *(iv)*.
- vortex model of droplet heating *(v)*.
- Navier-Stokes solution *(vi)*.

The main difference between all these models is the treatment of the heating of the liquid phase which is usually the rate controlling phenomenon in droplet vaporization (Sirignano, 1999). The first three models do not consider internal liquid circulation. The effective conductivity model *(iv)* and the vortex model of droplet heating *(v)* account for internal circulation and internal convective heating. The direct resolution of the Navier-Stokes equations provides, in principle, exact solutions both for the gas phase and the liquid phase. It is interesting to note that model *(i)* is a simplification of model *(ii)* which is in turn a simplification of model *(iii)*. The spherically symmetric transient droplet heating model *(iii)* solves the equation for heat diffusion through the liquid phase. A droplet heating time τ_h can be defined as the time required for a thermal diffusion wave to penetrate from the droplet surface to its center. The droplet heating time is compared to the droplet lifetime, τ_l. If the droplet heating time is short compared to the droplet lifetime we can assume that the temperature field inside the droplet is uniform and model *(ii)* is obtained. In the infinite liquid conductivity model *(ii)* the temperature of the droplet is uniform but varies with time. It is possible to go one step further and find the conditions for which we can neglect the temporal variation of the droplet temperature. The liquid temperature varies in time until the wet-bulb temperature is reached. If the wet-bulb temperature is reached in a time of the same order of magnitude than the droplet heating time then the liquid temperature can be considered to be constant with regards to time. Model *(i)*, the $d^2 - law$, is obtained.

The infinite liquid conductivity model is widely used in industrial spray calculations (Aggarwal and Peng, 1995; Aggarwal et al., 1984) for its balance between computational costs and accuracy. To account for the convective effects which enhanced the heat and mass transfer rates around the droplet, a correction is applied to the spherically symmetric expressions of the Sherwood and Nusselt numbers (Abramzon and Sirignano, 1989):

$$\dot{m}_F = 4\pi\rho_g \mathcal{D} r_d \,\mathrm{Sh}^* \ln(1+B_M) \tag{5.40}$$

$$Q_g = 2\pi r_d \lambda_g \mathrm{Nu}^* \frac{\ln(1+B_T)}{B_T} (T_\infty - T_d) \tag{5.41}$$

Abramzon and Sirignano (1989) suggest the following formulation for the modified Sherwood and Nusselt numbers:

$$Sh^* = 2 + \frac{Sh_0 - 2}{F_M} \tag{5.42}$$

$$Nu^* = 2 + \frac{Nu_0 - 2}{F_T} \tag{5.43}$$

where the functions F_M and F_T account for surface blowing which results in a thickening of the boundary layer surrounding the droplet. The well-known Frossling correlations, or Ranz-Marshall correlations (Crowe et al., 1998), can be used to express Nu_0 and Sh_0:

$$\mathrm{Sh}_0 = 2 + 0.552 \mathrm{Re}^{\frac{1}{2}} \mathrm{Sc}^{\frac{1}{3}} \tag{5.44}$$

$$\mathrm{Nu}_0 = 2 + 0.552 \mathrm{Re}^{\frac{1}{2}} \mathrm{Pr}^{\frac{1}{3}} \tag{5.45}$$

where Sc is the Schmidt number and Pr is the Prandtl number. The expressions above show that the heat and mass transfer rates increase with increasing Reynolds number.

5.3 Source terms in the continuous phase equations

The continuous phase is solved in the Eulerian reference frame. The gas phase conservation equations of mass, momentum, energy, specie mass fraction, turbulent dissipation rate and turbulent kinetic energy are discretized and solved on a Cartesian grid. The continuous phase equations are given in Chapter 4, Sections 4.1.2 and 4.1.3. Appropriate source terms must be added to the right hand side of these equations in order to account for the effects of the liquid droplets on the gas phase. Two-way coupling can occur through mass, momentum and energy exchanges between the two phases. The gas phase turbulence can also be modified by the presence of the particles.

5.3.1 Two-way coupling through mass, momentum and energy

A mass source term S_m is added to the right hand side of the gas phase continuity equation. The mass source term is equal to the vaporization rate of the liquid phase:

$$S_{m_{p\to f}} = \frac{1}{V}\sum_{n=1}^{N} \dot{m}_{F,n} \tag{5.46}$$

where N is the total number of droplets inside the volume V and $\dot{m}_{F,n}$ is the vaporization rate of a droplet.

As far as momentum is concerned, one term must be added in the expression for the instantaneous fluid velocity seen by the particles (Equation (5.22)) as well as one term in each of the three equations for the gas phase momentum. This term has the following form (Peirano et al., 2006):

$$S_{U_{p\to f},i} = \frac{\alpha_p \rho_p}{\alpha_f \rho_f}\frac{U_{p,i} - U_{s,i}}{\tau_p} \tag{5.47}$$

This term appears with a minus sign in Equation (5.22) and with a plus sign in the fluid momentum equations. The parameters α_p and α_f represent the volume fractions of the two phases.

A source term S_h is added to the gas phase conservation equation of enthalpy to account for the effects of droplets vaporization. The source term S_h is composed of two contributions: the first contribution represents the heat received by the droplet for its heating and vaporization, the second contribution represents the added enthalpy to the gas phase associated with the transfer of mass from the liquid phase to the gas phase:

$$S_{h_{p\to f}} = \frac{1}{V}\sum_{n=1}^{N} \left(\dot{m}_{F,n} h_v\left(T_{p,n}\right) - Q_{g,n}\right) \tag{5.48}$$

where $h_v(T_{p,n})$ is the enthalpy of the vapour evaporating form the droplet and $Q_{g,n}$ is the heat captured by the droplet and it is given by equation 5.41.

5.3.2 Turbulence modulation

The influence of particles on the turbulence equations remains an open question and no model has so far been able to reproduce the entire spectrum of experimental measurements. Experimental data seem to show that small particles attenuate, dampen, the fluid turbulence whereas large particles increase the level of fluid turbulence.

Mandø et al. (2009) proposed a new derivation of the source term for particle-turbulence interaction. This source term is introduced inside the equation for the turbulent kinetic energy and writes:

$$S_{k_{p\to f}} = \frac{\alpha_p \rho_p}{\tau_p}\left(\left|\overline{U}_{f,i} - \overline{U}_{p,i}\right|^2 - 2k\right) \tag{5.49}$$

The additional dissipation due to the particles is assumed to be proportional to the source term in the turbulent kinetic energy equation (Mandø et al., 2009):

$$S_{\varepsilon_{p\to f}} = C_{4\varepsilon}\frac{\varepsilon}{k}S_{k_p} \tag{5.50}$$

The constant $C_{4,\varepsilon}$ takes the value 1.1 and the new source term is introduced inside the equation for the turbulent dissipation ε.

5.4 Algorithm of the Euler-Lagrange approach

All the steps involved in the computations of a two-phase flow field with the Euler-Lagrange approach are summarized in this section. First, we define the variables that appear in Figure 5.3. The set of fluid mean quantities is represented by $C(t_n)$; the set of fluid mean quantities interpolated at particle locations is denoted $C_N(t_n)$; the set of variables attached to the particle is written $D(t_n)$ and $D_x(t_n)$ corresponds to the set of statistics, defined at cell centres, extracted from $D(t_n)$. The first step consists in solving the set of fluid RANS equations to obtain the set of mean fluid quantities at the time $t_{n+1} = t_n + dt$. The first step needs the set of quantities $D_x(t_n)$ because of the additional source terms in the RANS equations which arise from the two-way coupling. The next step concerns the interpolation of the cell quantities to the particle locations. The Lagrange solver solves the following set of equations:

$$\frac{\mathrm{d}x_{p,i}}{\mathrm{d}t} = U_{p,i} \tag{5.51}$$

$$\frac{\mathrm{d}U_{p,i}}{\mathrm{d}t} = \frac{1}{\tau_p}\left(U_{s,i} - U_{p,i}\right) + g_i \tag{5.52}$$

$$\mathrm{d}U_{s,i} = A_{s,i}\mathrm{d}t + B_{s,ij}\mathrm{d}W_j(t) \tag{5.53}$$

$$\frac{\mathrm{d}r_d}{\mathrm{d}t} = -\frac{\dot{m}_F}{4\pi r_d^2 \rho_L} \tag{5.54}$$

$$\frac{\mathrm{d}T_d}{\mathrm{d}t} = \frac{Q_L}{\frac{4}{3}\pi r_d^3 \rho_L C_{pL}} \tag{5.55}$$

A simplified notation has been used for the equation for the seen instantaneous velocity, Equation (5.53). The first term on the right hand side, $A_{s,i}$ is the deterministic term and the second term $B_{s,ij}\mathrm{d}W_j(t)$ is the diffusive term. Equation (5.22) shows the detailed expression. The Lagrange solver is composed of a second order numerical scheme which has been specifically developed to handle stochastic differential equations

$$\begin{array}{lcl}
\mathcal{C}(t_n)\,\mathcal{D}^x(t_n) & \xrightarrow[\text{RANS Solver}]{\qquad\qquad\qquad} & \mathcal{C}(t_{n+1}) \\
\mathcal{C}(t_n)\,\mathcal{D}^x(t_n) & \xrightarrow[\text{Interpolation}]{\qquad\qquad\qquad} & \mathcal{C}^N(t_n)\,\mathcal{D}(t_n) \\
\mathcal{D}(t_n)\,\mathcal{C}^N(t_n) & \xrightarrow[\text{Lagrange solver}]{\qquad\qquad\qquad} & \mathcal{D}(t_{n+1}) \\
\mathcal{D}(t_{n+1}) & \xrightarrow[\text{Average in cells}]{\qquad\qquad\qquad} & \mathcal{D}^x(t_{n+1})
\end{array}$$

Figure 5.3: *Algorithm of the Euler-Lagrange approach.*

(Peirano et al., 2006). Due to the properties of the Wiener process regular numerical schemes that are employed to solve Ordinary Differential Equations (ODE) cannot be used to solve SDE. Finally, in the last step statistics (mainly the mean) of particle quantities are evaluated in each cell. The statistics are understood in the sense of mass-weighted averages. As far as boundary conditions at the wall are concerned, particles are assumed to deposit when they impact on an obstacle. This simple boundary condition should give acceptable results for liquid particles. Boundary conditions at the wall would need to be improved in the future. A first order Euler scheme is used to solve the ordinary differential equations governing the droplet diameter and droplet temperature. The time-step is set to $dt_{euler} = min\left(10^{-5}, dt\right)$ where dt is the time-step used for the continuous phase equations and for the Stochastic Differential Equations.

5.5 Validation with laboratory scale experiments

5.5.1 The experiments of Hardalupas *et al.*

Description of the experiments

In this sub-section a validation test case which aimed at evaluating the model for the particle motion (i.e. Equations 5.51, 5.52 and 5.53) is presented. The turbulent dispersion of solid particles is considered and the experiment of Hardalupas et al. (1989) is simulated. A round turbulent air jet laden with solid particles was studied experimentally. The jet was directed vertically downward and the velocity and flux of spherical glass beads with diameters of 200, 80 and 40 μm were measured with a Phase Doppler Anemometry (PDA) system. The orifice diameter was 15 mm and the jet exit velocity was 13 m/s giving a Reynolds number of 13000. The fluid integral time-scale was estimated to be 1.15 ms whereas the glass beads of diameters 200, 80 and 40 μm had a particle relaxation time τ_p of 298, 48 and 12 ms respectively. For each particle diameter, experiments with two different mass loading were conducted. The effects of particles inertia and particle mass loading on the particle phase and continuous phase statistics were investigated.

Set-up of the simulations

A grid sensitivity study is performed and three grids with 30000, 213000 and 1600000 cells are considered. The results obtained with the grid having 213000 cells are practically identical to the results obtained with the grid having 1600000 cells. All the computations are done with a grid of 213000 cells. The grid is uniform with a resolution of 7.5 mm. The time-step is set to 4.3 10^{-4} s which is smaller than any of the particle's relaxation times. A sensitivity study is conducted on the number of parcels injected at each time-step: 1600, 160, 50 and 16 parcels per time-step are tested. The results obtained by injecting 1600 parcels per time-step are identical to the results obtained by injecting 160 parcels at each time-step. Therefore, the computations are done with 160 parcels per time-step. The profiles of mean variables are averaged over 1000 time-steps once the flow field has reached a steady state. Steady state is reached 1.4 s after the start of the release.

Results and discussions

First, the results concerning the axial profiles of the mean axial velocity of the particles shown on Figure 5.4 are discussed. For all the figures in this section, the legend clean jet refers to the air jet without particles, i.e. a regular single phase air jet, and acts as reference. The velocity $U_{f,0}$ is the exit velocity of the clean jet. The numerical results are in perfect agreement with the experimental observations. For the particles with diameters 80 μm and 200 μm the axial profiles of mean axial velocity are insensitive to the variations of the mass loading ratio. However, the axial profiles of the 40 μm particles are sensitive to the variation of the mass loading. For the particles with diameter 40 μm the axial decay of the mean axial velocity is decreased when the mass loading increases. When the particle loading increases a transfer of momentum occurs between the particle phase and the fluid phase. This transfer is operated by the two-way coupling source terms. The mean gas velocity increases and thus the decay rate of the particle axial mean velocity is decreased. The effect of particle inertia is also illustrated on Figure 5.4. The particle inertia increases with the particle diameter. The particle relaxation time of the 200 μm glass beads is 298 ms way larger than the fluid integral time-scale and thus the axial velocity of the beads is not affected by the variations of the mean gas flow field. The mean axial velocity of the 200 μm beads is almost constant over a distance equal to 30 times the exit diameter.

Figure 5.5 shows the axial profiles of particle axial rms velocity. A large disagreement exists for the clean jet predictions close to the exit orifice. This discrepancy is decreased as the distance downstream of the exit orifice increases and from $x/D = 10$ the predictions are very satisfying. The results for the particle phase are in very good agreement with the experimental data. As for the mean axial velocity profiles the effect of inertia is clearly visible. The glass beads with diameters 80 μm and 200 μm have a lower axial rms velocity than the gas phase and do not follow the variation imposed by the gas phase. The rms velocity of the 40 μm particles increases over the first 15 orifice diameters and for the highest loading ratio the 40 μm beads have an axial rms velocity which is larger than the one of the gas phase for $x > 15D_{ori}$. Figure 5.6 shows the axial profiles of particle radial rms velocity. The numerical predictions are again in good agreement with the experimental data. The radial rms

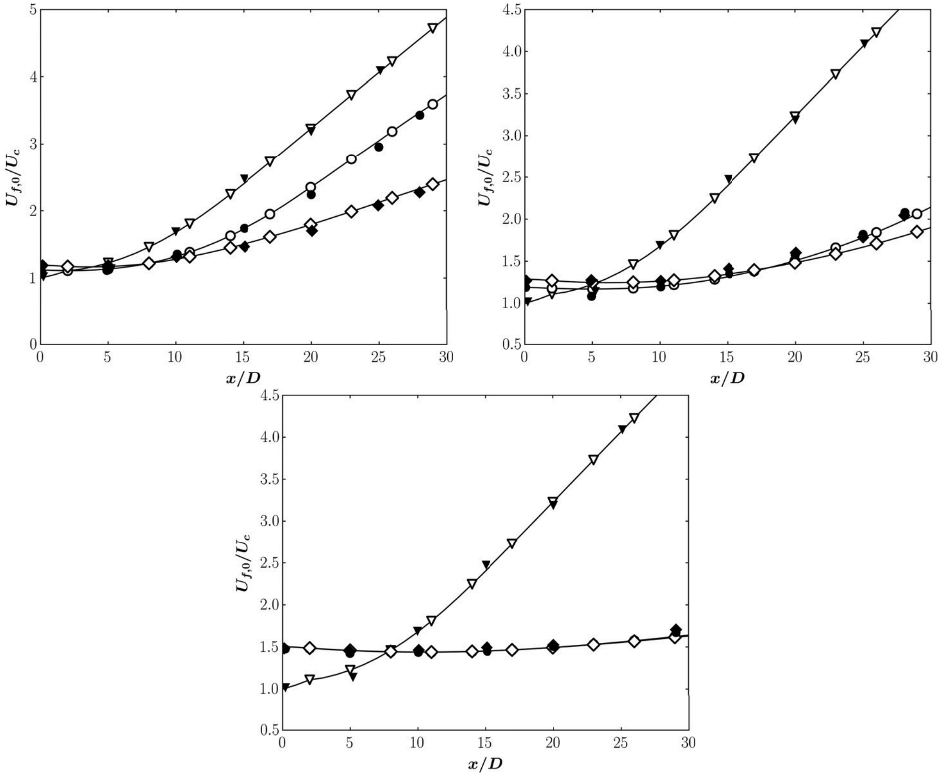

Figure 5.4: *Axial profiles of particles mean axial velocities. Experiments of Hardalupas et al. (1989). The black symbols represent experimental data and white symbols simulations. (∇) is the clean jet.* ***Top left****, for the 40 µm particles: (◯) loading 0.13 and (◇) loading 0.8.* ***Top right****, for the 80 µm particles: (◯) loading 0.23 and (◇) loading 0.86.* ***Bottom****, for the 200 µm particles: (◯) loading 0.13 and (◇) loading 0.37.*

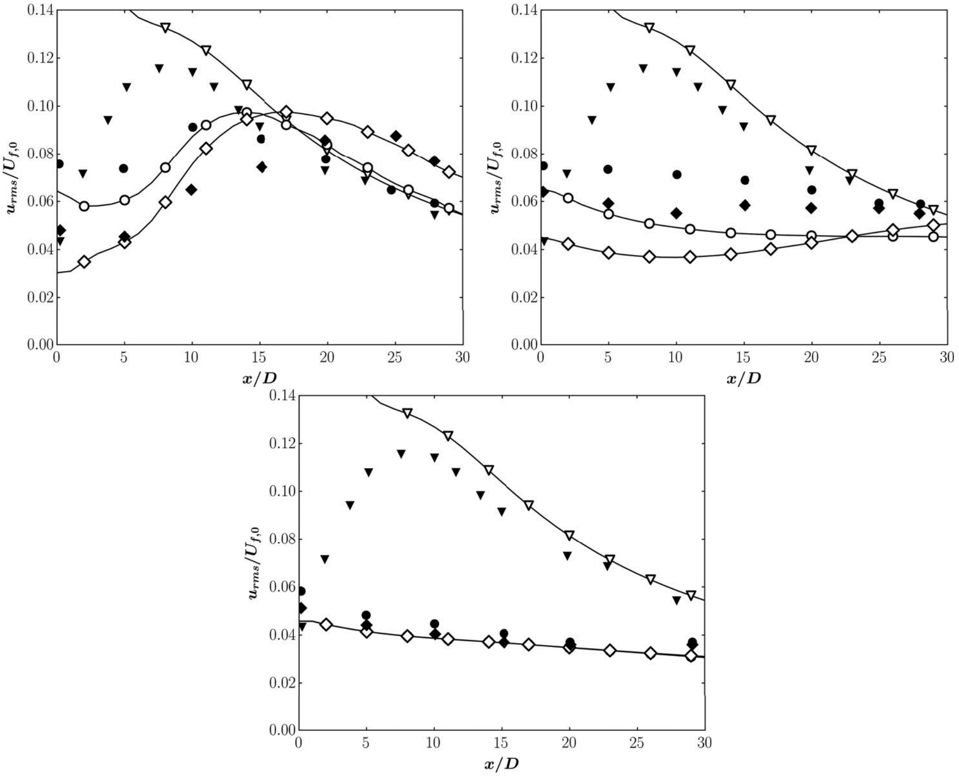

Figure 5.5: *Axial profiles of particles axial rms velocities. Experiments of Hardalupas et al. (1989). The black symbols represent experimental data and white symbols simulations. (∇) is the clean jet.* ***Top left****, for the 40 µm particles: (◯) loading 0.13 and (◇) loading 0.8.* ***Top right****, for the 80 µm particles: (◯) loading 0.23 and (◇) loading 0.86.* ***Bottom****, for the 200 µm particles: (◯) loading 0.13 and (◇) loading 0.37.*

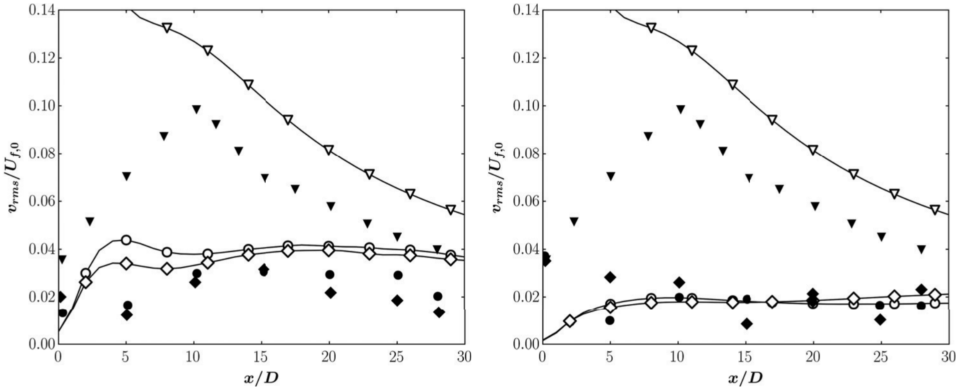

Figure 5.6: *Axial profiles of particles radial rms velocities. Experiments of Hardalupas et al. (1989). The black symbols represent experimental data and white symbols simulations. (∇) is the clean jet.* ***Left****, for the 40 μm particles: (◯) loading 0.13 and (◇) loading 0.8.* ***Right****, for the 80 μm particles: (◯) loading 0.23 and (◇) loading 0.86.*

velocity is lower than the axial rms velocity which demonstrates a large anisotropy in the turbulence of the beads.

Radial profiles at the location $x/D_{ori} = 28$ are now inspected. Figure 5.7 depicts the radial profiles of mean axial velocity of the particles. The numerical profiles are slightly wider than the experimental profiles indicating that the dispersion of the particles is slightly over-estimated in the simulations. Figure 5.8 shows the radial profiles of axial particle rms velocity. The shape of the profiles are well predicted in our simulations and as for the mean axial velocity the width of the profiles is slightly over-estimated.

The statistics of the fluid phase are now discussed. Figure 5.9 shows the axial profiles and radial profiles of axial mean fluid velocity for the 80 μm beads. For the axial profiles the predictions are in very good agreement with the experimental observations. The axial decay of fluid axial mean velocity is decreased when the particle loading increases. Two-way coupling effects are well predicted by our model. Figure 5.10 depicts the axial and radial profiles of axial fluid rms velocity. The axial fluid rms velocity is largely over-estimated in the simulation. It might be due to the source terms $S_{k_{p \to f}}$ and $S_{\varepsilon_{p \to f}}$ which over-estimates the production of turbulence associated to the presence of the particles. This over-estimated fluid turbulence could also explain the too wide radial profiles for the particle axial mean velocity.

5.5.2 The experiments of Sheen *et al.*

Description of the experiments

The experiments conducted by Sheen et al. (1994) are also used to validate the Euler-Lagrange models. The experiments performed by Sheen et al. are similar to the previously discussed experiments of Hardalupas et al. (1989). Downward particle-laden turbulent air jets were studied by means of a Laser-Doppler Anemometer. The nozzle diameter was 15 mm and the jet centreline exit velocity was 20 m/s which gives a Reynolds number of 20000, similar to the Reynolds number of the Hardalupas *et al.*

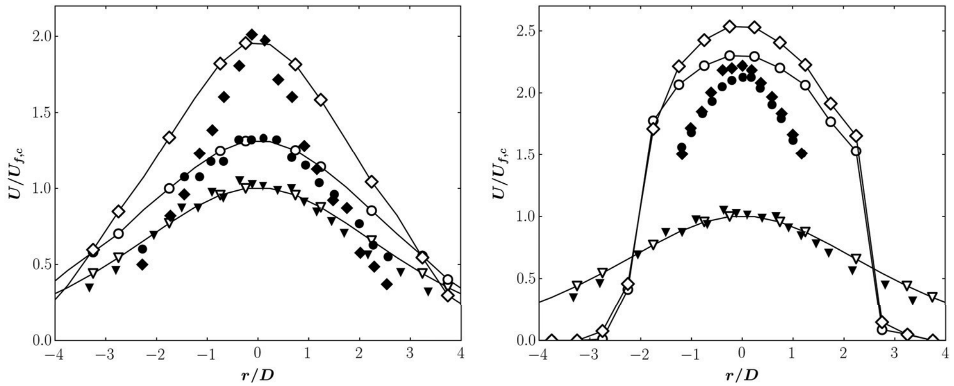

Figure 5.7: *Radial profiles of particles axial mean velocities at $x/D = 28$. Experiments of Hardalupas et al. (1989). The black symbols represent experimental data and white symbols simulations. (∇) is the clean jet.* ***Left****, for the 40 μm particles: (◯) loading 0.13 and (◇) loading 0.8.* ***Right****, for the 80 μm particles: (◯) loading 0.23 and (◇) loading 0.86.*

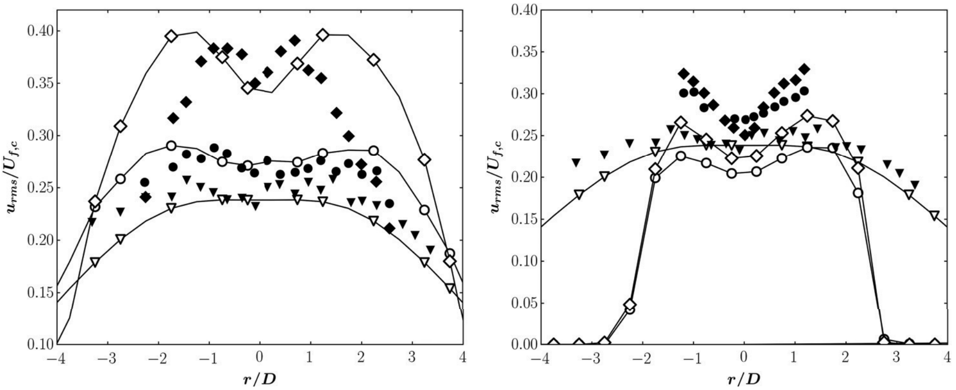

Figure 5.8: *Radial profiles of particles rms velocities at $x/D = 28$. Experiments of Hardalupas et al. (1989). The black symbols represent experimental data and white symbols simulations. (∇) is the clean jet.* ***Left****, for the 40 μm particles: (◯) loading 0.13 and (◇) loading 0.8.* ***Right****, for the 80 μm particles: (◯) loading 0.23 and (◇) loading 0.86.*

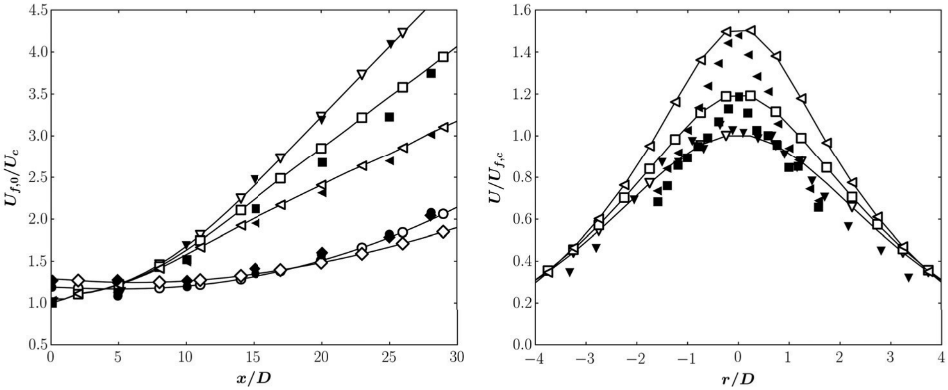

Figure 5.9: *Axial and radial (at $x/D = 28$) profiles of mean particle and fluid axial velocities for 80 µm particles. Experiments of Hardalupas et al. (1989). The black symbols represent experimental data and white symbols simulations. (∇) is the clean jet. ($\bigcirc$) represents particle mean velocity with loading 0.23 and ($\diamond$) represents particle mean velocity with loading 0.86. ($\square$) represents fluid mean velocity with loading 0.23 and ($\triangleleft$) represents fluid mean velocity with loading 0.86.*

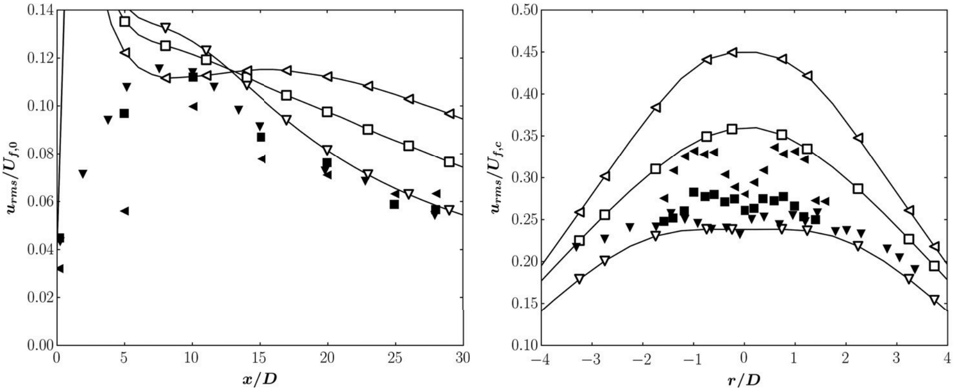

Figure 5.10: *Axial and radial (at $x/D = 28$) profiles of fluid axial rms velocities for 80 µm particles. Experiments of Hardalupas et al. (1989). The black symbols represent experimental data and white symbols simulations. (∇) is the clean jet. ($\square$) represents fluid mean velocity with loading 0.23 and ($\triangleleft$) represents fluid mean velocity with loading 0.86.*

experiment. Three main differences exist between the Sheen *et al.* experiments and the Hardalupas *et al.* experiments. First, the diameters and inertia of the solid particles are larger than the ones in the experiments of Hardalupas *et al.*: particles with diameters 210, 460 and 780 μm and time constants of 163, 807 and 2298 ms respectively were considered. Second, a wide range of mass loading ratios was investigated in the experiment of Sheen et al.: from 0 to 3.6. Third, the measurement range extended from the nozzle exit down to $90D$ downstream, approximately twice the size of the measurement range of the Hardalupas *et al.* experiments.

Set-up of the simulations

The setup of the simulations was identical to the setup used to simulate the experiments of Hardalupas *et al.*

Results and discussions

The results for the mean velocity fields, particle and gas are discussed. Figure 5.11 illustrates the variations of the mean velocity fields as a function of the mass loading at the axial position $x = 20D$. The centreline axial mean velocity is considered. As far as the axial mean particle velocity is concerned, the experimental data and numerical predictions are in very good agreement. For the two largest particle diameters 460 and 780 μm the axial mean velocity of the particles is not affected by the mass loading. This observation is also valid for the 200 μm particle diameters of the Hardalupas *et al.* experiments (see Figure 5.4). The axial mean velocity of particles with diameter 210 μm slightly increases with the mass loading. At $x/D = 20$ the particles with a diameter of 210 μm have the largest velocities. It is an effect of the initial conditions. At the nozzle exit the particles with a diameter of 210 μm have a larger velocity than the other, bigger, particles because they are more sensitive to changes in mean gas phase velocities. A large variation of the mean axial gas phase velocity is seen for the jet laden with the 210 μm particles. The mean axial gas phase velocities of the jets laden with bigger particles are less sensitive to increases in the mass loading.

Figure 5.12 shows the axial mean profiles of gas phase and particles axial velocities for different mass loadings. For all three particle diameters the agreement between observations and predictions is satisfying over the whole measurement range. We can therefore conclude that the models are able to give accurate predictions of the mean fields of solid particle laden jets. Sprays experiments need to be considered in order to assess the performance of the models in simulating droplets laden turbulent air jets.

5.5.3 The experiments of McDonell *et al.*

Description of the experiments

In the early 1990's, McDonell (1990); McDonell and Samuelsen (1995) conducted a series of methanol spray experiments. Their objective was to provide a collection of detailed experimental data for model development, verification and application. They performed reacting and non-reacting experiments with or without atomizing air. A

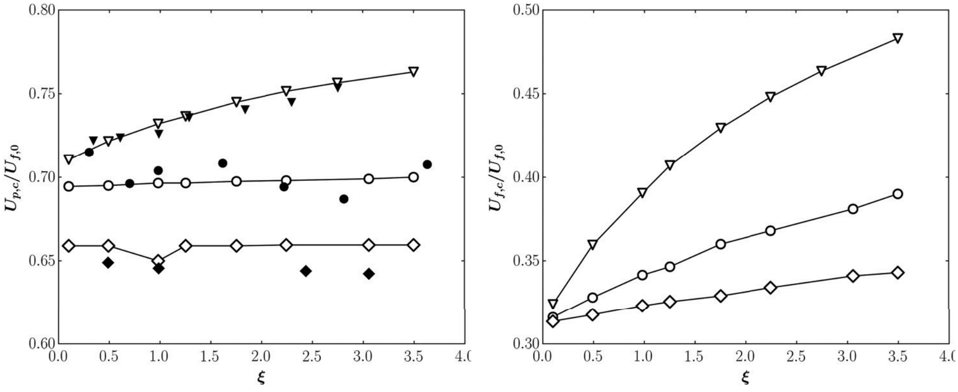

Figure 5.11: *Simulation of the experiment of Sheen et al. (1994). Effects of the mass loading* ξ *on the mean flow statistics at* $x/D = 20$. *The black symbols represent experimental data and white symbols simulations. (∇) represents the particles with diameter 210* μ*m; (○) represents the particles with diameter 460* μ*m and (◇) represents the particles with diameter 780* μ*m.*

swirl (tangential momentum) could be imposed to the atomizing air jets. The non-reacting, non-swirling air assisted spray is considered. The liquid methanol jet is atomized by the air jets producing a fine spray. A sketch of the injector is shown on Figure 5.13. Measurements were obtained for both the gas phase and the dispersed phase. Phase Doppler Interferometry (PDI) and Infrared Extinction Scattering (IRES) measurement techniques were employed. Radial profiles of mean axial and radial velocities (for both the gas phase and the dispersed phase), vapour concentration and droplets diameters are available at six planes downstream of the exit orifice: at 7.5, 25, 50, 75, 100 and 150 mm.

Set-up of the simulations

The data measured at the first plane, 7.5 mm downstream of the exit orifice are used as inlet conditions. The mass flux of methanol at the exit orifice is 1.26 g/s. The vapour mass flux and the liquid mass flux computed at the 7.5 mm plane do not add to the total mass flux of 1.26 g/s. It is very likely that the liquid mass flux is under-estimated. The measurement device may have missed some of the droplets. Indeed, McDonell (1990) report that the instrument may not have been able to sample all the drops passing through the sampling volume. As a consequence, in our computations the liquid mass flux is estimated as:

$$\dot{m}_{l,@7.5mm} = \dot{m}_{total} - \dot{m}_{v,@7.5mm} \tag{5.56}$$

Radial profiles of arithmetic mean droplet diameters and SMD are also reported 7.5 mm downstream of the exit orifice. At each radial position the number of droplets in 50 different size bins was reported and the size distribution could be estimated. In our simulations a somewhat simplified approach is employed: the same size distribution is used at each radial position. Simulations are performed with mono-dispersed and poly-dispersed sprays. For the mono-dispersed spray two different representative diameters

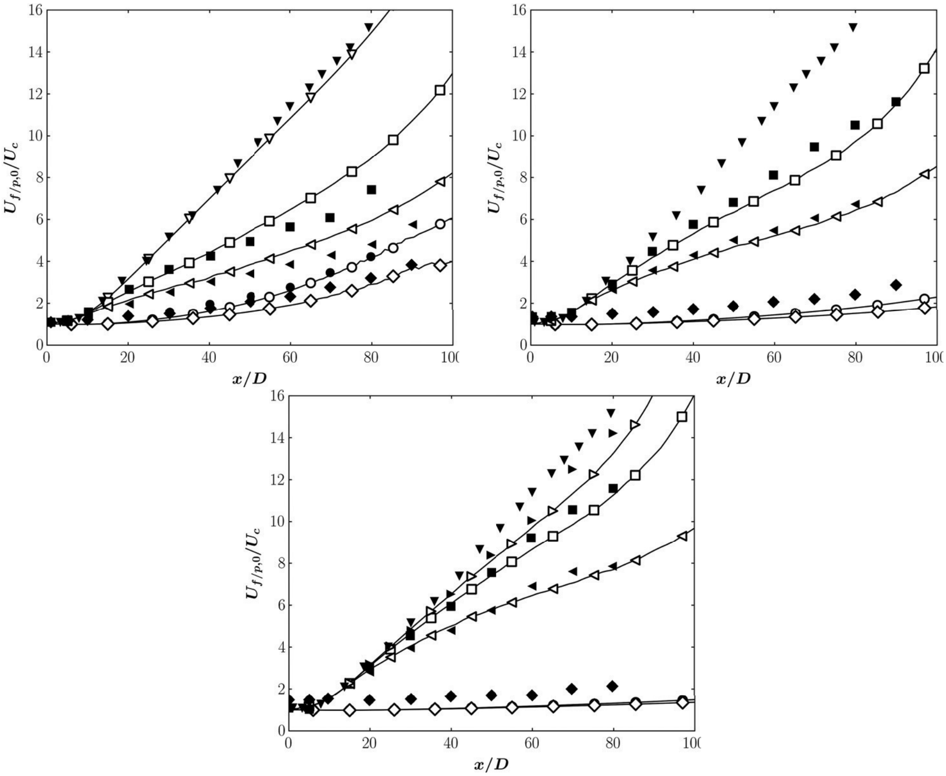

Figure 5.12: *Simulation of the experiment of Sheen et al. (1994). Axial profiles of particle and fluid axial mean velocities. The black symbols represent experimental data and white symbols simulations.* ***Top left****, for the 210 µm particles: (□) represents fluid mean velocity with loading 0.98; (◁) represents fluid mean velocity with loading 2.75; (◯) represents particle mean velocity with loading 0.98 and (◇) represents particle mean velocity with loading 2.75.* ***Top right****, for the 460 µm particles: (□) represents fluid mean velocity with loading 0.98; (◁) represents fluid mean velocity with loading 3.06; (◯) represents particle mean velocity with loading 0.98 and (◇) represents particle mean velocity with loading 3.06.* ***Bottom****, for the 780 µm particles: (▷) represents fluid mean velocity with loading 0.49; (□) represents fluid mean velocity with loading 0.98; (◁) represents fluid mean velocity with loading 2.75; (◯) represents particle mean velocity with loading 0.98 and (◇) represents particle mean velocity with loading 2.75.*

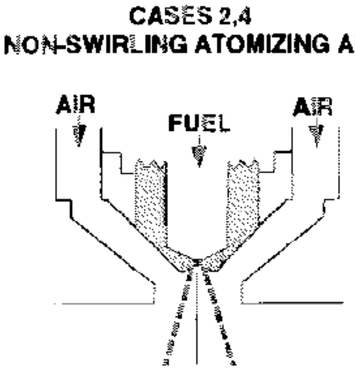

Figure 5.13: *Illustration of the injector used in the experiments of McDonell and Samuelsen (1995) (taken from McDonell and Samuelsen (1995)).*

are tested: the averaged *SMD* and the averaged arithmetic mean diameter, d_{10}, in the measurement plane 7.5 mm downstream. The mono-dispersed size distributions will be referred to as $D10$ and $D32$ size distributions. A log-normal distribution is also used. The *SMD* of the log-normal distribution is the averaged *SMD* in the measurement plane 7.5 mm downstream of the exit orifice and the standard deviation is set to 1.8. The simulations performed with the log-normal distribution will be referred to as *Dlog* in the following. The computations are performed on a grid composed of 600000 cells. The resolution is 2 mm in all directions. The time-step is set to $2\ 10^{-5}$ s. The number of parcels injected at each time-step is 270, giving 31 particles per parcel for the size distribution $D10$ and 8.7 particles per parcel for the size distribution $D32$. These numbers of particles per parcel are lower than the ones used to simulate the Hardalupas *et al.* and Sheen *et al.* experiments. The inlet velocities and temperature of the gas and dispersed phase are equal. The computations are performed without two-way coupling.

Results and discussions

The mean velocity field of the gas phase are first investigated. Figure 5.14 shows the radial profiles of the axial mean velocity of the gas phase. The profiles 7.5 mm downstream of the exit orifice have to be understood as the inlet profiles for the velocity. The agreement between experimental data and numerical predictions is very good for all locations downstream of the exit orifice. As far as the methanol vapour concentration is concerned, Figure 5.15 shows radial profiles of mean methanol concentration at six downstream locations. The first location represents the inlet profile. Three numerical profiles are compared with the experimental data. They correspond to the three different size distributions: $D10$, $D32$, *Dlog*. The concentration is underestimated at all locations but 25 mm downstream. A maximum difference of 35 % exists 150 mm downstream. The same concentration profiles are obtained with the three size distributions. In order to improve the predictions, the temperature of the release is decreased. In the experiments air and methanol were injected at 18-22 °C (McDonell and Samuelsen, 1995). Up to now in the simulations the injection temperature of air, methanol vapour and methanol liquid was set to 20 °C. However, the temperature

7.5 mm downstream of the exit orifice, i.e. the injection position in the simulations, might be different from the injection temperature at the nozzle. Indeed, in the first simulations (Figure 5.15) because the droplets vaporize the temperature of the gas phase drops from 20 °C down to 5 °C within the first 7 mm downstream of the exit orifice. The assumption consists in injecting the droplets and the methanol vapour at a temperature of 12 °C instead of 20 °C. The air is still injected at a temperature of 20 °C. The results are shown on Figure 5.16. The results are clearly improved. The predictions still under-estimate the experimental data but now the maximum difference 150 mm downstream is 17 % instead of 35 % in the first round of simulations. The predictions could be further improved by considering the actual measurements of droplets size distribution. The experimental profiles of *SMD* and arithmetic mean droplet diameters show that the smallest droplets are found on the centreline axis of the spray whereas the largest drops are on the edges of the spray. The smallest droplets vaporizing faster than the largest droplets, the results could be improved by varying the size distribution of the droplets over the source area. One may also question the absence of secondary break-up models which could account for the break-up of the largest droplets. Gant et al. (2007) have simulated the experiments of McDonell *et al.* with the CFD code CFX and did not observe any changes in the results when using secondary break-up models. Figure 5.17 shows the mass fraction of droplets for two simulations, one with the size distribution $D10$ and one with the size distribution $D32$. It is seen that due to their lower inertia the droplets with the size distribution $D10$ disperse more than the droplets with the size distribution $D32$.

5.6 Conclusions

The Euler-Lagrange model which was implemented in the FLACS model has been presented. Heavy particles do not follow the trajectory of fluid particles. A proper model needs to be employed in order to estimate the instantaneous fluid velocity seen by the heavy particles. The modified Langevin equation derived by Minier and Peirano (2001) was implemented in the FLACS model. Appropriate second order numerical schemes are used to solve the system of Stochastic Differential Equations. Due to its balance between computational costs and accuracy the infinite liquid conductivity model (Abramzon and Sirignano, 1989) is used to compute the vaporization of the liquid droplets. Numerical parcels containing a given number of physical particles are tracked in the computational domain. The particles within a parcel have the same properties: same velocity, diameter, temperature.

Three laboratory scale experiments have been simulated in order to validate the implementation of the Euler-Lagrange models. The experiments of Hardalupas et al. (1989); McDonell and Samuelsen (1995); Sheen et al. (1994) were considered. Very encouraging results were obtained for the experiments of Hardalupas et al. (1989) and Sheen et al. (1994). The models were able to capture the inertia and two-way coupling effects. Very satisfying results were also seen for the spray experiments of McDonell and Samuelsen (1995). The initial conditions of the Mcdonell *et al.* experiments are more complex than the ones of the Hardalupas *et al.* and Sheen *et al.* experiments. The initial temperature of the spray, which is an unknown initial parameter, was shown to have a non-negligible influence on the results. It illustrates the difficulties in specifying

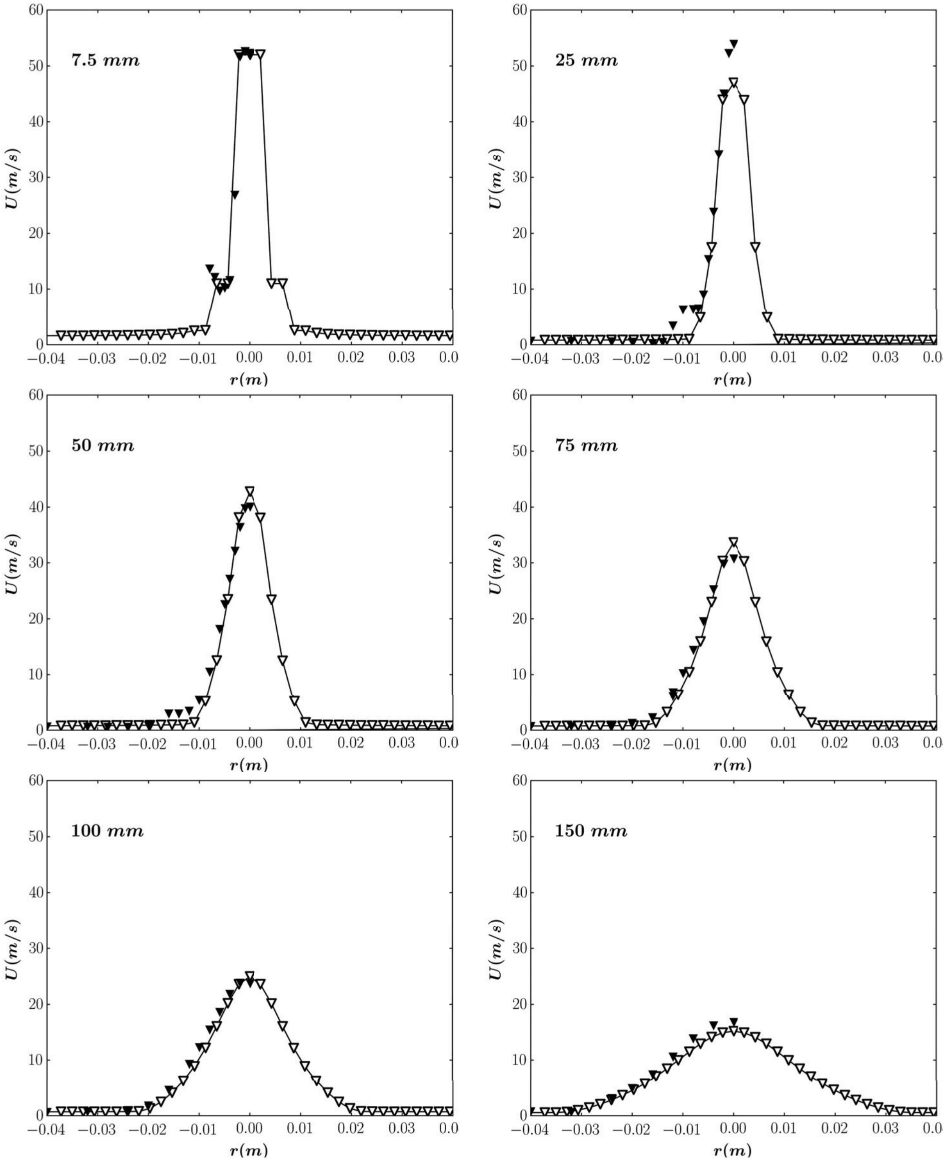

Figure 5.14: *Simulation of the experiment of McDonell and Samuelsen (1995). Radial profiles of mean axial velocity. Black symbols represent experimental data and white symbols numerical results.*

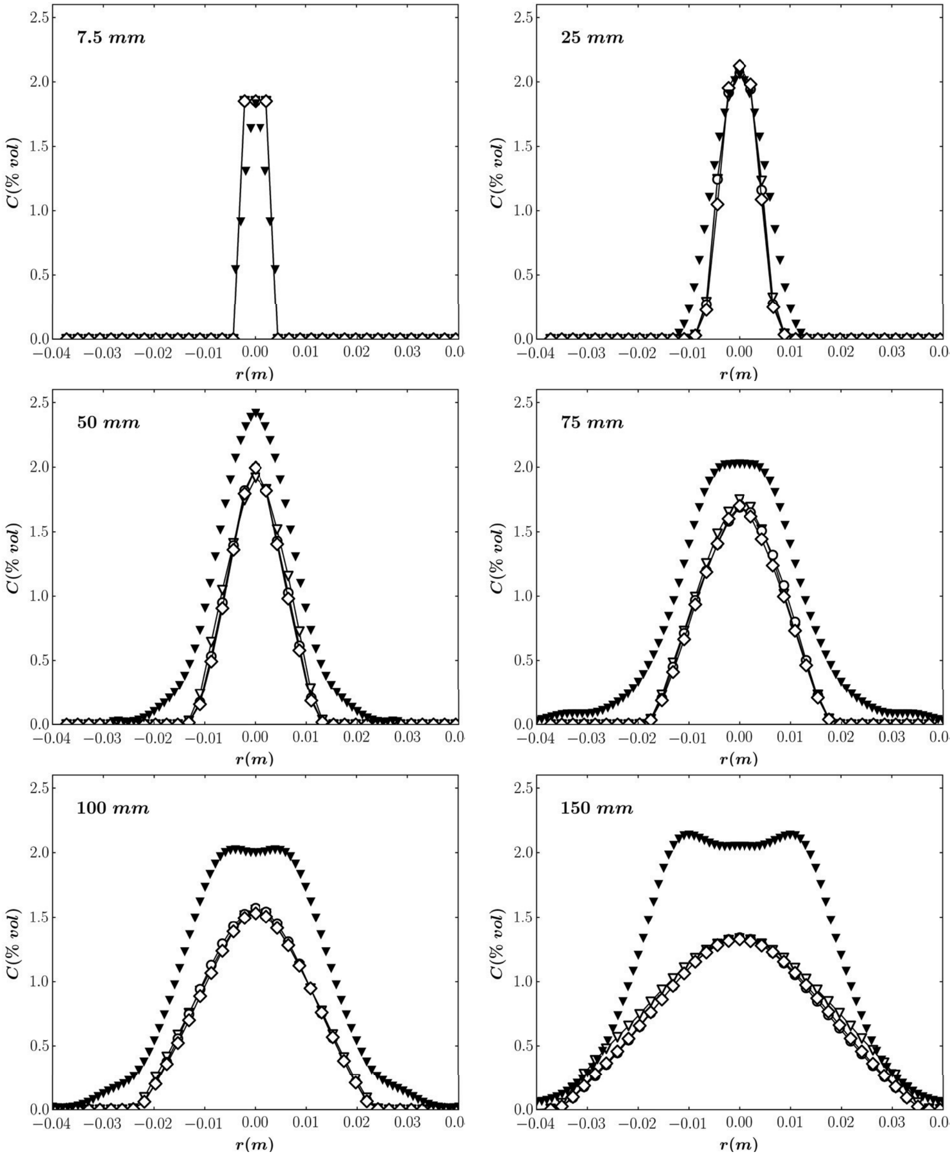

Figure 5.15: *Simulation of the experiment of McDonell and Samuelsen (1995). Radial profiles of mean methanol concentration. Black symbols represent experimental data and white symbols numerical results. (∇) represents simulation with the uniform size distribution with diameter $D10 = 19.3\,\mu m$. ($\bigcirc$) represents simulation with the uniform size distribution with diameter $D32 = 32\,\mu m$. ($\diamondsuit$) represents simulation with the log-normal distribution with $SMD = 32\,\mu m$. The temperature at the injection plane is 20 °C.*

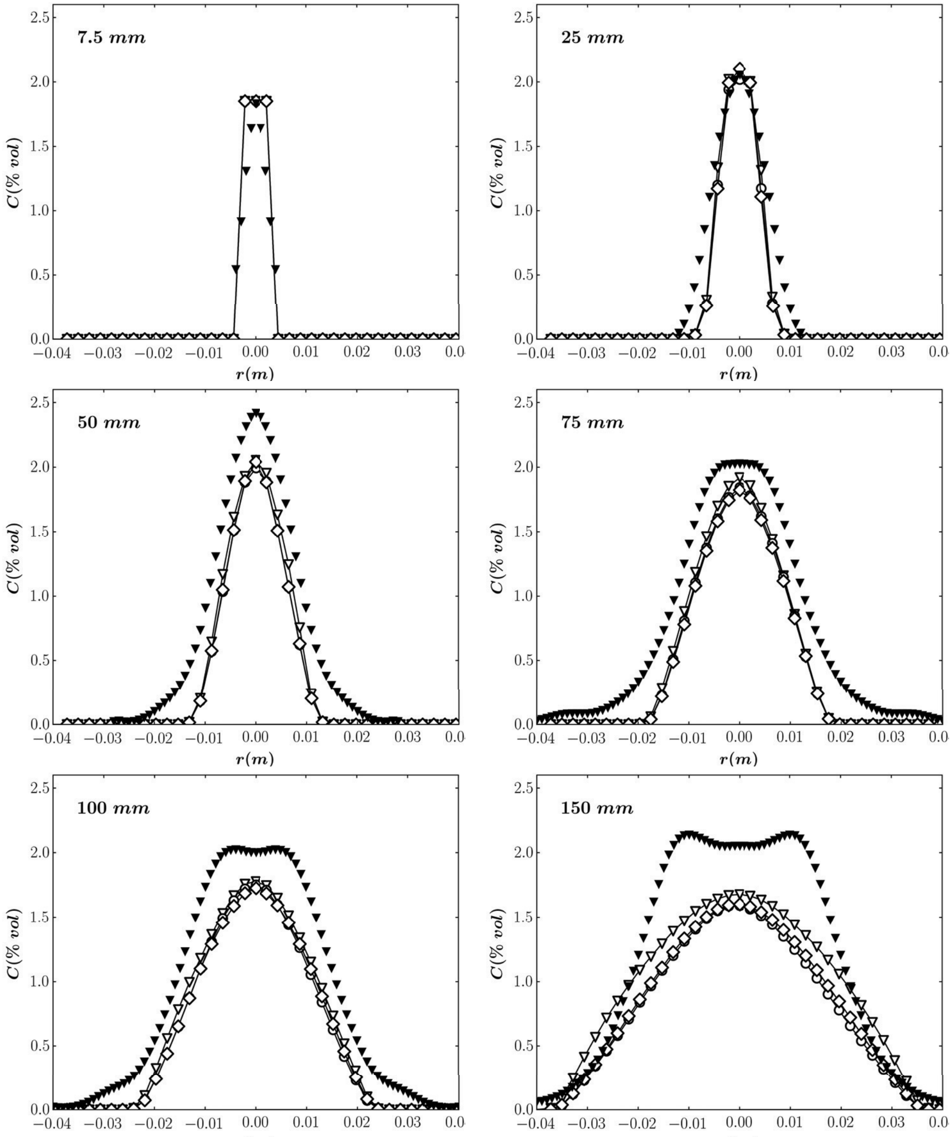

Figure 5.16: *Simulation of the experiment of McDonell and Samuelsen (1995). Radial profiles of mean methanol concentration. Black symbols represent experimental data and white symbols numerical results. (∇) represents simulation with the uniform size distribution with diameter* $D10 = 19.3\,\mu m$*. (◯) represents simulation with the uniform size distribution with diameter* $D32 = 32\,\mu m$*. (◇) represents simulation with the log-normal distribution with* $SMD = 32\,\mu m$*. The temperature at the injection plane is 12* °C.

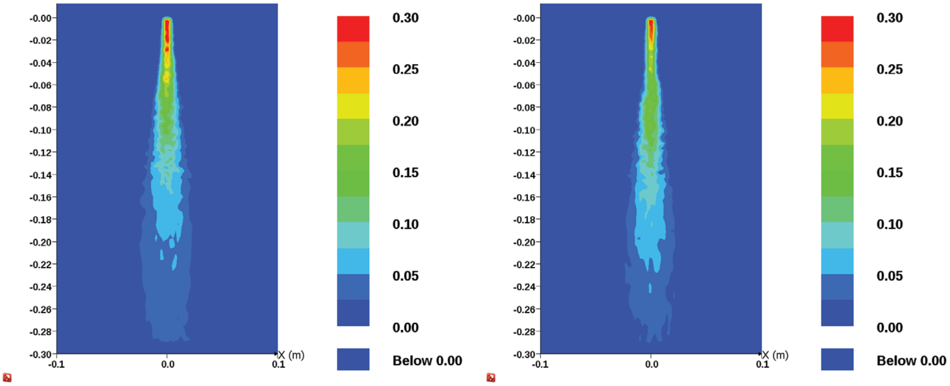

Figure 5.17: *2D cut planes of the mass fraction of droplets in the experiments of McDonell and Samuelsen (1995).* ***Left plot**: Simulations with the uniform size distribution with diameter* $D10 = 19.3\,\mu m$*.* ***Right plot**: simulation with the uniform size distribution with diameter* $D32 = 32\,\mu m$*.*

the source conditions of complex scenarios. In the next chapter a simplified model which requires less information about the source conditions is presented.

Chapter 6

Two-phase turbulent jet flows: the HEM approach

6.1 Description of the HEM approach

6.1.1 Overview

The Homogeneous Equilibrium Model (HEM) is a simplified approach for modelling two-phase flows where it is assumed that both phases are in local thermal and kinematic equilibrium. It implies that the transport of heat and mass between the phases is infinitely fast. This approach only distinguishes the two phases by their volume (or mass) fractions in a given mixed volume. The temperature, velocity and other flow field parameters are the same for the two phases and the denomination mixture temperature or mixture velocity is often encountered. The HEM approach has two main advantages:

- It requires little information about the source term.
- The conservation equations are similar to single phase flow conservation equations.

By *little information* about the source term it is meant that information about the particle diameter and velocity is not required. The particle volume fraction is the only parameter needed to characterize the dispersed phase at the source. This can be seen as an advantage because a lot of uncertainties remain in estimating the characteristics of particles produced by the atomization of liquid sprays (despite some recent efforts, see for example Witlox *et al.*, 2010, Bonnet *et al.* 2005). The second bullet implies that minor modifications to single phase flow CFD codes (such as FLACS) are needed. These modifications are detailed in the next section.

The main disadvantage of the HEM approach is the equilibrium assumption implying infinitely fast transfer of heat and mass, which seems to fail for large particle diameters. Kukkonen et al. (1994) used the HEM approach to compute the dispersion of two-phase ammonia jets and they assessed the performances of the HEM approach by comparing the results with a more advanced two-phase flow model (the model was based on Lagrangian particle tracking). They found that the results were identical (within 1%) when the ammonia droplets had a diameter smaller than 100 microns. Faeth (1983) provides a thorough theoretical description of the HEM approach and reports comparisons between HEM predictions and experiments for evaporating and combusting sprays. As Kukkonen et al. (1994), Faeth (1983) also concludes that the finite inter-phase transport rates account for much of the differences between the HEM approach and experimental observations.

6.1.2 Implementation inside the FLACS code

Some details about the implementation of the HEM method inside the FLACS CFD model are now discussed. In each grid cell the calculations must provide the mass fractions of air, contaminant in the gas phase and contaminant in the liquid phase. The mass fractions are related to the mixture fraction and the initial mass fractions via the following equation:

$$Y_i = Y_{i_0}^a + f_g Y_{i_0}^g + f_l Y_{i_0}^l \tag{6.1}$$

$$\sum_i Y_i = 1 \tag{6.2}$$

where Y_i is the mass fraction of element i at a given location $\mathbf{x}$. In this work we are dealing with releases of pressurized liquefied gases into the atmosphere and therefore the elements present are: oxygen, nitrogen, the released chemical in the vapour phase and the released chemical in the liquid phase. In Equation (6.1), $Y_{i_0}^a$ is the initial mass fraction of element i inside the surrounding atmosphere, $Y_{i_0}^g$ is the initial mass fraction of element i inside the gas phase at the source, and $Y_{i_0}^l$ is the initial mass fraction of element i inside the liquid phase at the source. Transport equations are solved for the two mixture fractionsf_g andf_l (the index $*$ represents g or l):

$$\frac{\partial(\beta_v \rho f_*)}{\partial t} + \frac{\partial(\beta_j \rho u_j f_*)}{\partial x_j} = \frac{\partial}{\partial x_j}\left(\beta_j \frac{\mu_{eff}}{\sigma_{f_*}} \frac{\partial f_*}{\partial x_j}\right) + \beta_v S_{f_*} \tag{6.3}$$

The mixture fraction $f_*(x_j,t)$ indicates how much of the quantity $Y_{i_0}^*$ has been transported to the location x_j at time t. The source term S_{f_*} contains the effects of the evaporation and eventual deposition on the ground of the liquid phase. And a source term $S_{H,HEM}$ is added to the right hand side of the transport equation for the enthalpy and represents the loss of energy due to liquid deposition. The density of the mixture is given by:

$$\rho = \sum_i \rho_i \alpha_i \tag{6.4}$$

where α_i is the volume fraction of element i at the position x_j and time t. Evaporation of the liquid phase is taken into account by ensuring thermodynamic equilibrium in each grid cell. Thermodynamic equilibrium implies that the partial pressure of the contaminant in the vapour phase is the saturation pressure at the mixture temperature. The partial pressure of the chemical vapour is deduced from the Dalton's law:

$$P_g = \alpha_g P_{atm} = P_{sat}(T) \tag{6.5}$$

And α_g is the volume fraction of the chemical vapour. We iterate on the temperature until equilibrium is attained. Equilibrium is attained when the enthalpy is equal to the initial enthalpy in the control volume.

6.2 Simulation of the McDonell *et al.* experiments

Setup of the simulations

The McDonell and Samuelsen (1995) experiments that were simulated with the Euler-Lagrange models in Chapter 5 are now computed with the HEM approach. The measurements at the location 7.5 mm downstream of the exit orifice are used as inlet conditions. The size of the droplets is not required as input of the HEM approach. The volume fraction (or mass fraction) is the only parameter needed to describe the dispersed phase. It is important to note that at the inlet plane we have a mixture of air, methanol vapour and methanol liquid. In terms of mass fractions we have:

$$Y_a + Y_{m,v} + Y_{m,l} = 1 \tag{6.6}$$

If we consider the mixture methanol alone we can also write:

$$Y'_{m,v} + Y'_{m,l} = 1 \tag{6.7}$$

and we already know $Y'_{m,v}$ from the following equation:

$$\dot{m}_{gas,@7.5mm} = Y'_{m,v}\dot{m}_{total} \tag{6.8}$$

Another equation can be written for $Y'_{m,v}$:

$$Y'_{m,v} = \frac{Y_{m,v}}{Y_{m,v} + Y_{m,l}} \tag{6.9}$$

Therefore, we can find the mass fraction of liquid methanol in the mixture composed of air, methanol vapour and methanol liquid:

$$Y_{m,l} = \frac{Y_{m,v}\left(1 - Y'_{m,v}\right)}{Y'_{m,v}} \tag{6.10}$$

where $Y_{m,v}$ is given by the measurement of methanol vapour concentration at the plane 7.5 mm downstream of the exit orifice. The mass fraction of air is finally estimated from Equation (6.6). The computational grid used in the Euler-Lagrange computations is also used in these computations.

Results and discussions

Figure 6.1 shows the results for the mean velocity field. As for the Euler-Lagrange computations the velocity results compare well with experimental data. It is not the case for the concentration field shown on Figure 6.2. As expected the predictions of the HEM approach largely exceed the experimental observations. This is a direct consequence of the infinite inter-phase transport rates. Moreover, methanol is not a volatile liquid since its normal boiling point is above typical ambient atmospheric temperatures and then the assumption of infinite inter-phase transfer rates might be inappropriate. We will test further the HEM approach with volatile liquids in the next chapter.

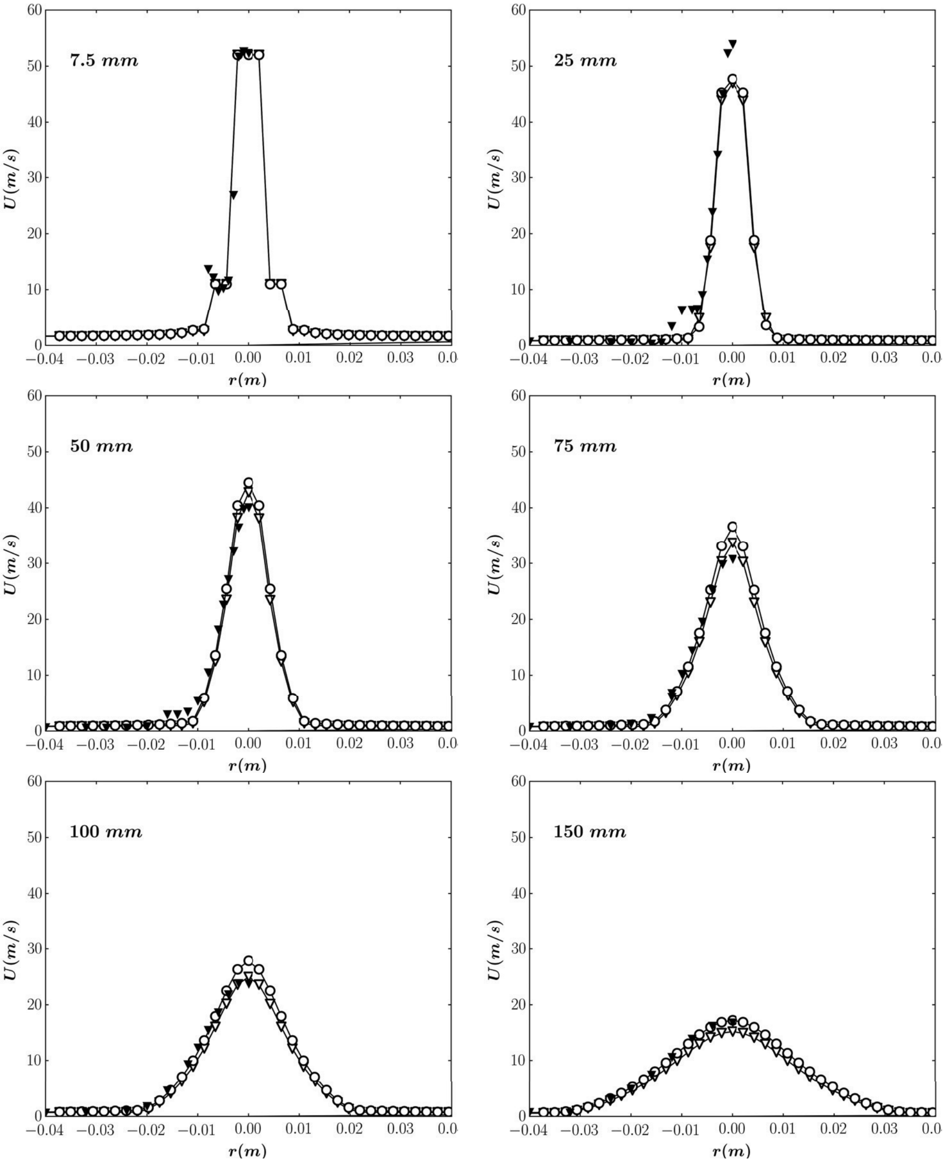

Figure 6.1: *Simulation of the experiment of McDonell and Samuelsen (1995). Radial profiles of mean axial velocity. Black symbols represent experimental data and white symbols numerical results. (◯) represents the HEM predictions and (∇) represents the Euler-Lagrange predictions.*

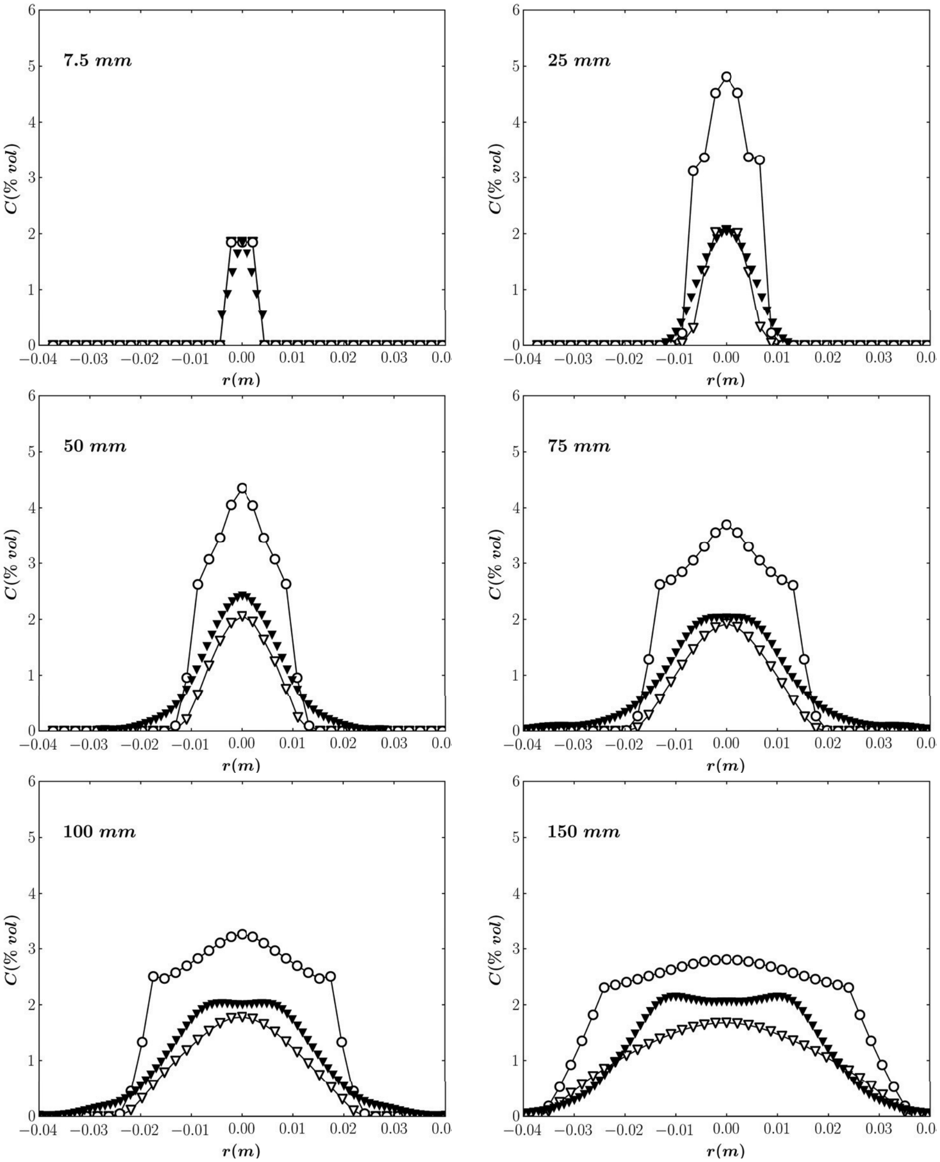

Figure 6.2: *Simulation of the experiment of McDonell and Samuelsen (1995). Radial profiles of mean methanol concentration. Black symbols represent experimental data and white symbols numerical results. (◯) represents the HEM predictions and (∇) represents the Euler-Lagrange predictions.*

6.3 Estimation of liquid deposition in the HEM approach

6.3.1 Proposition of a model

A model to estimate the amount of liquid that deposits on the ground is proposed. In the HEM approach, rain-out is due to jet impingement either directly on the ground or on obstacles. Coupling a rain-out model with the HEM approach is not an easy task as information about the diameter of liquid droplets and the size distribution is voluntarily omitted. Consider a jet impinging on an obstacle located at a distance L in the positive x direction. In a grid cell (I,J,K) which is directly adjacent to the obstacle, the amount of liquid that rains-out at each time step is estimated via the following relation:

$$m_{RO}(\mathbf{x}) = \begin{cases} \sum\limits_{i,k} Y^{l}_{i,k} m_k & \text{if } T(\mathbf{x}) \leq T_{NBP} \\ \\ 0 & \text{if } T(\mathbf{x}) > T_{NBP} \end{cases} \tag{6.11}$$

where

$$\mathbf{x} = [x(I), y(J), z(K)] \tag{6.12}$$

Rain-out is activated only if the temperature of the mixture inside the grid cell (I,J,K) is less than or equal to the normal boiling point of the mixture. Mixture temperatures which are smaller than or equal to the normal boiling point of the mixture indicate that liquid is evaporating and that thermodynamic equilibrium has been reached. We define a characteristic length scale ℓ_{RO} for the rain-out process defined as the product of the characteristic velocity and characteristic time scales for the rain-out process:

$$\ell_{RO} = \vartheta_{RO} \tau_{RO} \tag{6.13}$$

The sum on the index k in Equation (6.11) is performed over all grid cells located at a distance less or equal than ℓ_{RO} from the wall. The velocity ϑ_{RO} is expressed by:

$$\begin{aligned} \vartheta_{RO} &= \max\left[u(I,J,K), u(I-1,J,K), \ldots, u(I-r,J,K)\right] \\ & \quad \textit{and}\ \forall r,\ T(I-r,J,K) \leq T_{NBP} \end{aligned} \tag{6.14}$$

The characteristic velocity for the rain-out process (ϑ_{RO}) is taken to be the local maximum velocity in regions of the flow where liquid is evaporating and thermodynamic equilibrium has been attained. This can be justified by the fact that the mass of liquid that deposits on the ground or on obstacles is expected to be contained inside the droplets having the largest diameters. These droplets have a large inertia, way larger than the inertia of fluid particles, and hence have an extended memory of their maximum velocities. Finally, the characteristic time τ_{RO} over which the rain-out process occurs is assumed to be the time needed by the flow to achieve a new thermodynamic equilibrium in the grid cell (I,J,K) adjacent to the wall. This time-scale is approximated by the time needed by the flow to bring new fluid particles to this grid cell. The time-scale is calculated as the ratio of the size of the grid cell and the velocity across the face of the grid cell. Appropriate source terms are integrated inside the transport equations for the mixture fractions and mixture enthalpy. The amount of liquid that is removed from the flow is added as a source term to the pool model.

6.3.2 Spread and vaporization of liquid on the ground

Presentation of the model

In the case of liquid depositing on the ground and forming a pool the two-dimensional (2D) shallow water equations are solved to calculate the behaviour of the pool (Melheim et al., 2008). The assumption behind the shallow water theory is that the pool properties (temperature, velocity, etc.) are uniform across the thickness of the pool and, thus, are only a function of the horizontal coordinates. Therefore, the shallow water equations are an approximation of the equations of fluid motion, which is accurate when the thickness of the liquid pool is small in comparison with its horizontal dimensions. The advantage of using the 2D shallow water equations to calculate the pool spread and vaporization is that they account for the effect of terrain features (e.g., sloping, channels, etc.) or obstacles on the spread of the pool.

The shallow water equations for the conservation of mass and momentum are:

$$\frac{\partial h}{\partial t}+\frac{\partial h u_i}{\partial x_i} = \frac{\dot{m}_L-\dot{m}_V}{\rho_l} \tag{6.15}$$

$$\frac{\partial u_i}{\partial t}+u_j\frac{\partial u_i}{\partial x_j} = F_{g,i}+F_{\tau,i} \tag{6.16}$$

where $\dot{m}_L$ is the liquid spill rate into the pool and $\dot{m}_V$ is the rate of vaporization, and the terms on the right-hand side of the momentum equation represent the gravity and shear stress components, respectively:

$$F_{g,i} = g\Delta\frac{\partial\left(h+z\right)}{\partial x_i} \tag{6.17}$$

$$F_{\tau,i} = \frac{1}{8}f_f u_i\left|\mathbf{u}\right| \tag{6.18}$$

where $\Delta = 1$ for pools spreading on solid surfaces and $\Delta = \left(1-\rho_l/\rho_w\right)$ for spills on water, and f_f is the friction coefficient between pool and substrate. The rate of vaporization from the pool ($\dot{m}_V$) includes contributions from heat transfer from the substrate (e.g., ground or water), solar radiation and convective heat transfer from the air above the pool (Hansen et al., 2007; Melheim et al., 2008).

The heat transfer components are added into the energy equation, which is solved in terms of specific enthalpy:

$$\frac{\partial\theta}{\partial t}+u_i\frac{\partial\theta}{\partial x_i}=\frac{\dot{m}_L}{h}\left(\theta_L-\theta\right)+\dot{q}_c+\dot{q}_{rad}+\dot{q}_g+\dot{q}_{evap} \tag{6.19}$$

where $\dot{q}_c$ is convective heat transfer, $\dot{q}_{rad}$ is heat transfer to the pool from radiation, $\dot{q}_g$ is heat transfer to the pool from the substrate, and $\dot{q}_{evap}$ is heat loss due to evaporation. For cryogenic pools, heat transfer from the substrate is often the main source of heat input. The heat transfer from a solid substrate (e.g., ground) is calculated as a function of position and time according to the semi-infinite solid heat transfer theory, assuming perfect contact between pool and substrate. The 2D shallow water equations are solved at every time step and on the same computational domain as the atmospheric flow. This allows the heat transfer from the ambient to be accounted for in a realistic and time-dependent manner. Hansen et al. (2010a) have used this model to compute atmospheric releases of Liquefied Natural Gas (LNG). The Burro (Koopman et al., 1982a,b) and Coyote (Goldwire et al., 1983) experiments were simulated and the FLACS predictions were found to compare well with experimental data. Middha et al. (2011) have also used the FLACS pool model to simulate liquid hydrogen releases and obtained very satisfying results (see Paper 2 in this thesis).

Model improvement

Improvements to the pool model have been implemented as part of the work done in this thesis. The equations controlling the spread and vaporization of liquids on the ground are discretized on the grid used to solve the surrounding flow field. We refer to this grid as to the *FLACS-MASTER* grid in the following. For large scale dispersion scenarios, the *FLACS-MASTER* grid can be rather coarse and not uniform due to grid refinement around leaks. However, it is preferable to discretize the shallow water equations on a uniform grid with a reasonably fine resolution. The main reason being that the computation of the spread of a liquid on a ground involves numerical challenges associated with front propagation, i.e. the interface between the wet and dry parts of the computational domain. In order to avoid numerical instabilities, the equations for liquid spread and liquid vaporization are solved on a uniform grid with a user defined resolution. This grid is referred to as the *FLACS-POOL* grid. Communication is established between the *FLACS-MASTER* grid and the *FLACS-POOL* grid. Flow variables such as the mean air flow velocity or the mean air temperature that are needed inside the equations for liquid spread and vaporization are interpolated from the *FLACS-MASTER* grid to the *FLACS-POOL* grid. The amount of vapour emanating from the pool and the associated enthalpy are computed in each grid cell of the *FLACS-POOL* grid and are interpolated to the *FLACS-MASTER* grid.

A simple test case has been run in order to validate the implementation of the algorithm. A methane liquid release of 88 kg/s on a flat ground is considered. First the liquid release is solved on the *FLACS-MASTER* grid with a resolution of 1 m and then the same liquid release is computed using the *FLACS-POOL* grid with the same resolution than the *FLACS-MASTER* grid. Figure 6.3 shows the evaporation fluxes from the liquid pool as a function of time. The two computations give the same results as expected. The same release is solved on three others *FLACS-POOL* grids with resolutions: 0.5, 0.25 and 0.125 m Figure 6.3 shows the evaporation fluxes from the liquid pool as a function of time. We note that the results converge toward the same curve with decreasing cell size.

Figure 6.4 shows the liquid depth of a pool formed by rain-out of some of the liquid of a two-phase flashing jet of ammonia. The set-up of this hypothetical test is similar to the set-up of the Desert Tortoise tests which will be discussed in the next chapter. The grid is also shown and it is clear that the resolution is not optimal to solve the spread of a thin layer of liquid on the ground. The grid is also far from uniform due to the required refinement at the leak position. The *FLACS-POOL* grid was used with a uniform resolution of 30 cm and allows getting plausible results for the spread of the liquid.

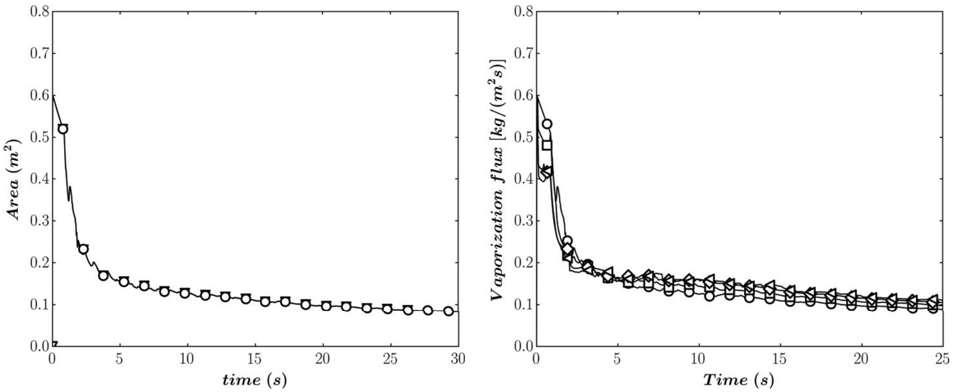

Figure 6.3: *The evaporation flux from a liquid pool.* ***Left****, (◯) is the* $FLACS-MASTER$ *grid and (∇) represents the* $FLACS-POOL$ *grid and the same resolution is used for both grids.* ***Right****, simulations with the* $FLACS-POOL$ *grid: (◯) resolution is 1 m, (□) resolution is 0.5 m, (◁) resolution is 0.25 m and (◇) resolution is 0.125 m.*

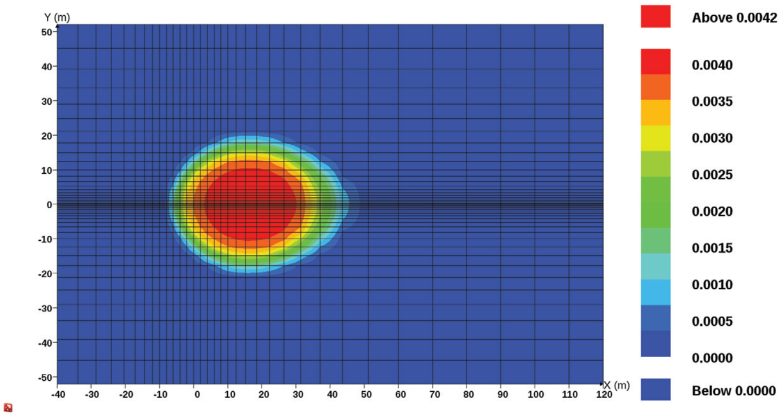

Figure 6.4: *2D cut plane of the liquid depth of a pool formed by rain-out. The FLACS-MASTER grid is shown and is highly non-uniform with a coarse resolution. The* $FLACS-POOL$ *grid helps improving the results.*

6.4 Conclusions

The homogeneous equilibrium model (HEM) was implemented inside the FLACS model. The HEM approach assumes that both phases are in local thermal and kinematic equilibrium. The dispersed phase is fully characterised by its volume fraction at the source. The experiments of McDonell and Samuelsen (1995) were simulated with the HEM approach. The predictions largely over-estimate the experimental observations. The over-prediction is due to the assumption of infinitely fast transport rates between the phases which fails for non-volatile liquids, i.e. liquids whose normal boiling point is larger than ambient temperature. A model used to estimate the amount of liquid that deposits on the ground has been proposed. The model is validated against large-scale experiments in the next chapter. Improvements to the FLACS model for liquid spreading and evaporation on grounds have also been presented. The improvements consist in solving the equations of the pool model on a uniform grid which is created in addition to the grid for the surrounding flow field. This new feature for the pool model is used in the simulations of the large scale experiments which will be discussed in the next chapter.

Chapter 7

Simulations of atmospheric releases of pressurized liquefied gases

7.1 The atmospheric boundary layer

7.1.1 Introduction to atmospheric turbulence

A boundary layer is a layer of fluid in the immediate vicinity of a material surface in which exchanges of mass, momentum and heat take place between the surface and the fluid (Arya, 2001). The atmospheric boundary layer can be loosely seen as the first kilometre of the troposphere. It has an important influence on the behaviour of the atmosphere as a whole, and activities involving the representation of the atmosphere such as climate modelling and numerical weather prediction cannot succeed without the boundary layer being represented in some detail. Indeed, the transfers of heat, mass and momentum from the ground to the free atmosphere occurs through the atmospheric boundary layer. In the framework of this thesis, an accurate description of the atmospheric boundary layer is crucial for predicting the dispersion of pollutants or other materials. A schematic of the atmospheric boundary layer is shown on Figure 7.1. Accidental releases of pressurized liquefied gases usually occur in the lower part of the atmospheric boundary layer called the surface layer. The surface layer roughly

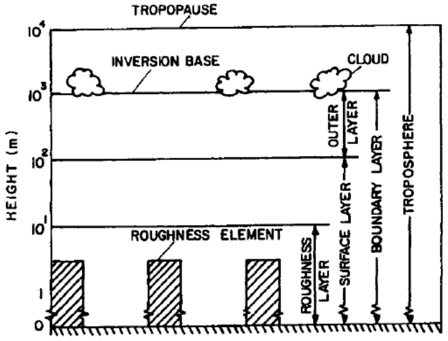

Figure 7.1: *A schematic of the Atmospheric Boundary Layer (taken from Arya (2001)).*

represents one-tenth of the atmospheric boundary layer. The surface layer is said to be stable, unstable or neutral. These adjectives refer to the response of a parcel of air when displaced in the vertical direction. The stability criteria can be expressed via the temperature gradient in the surface layer:

$$\begin{cases} \text{Unstable if} & (\partial T)/(\partial z) < \gamma \\ \text{Neutral if} & (\partial T)/(\partial z) = \gamma \\ \text{Stable if} & (\partial T)/(\partial z) > \gamma \end{cases} \tag{7.1}$$

where $\gamma = -(0.98\,C)/(100\,m)$ is the lapse rate. The lapse rate is obtained by considering the vertical displacement of a parcel of dry air without heat exchange with its surrounding (Hanna et al., 1982). The Monin-Obukhov length is often employed to measure the stability of the surface layer. Different methods can be used to derive the Monin-Obukhov length. One method consists in multiplying the budget equation of turbulent kinetic energy by $-(\kappa z)/u_*^3$. One of the dimensionless terms, noted β can be written as (Stull, 1988):

$$\beta = \frac{z}{L} = -\frac{z\kappa g\left(\overline{w'T'}\right)_s}{u_*^3 T} \tag{7.2}$$

The Monin-Obukhov length is noted L, $\left(\overline{w'T'}\right)_s$ is the turbulent flux of heat at the surface and $u_* = \left[\left(\overline{u'w'}\right)_s^2 + \left(\overline{v'w'}\right)_s^2\right]^{0.25}$ is the momentum flux at the surface also called the friction velocity. The absolute value of the Monin-Obukhov length can be interpreted as a measure of the height above the ground where buoyancy production of turbulent kinetic energy first dominate over mechanical shear production of turbulent kinetic energy (Stull, 1988). We note that L has the opposite sign of the turbulent heat flux at the ground. If L is positive it means that there exists a downward heat flux from the atmosphere toward the ground. This situation corresponds to a stable stratification of the surface layer. If L is negative it means that there exists an upward

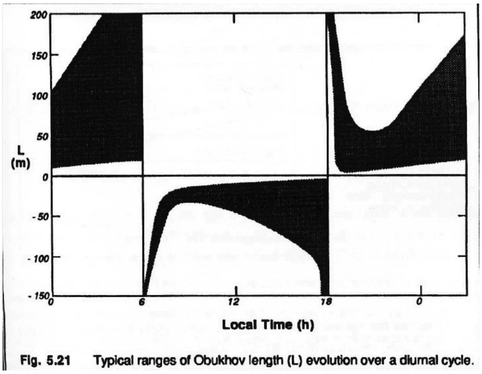

Figure 7.2: *Diurnal variation of the Monin-Obukhov length (taken from Stull (1988)).*

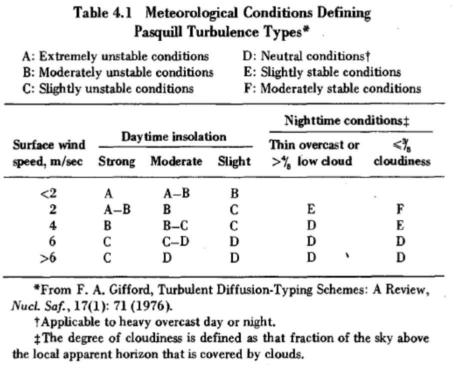

Table 4.1 Meteorological Conditions Defining Pasquill Turbulence Types*

A: Extremely unstable conditions
B: Moderately unstable conditions
C: Slightly unstable conditions
D: Neutral conditions†
E: Slightly stable conditions
F: Moderately stable conditions

Surface wind speed, m/sec	Daytime insolation			Nighttime conditions‡	
	Strong	Moderate	Slight	Thin overcast or $>\frac{4}{8}$ low cloud	$\leq\frac{3}{8}$ cloudiness
<2	A	A–B	B		
2	A–B	B	C	E	F
4	B	B–C	C	D	E
6	C	C–D	D	D	D
>6	C	D	D	D	D

*From F. A. Gifford, Turbulent Diffusion-Typing Schemes: A Review, *Nucl. Saf.*, 17(1): 71 (1976).

†Applicable to heavy overcast day or night.

‡The degree of cloudiness is defined as that fraction of the sky above the local apparent horizon that is covered by clouds.

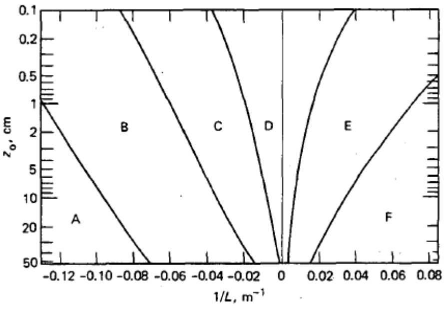

Figure 7.3: *The table established by Pasquill (1961) containing the six stability classes and the graph of Golder (1972) linking the Pasquill classes to the Monin-Obukhov length via the roughness length.*

heat flux from the ground toward the atmosphere and the surface layer has an unstable stratification. Figure 7.2 illustrates the diurnal variation of the Monin-Obukhov length. It is worth pointing out the importance of the stability of the surface layer in the dispersion of pollutants or chemicals in the atmosphere. When the surface layer has a stable stratification, turbulent fluctuations are dampened, killed, and turbulent mixing is weak. Therefore, high chemical concentrations are observed over distances larger than in the case of an unstable surface layer.

In most atmospheric dispersion models the stability of the surface layer is described via a Pasquill-Gifford stability class. Figure 7.3 shows the table created by Pasquill (1961) which contains the six different classes that were identified and their corresponding criteria. The stability classes A through C represents unstable conditions, from E to F stable conditions and class D is associated with neutral conditions. The scheme established by Pasquill essentially describes the state of the surface layer, it does not allow to model it. It would be useful to associate a state of the surface layer, i.e. a Pasquill class, with a value of the Monin-Obukhov length which is a direct measure of the stability. Golder (1972) performed this work. He analysed turbulent measurements in the surface layer to determine a graphical relation between the roughness length, the Pasquill class and the Monin-Obukhov length. The graphical relationship is shown on Figure 7.3.

7.1.2 Modelling of atmospheric turbulence in the FLACS model

For atmospheric dispersion simulations, the atmospheric boundary layer is modelled by imposing profiles for velocity, temperature and turbulence on flow inlet boundaries. These profiles are specified as a function of the atmospheric stability (expressed according to the Pasquill-Gifford stability classes) and the surface roughness length, z_0. Logarithmic velocity profiles are written as (van den Bosch and Weterings, 1997):

$$U(z) = \frac{u_*}{\kappa}\left(\ln\left(\frac{z}{z_0}\right) - \psi_m\right) \tag{7.3}$$

where the friction velocity u_* is given by:

$$u_* = \frac{U_{ref}\kappa}{\ln\left(\frac{z_{ref}}{z_0}\right) - \psi_m} \tag{7.4}$$

where U_{ref} is the velocity at the reference height z_{ref}. The stability function ψ_m is also given by van den Bosch and Weterings (1997) as:

$$\psi_m = \begin{cases} 2\ln\left(\frac{1+\xi}{2}\right) + \ln\left(\frac{1+\xi^2}{2}\right) - 2\arctan(\xi) + \frac{\pi}{2} & \text{if } L \leq 0, \\ \\ -17\left(1 - \exp\left(-0.29\frac{z}{L}\right)\right) & \text{if } L > 0. \end{cases} \tag{7.5}$$

and

$$\xi = \left(1 - 16\frac{z}{L}\right)^{1/4} \tag{7.6}$$

The temperature profile is assumed to be uniform. The expressions for the turbulent kinetic energy, k, and turbulent dissipation rate, ε, for neutral and stable atmospheric boundary layers follow the derivation by Han et al. (2000):

$$k(z) = \begin{cases} 6u_*^2 & \text{if } z \leq 0.1h_{abl}, \\ \\ 6u_*^2\left(1 - \frac{z}{h_{abl}}\right)^{1.75} & \text{if } z > 0.1h_{abl} \end{cases} \tag{7.7}$$

and

$$\varepsilon(z) = \begin{cases} \frac{u_*^3}{\kappa z}\left(1.24 + 4.3\frac{z}{L}\right) & \text{if } z \leq 0.1h_{abl}, \\ \\ \frac{u_*^3}{\kappa z}\left(1.24 + 4.3\frac{z}{L}\right)\left(1 - 0.85zh_{abl}\right)^{1.5} & \text{if } z > 0.1h_{abl} \end{cases} \tag{7.8}$$

where h_{abl} is the height of the atmospheric boundary layer. For neutral or stable boundary layers, the boundary layer height is a function of the friction velocity, the Coriolis parameter f_c, and the Monin-Obukhov length L as follows:

$$h_{abl,neutral} = 0.3\frac{u_*}{f_c} \tag{7.9}$$

and

$$h_{abl,stable} = 0.4\left(\frac{u_* L}{f_c}\right)^{0.5} \tag{7.10}$$

The atmospheric dispersion model in FLACS has been tested against a wide range of scenarios including releases of dense, passive and buoyant gases in open, obstructed and enclosed spaces (Dharmavaram et al., 2005; Hansen et al., 2010a; Middha et al., 2009, 2011).

7.2 The CCPS experiments

The water tests

The CCPS experimental tests have been presented in Chapter 2 (Johnson and Woodward, 1999). For the water experiments, 19 tests are simulated. The computations are performed with both the HEM and the Euler-Lagrange approaches. The pseudo-source term is estimated via the control volume approach which was presented in Chapter 3. For the Euler-Lagrange approach the size distribution of the liquid droplets needs to be estimated. As recommended in the conclusion of Chapter 3 we use a log-normal distribution with standard deviation $\sigma_G = 1.8$ and the SMD is taken as the average of the three *SMD* obtained with the models presented in Chapter 3, Sections 3.2.2, 3.2.3 and 3.2.5. The final SMDs are plotted versus the degree of superheat for each one of the tests on Figure 7.4. As expected the SMD is decreasing with increasing degree of superheat. The tests conditions and the parameters of the pseudo-source are given in Table 7.1. The computational volume ranges from -5 m to 50 m in the x-direction, -10 m to 10 m in the y-direction and from 0 m to 10 m in the z-direction. The release is in the positive x-direction. The number of grid cells differs from one test to another, it varies between 300000 and 500000 cells. The time-step varies also from test to test but a typical or mean value for all tests is around $8.4\ 10^{-4}$ s. The number of parcel released at each time-step is set to 20. Two-way coupling is not activated The simulations are performed without wind because the experiments were conducted inside an open-house tunnel (Johnson and Woodward, 1999). The same set-up is used for the chlorine tests.

The results obtained with the HEM and Euler-Lagrange approaches are presented on Figure 7.5. Before discussing the results we mention that Bigot et al. (2005) have performed similar flashing water experiments. They measured the rain-out percentage and their data compare well with the CCPS data. Overall the predictions of the two methods are of reasonable accuracy. The results obtained with the Lagrange approach are more consistent with the experimental data. The HEM predictions have more variability or diversity. We note that the Euler-Lagrange predictions are above the experimental data which may indicate that the SMDs are slightly over-estimated or that the shape of the size distribution (log-normal with a given standard deviation) could be improved. We note that for super-heat degrees around 70 to 80 °C several experimental tests were performed. Different orifice diameters were used. The smallest orifice diameters gave the lowest amounts of rain-out.

The chlorine tests

Ten chlorine tests are simulated and the results are shown on Figure 7.5. Table 7.2 summarizes the experimental conditions and the parameters of the pseudo-source terms. Two sets of experimental data are considered: the corrected and the non-corrected measurements (Johnson and Woodward, 1999). The Euler-Lagrange approach over-estimates the amount of liquid which deposits on the ground whereas the HEM approach is not able to detect any rain-out. In the HEM approach all the liquid vaporizes before reaching the ground. In order to assess the impact of the shape of the log-normal distribution on the amount of liquid chlorine that deposits on the ground, test 2 was simulated with a log-normal distribution having a standard

Table 7.1: *Release conditions and parameters of the pseudo-source terms for the CCPS water tests.*

Test	Release conditions					Pseudo-source		
	D_{ori} (mm)	T_0 (K)	P_0 (bar)	$\dot{m}$ (kg/s)	T_a (K)	x_g (−)	U (m/s)	SMD (μm)
1	6.4	398.7	2.53	0.354	295.7	0.049	25	1420
2	6.4	410.2	3.47	0.420	300.0	0.070	32	780
3	6.4	421.0	4.60	0.488	300.9	0.090	39	529
4	6.4	433.2	6.33	0.568	297.9	0.112	48	354
5	6.4	443.4	8.07	0.658	296.5	0.130	56	274
6	6.4	454.4	10.62	0.797	299.3	0.151	65	212
7	6.4	465.7	13.61	0.901	300.0	0.171	74	168
8	6.4	476.4	16.98	0.995	297.9	0.191	84	141
10	3.2	454.3	10.47	0.184	297.3	0.150	65	215
11	3.2	465.9	13.53	0.213	301.0	0.172	75	174
12	3.2	476.3	17.14	0.241	300.9	0.191	85	149
13	3.2	488.2	21.40	0.267	305.4	0.267	96	128
21	3.2	455.1	11.98	0.210	308.7	0.152	68	200
25	12.7	433.1	6.31	2.408	303.2	0.112	48	347
26	12.7	443.8	8.16	2.750	308.7	0.131	55	258
27	12.7	455.3	10.62	3.111	309.8	0.152	65	197
30	3.2	399.0	2.53	0.099	308.2	0.049	25	1335
34	3.2	443.2	8.10	0.157	309.3	0.130	56	279
35	6.4	444.2	8.21	0.654	310.1	0.132	56	263

Table 7.2: *Release conditions and parameters of the pseudo-source terms for the CCPS chlorine tests.*

Test	Release conditions					Pseudo-source		
	D_{ori} (mm)	T_0 (K)	P_0 (bar)	$\dot{m}$ (kg/s)	T_a (K)	x_g (−)	U (m/s)	SMD (μm)
1	6.35	289.2	6.61	0.830	303.3	0.167	38	435
2	6.35	273.3	4.34	0.650	304.3	0.114	29	733
3	6.35	258.1	2.58	0.480	304.6	0.063	22	1527
4	6.35	247.1	1.79	0.380	304.3	0.027	14	3075
5	6.35	283.7	5.59	0.740	305.8	0.149	35	529
7	6.35	277.9	4.82	0.700	304.8	0.129	31	638
10	6.35	267.9	3.59	0.600	303.5	0.094	26	938
13	6.35	261.8	3.03	0.550	300.7	0.076	23	1133
16	6.35	250.9	2.15	0.440	301.2	0.039	17	2105
18	6.35	283.6	5.67	0.760	303.5	0.148	35	522
19	6.35	272.4	4.21	0.640	302.9	0.111	29	762

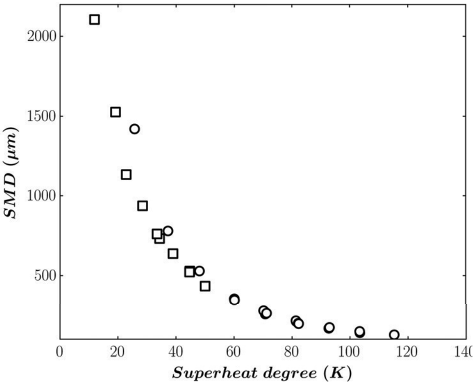

Figure 7.4: *Variation of the SMD as a function of superheat degree for the CCPS water and chlorine tests: (□) represents the chlorine tests and (◯) represents the water tests.*

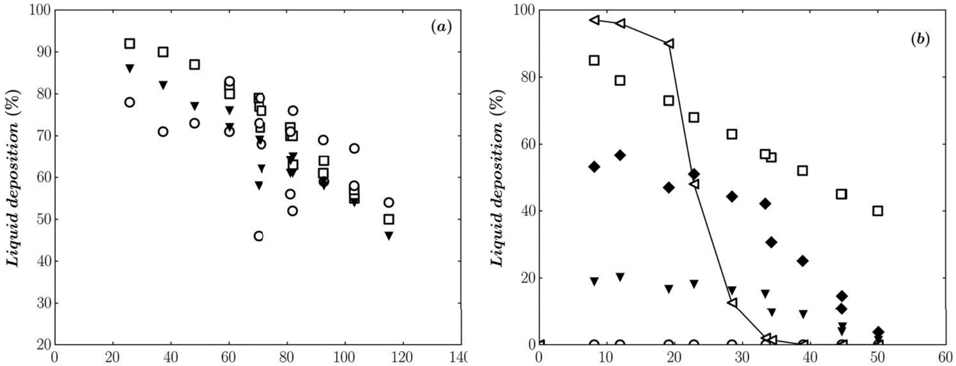

Figure 7.5: *Percentage of rain-out in the CCPS tests. The black symbols represent the experimental data.* ***(a)*** *water tests: (□) represents the Euler-Lagrange simulations and (◯) represents the HEM simulations.* ***(b)*** *chlorine tests: the corrected experimental data represented by black (◇) and the original experimental data are shown; (□) represents the Euler-Lagrange simulations, (◯) represents the HEM simulations and (◁) represents the results obtained with the flash program.*

deviation of $\sigma_G = 3.6$, i.e. twice the default standard deviation. The amount of rain-out went down from 56 % to 37 %, in good agreement with the experimental observation of 30.7 %. The results obtained with the utility program *flash* are also shown. The predictions of the utility program *flash* obey an on-off law, either 100 % of the liquid rains-out or none of the liquid rains-out.

7.3 The FLIE-INERIS experiments

The FLIE-INERIS tests have been presented in Chapter 2 (Bonnet et al., 2005). Free and impinging butane tests are simulated. Axial temperature profiles obtained wit the Euler-Lagrange and HEM approaches are compared with experimental data. Rain-out predictions due to jet impingement on a wall located at a given distance from the exit orifice are also compared with experimental observations.

Free butane jet

Butane is released through a 10 mm orifice diameter. The pressure inside the reservoir is 7.78 bar and the reservoir temperature is 19 °C. The mass flow rate which was measured during the experiment is 1.33 kg/s. The pseudo-source term is estimated via the control volume approach. The *SMD* needed in the Euler-Lagrange computations is taken as the mean of the three SMDs given by the models presented in Chapter 3, Sections 3.2.2, 3.2.3 and 3.2.5. The size distribution is a log-normal distribution with a standard deviation of $\sigma_G = 1.8$. The parameters of the pseudo-source term are summarized in Table 7.3. The temperature of the jet was measured along the centreline axis of the jet. The simulation domain goes from -10 m to 30 m in the x-direction, from -10 m to 10 m in the y-direction and from 0 m to 10 m in the z-direction. the total number of cells is 200000 and the resolution is 4.6 cm in the y and z directions and 10 cm in the x-direction in the near field of the jet. The time-step is set to $6.66\ 10^{-4}$ s and the number of parcels released at each time-step is 40. Two-way coupling is not activated. The stability of the atmosphere was not reported in the report describing the experimental tests. A neutral atmosphere is assumed with a wind speed of 3.5 m/s at 2 m and a wind direction aligned with the direction of the release.

The results are shown on Figure 7.6. The minimum temperature predicted by the HEM approach is in good agreement with the observed minimum temperature (around -43 °C). This minimum temperature is well below the normal boiling point of butane which is -0.5 °C. This is due to the cooling effect associated with the vaporization of liquid droplets inside the jet. Kukkonen et al. (1994) give a comprehensive explanation of the process. The cooling process can be understood in the following way. As air is entrained inside the jet, the volume fraction of the contaminant vapour is decreasing and so does the vapour pressure. The temperature of the jet at the source is the normal boiling point of the chemical. Since the vapour pressure is decreasing the mixture temperature must also decrease. The conservation of enthalpy for the mixture of dry air, vapour and liquid droplets must be satisfied as the temperature of the cloud decreases. The conservation of enthalpy can only be achieved if the liquid vaporizes and extracts the required amount of latent heat to reach equilibrium. When all the liquid has evaporated, air entrainment brings the mixture temperature back to the

Table 7.3: *Release conditions and parameters of the pseudo-source terms for the FLIE-INERIS tests.*

Test	Release conditions						Pseudo-source		
	D_{ori} (mm)	T_0 (K)	P_0 (bar)	$\dot{m}$ (kg/s)	T_a (K)	D_{imp} (m)	x_g (−)	U (m/s)	SMD (μm)
F	10	292	7.78	1.33	294	-	0.117	35	289
I1	10	285	3.40	0.60	290	0.83	0.073	20	286
I2	10	287	3.00	0.68	290	1.60	0.085	20	286
I3	10	286	3.18	0.58	290	2.57	0.083	20	286

ambient temperature. The cooling effect is also well captured in the Euler-Lagrange simulations. Two size distributions are used, the default log-normal distribution and a uniform distribution with a characteristic diameter of 145 μm. The results obtained with the uniform distribution are in better agreement with experimental data than the results obtained with the log-normal distribution.

Impinging butane jets

Three impinging butane jets are simulated with the HEM and the Euler-Lagrange approaches. We are mainly interested in the predictions of the amount of liquid which rains-out due to jet impingement. The three tests have similar release conditions, only the location of the obstacle varies from one test to another. The release conditions and the parameters of the pseudo-source are given in Table 7.3. A grid sensitivity study is performed with the HEM approach for one of the test. The obstacle is located 2.57 m away from the exit orifice. Two grids are tested: one grid with 240000 cells and one grid with 1400000 cells. The rain-out percentage on the coarse grid is 17 % and it is 15 % on the fine grid. As a consequence of the small difference in the results between the two grids the coarse grid is used for the remaining tests. The resolution in the x and y directions is 3.6 cm and 10 cm in the x-direction in the near field of the jet. The direction of the release is aligned with the x-direction. The time-step is set to 10^{-3} s and 60 parcels are released at each time-step. Two-way coupling is not activated. The atmospheric conditions used for the free jet simulation are employed for these impinging jets simulations.

The results are shown on Figure 7.6. As for the free butane jet the HEM approach seems to give the best predictions. We note that the amount of rain-out is largely overestimated when the obstacle is close to the release point (0.83 m in the tests). The closer the obstacle to the release point the stronger the momentum of the jet just before impacting on the wall. The relatively high momentum of the jet may explain the overestimation: the droplets impacting on the wall have a high velocity and thus may not totally rain-out but rebound and break-up into smaller droplets which would remain airborne. Moreover, in the simulations we assume that when a droplet impacts the wall, its whole mass deposits on the ground, i.e. we do not compute the vaporization of the liquid film on the vertical wall. All these observations certainly explain the overestimation seen in the Euler-Lagrange results. However, as expected, when the *SMD* is decreased the amount of rain-out decreases.

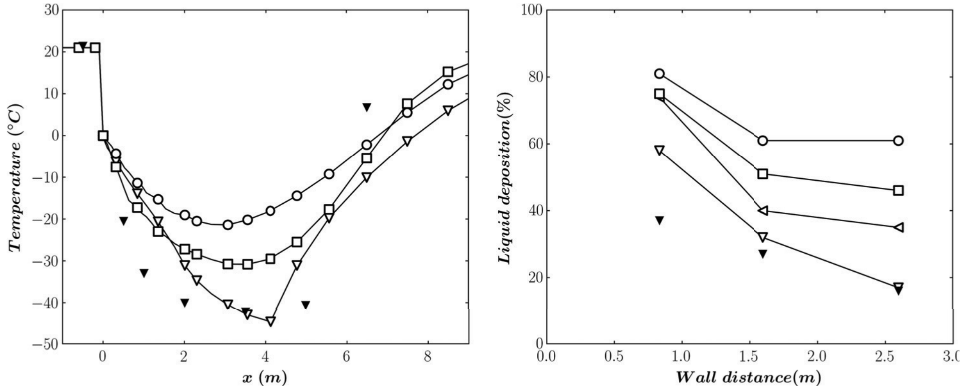

Figure 7.6: ***Left**, temperature profile along the centre-line axis of a free flashing jet of butane. Black symbols represent experimental data, (◯) represents the Euler-Lagrange simulation with a log-normal size distribution and SMD = 289 μm, (◁) represents Euler-Lagrange simulation with a uniform size distribution with characteristic diameter 145 μm and (∇) represents the HEM simulation. **Right**, percentage of rain-out as a function of wall distance: black symbols represent experimental data, (∇) represents Euler-Lagrange simulations with a log-normal size distribution with SMD = 286 μm, (◁) represents Euler-Lagrange simulations with a uniform size distribution with characteristic diameter 145 μm, (□) represents Euler-Lagrange simulations with a log-normal size distribution with SMD = 75 μm and (◯) represents HEM simulations.*

7.4 The Desert Tortoise experiments

Presentation of the experiments

The Desert Tortoise test series consists of four large scale releases of pressurized liquefied ammonia which were performed in the summer of 1983 by the Lawrence Livermore National Laboratory on the Frenchman Flat area of the Department of Energy's Nevada Test Site (Goldwire et al., 1985). The test site is ideal for conducting dispersion tests both due to the very flat terrain and regular wind patterns. The main objective of the tests was to measure the concentration of ammonia at two distances, 100 m and 800 m downstream of the release point. Ammonia was stored in two 41.5 m^3 capacity highway tanker trucks which were connected to a spill line with an orifice plate at the end. Ammonia was self-pressurized in the tanker trucks and additional nitrogen gas was used to maintain a constant pressure inside the tankers to obtain a constant flow rate. The exit orifice was 0.79 m above the ground and was specially designed such that the ammonia remained liquid until the end of the spill line. The gas concentration and the temperature of the gas cloud were measured at the same position. Gas concentrations and temperature were measured at heights of 1 m, 2.5 m and 6 m for the 100 m row and 1 m, 3.5 m and 8.5 m for the 800 m row. Eleven meteorological stations were used to evaluate the parameters of the atmospheric boundary layer over the test area. In the experiments the amount of rain-out was deduced form the integration of the mass fluxes through the first row of sensors. The integration was done over the duration of the spills and the difference between the mass spilled and the integrated mass fluxes at the 100 m row gave the amount of rain-out.

Table 7.4: *Meteorological data for the Desert Tortoise tests.*

Test	U_{ref} ($^{m}/_{s}$)	z_{ref} (m)	T_a (K)	z_0 (m)	Stability Class (−)	Monin-Obukhov length (m)
1	7.42	2	302	0.003	D	92.7
2	5.76	2	306	0.003	D	94.7
3	7.38	2	307	0.003	D	570.7
4	4.51	2	306	0.003	E	45.2

Table 7.5: *The release conditions and parameters of the pseudo-source terms for the Desert Tortoise tests.*

	Release conditions					Pseudo-source		
Test	D_{ori} (mm)	T_0 (K)	P_0 (bar)	$\dot{m}$ ($^{kg}/_{s}$)	t_{dur} (s)	x_g (−)	U ($^{m}/_{s}$)	SMD (μm)
1	81.0	294	10.13	80.95	126	0.174	97	143
2	94.5	293	11.16	117.25	255	0.171	86	158
3	94.5	295	11.37	133.13	166	0.178	84	153
4	94.5	297	11.79	107.87	381	0.184	94	131

Set-up of the simulations

The set-up of the Euler-Lagrange and HEM simulations of the four Desert Tortoise tests are now presented. First, a grid sensitivity study is conducted with the HEM approach for the test Desert Tortoise 1. The first grid has 380000 cells, the second grid has 1000000 cells and the third grid has 2000000 cells. The differences between the results obtained on the three grids are assessed by looking at the maximum concentrations at the 100 m and 800 m rows. At the 100 m and 800 m rows the results vary by a maximum of 6 %. We conclude that the 6 % difference does not justify the extra computational costs associated with the simulations on the grids with 1000000 and 2000000 cells. The computations with Euler-Lagrange and HEM approaches are conducted on the grid with 380000 cells. The mass flow rates were measured during the experiments. The parameters of the pseudo-source terms are estimated via the control volume approach and the SMD of the size distribution is taken as the mean of the SMD predicted by the Wilcox, CCPS and YB models. The size distribution is a log-normal distribution with a standard deviation of 1.8. The parameters of the pseudo-sources are reported in Table 7.5 for each of the four Desert Tortoise tests. The time-step is set to 1.13 10^{-2} s and the number of parcels injected inside the domain at each time-step is 40. Rain-out is expected and thus a grid for liquid spread and vaporization on the ground is defined. The grid has a resolution of 10 cm and extends from 0 m to 40 m in the x-direction and from -10 m to 10 m in the y-direction. Two-way coupling is not activated. As far as the atmospheric boundary layer is concerned, profiles for the wind, temperature and turbulent parameters are defined at the inflow boundaries. The Pasquill classes reported in Table 7.4 are used as inputs in the simulations.

Table 7.6: *Predicted and observed maximum concentrations for the Desert Tortoise tests at 100 m.*

	Short averaging time			Long averaging time		
Test	EXP (ppm)	HEM (ppm)	EUL-LAG (ppm)	EXP (ppm)	HEM (ppm)	EUL-LAG (ppm)
1	63260	73275	87524	49943	60702	65023
2	109580	87671	110886	83203	74146	75111
3	97250	105217	126477	76881	89218	97793
4	84260	83628	112967	57300	74608	97054

Table 7.7: *Predicted and observed maximum concentrations for the Desert Tortoise tests at 800 m.*

	Short averaging time			Long averaging time		
Test	EXP (ppm)	HEM (ppm)	EUL-LAG (ppm)	EXP (ppm)	HEM (ppm)	EUL-LAG (ppm)
1	10950	8200	7238	8843	7946	7174
2	18590	10951	10111	10804	10899	9936
3	15630	9038	9350	7087	8464	9137
4	20910	15342	16107	16678	13590	16045

Results: maximum concentrations

The maximum ammonia concentrations predicted by the HEM and Euler-Lagrange approaches at the 100 m and 800 m rows are compared with experimental observations. The results are shown in Table 7.6 and 7.7. Two averaging times are used. The short averaging time, 1 s, is the response time of the concentration sensors and these maximum concentrations approximate instantaneous maximum concentrations (Hanna et al., 1991). The second averaging time varies from one test to another and it is the averaging time recommended by Hanna et al. (1991). It roughly corresponds to the duration of the release. The predictions obtained with both approaches are in satisfying agreement with the experimental observations. At the 100 m row the maximum percentage difference between experimental data and HEM predictions is 20 % for the short averaging time and 30 % for the long averaging time. With the Euler-Lagrange formulation we obtain 38 % and 70 % for the short and long averaging time respectively. At the 800 m row the maximum percentage difference between experimental data and HEM predictions is 70 % for the short averaging time and 19 % for the long averaging time. With the Euler-Lagrange formulation we obtain 77 % and 29 % for the short and long averaging time respectively. All predictions are within a factor of two of the experimental observations. For the short and long averaging times, at the 100 m row, the maximum concentrations obtained with the Euler-Lagrange approach are always greater than the maximum concentrations obtained with the HEM approach. The results are discussed in more details by looking at the time-series of concentration and temperature at given sensor locations.

Results: time-series of concentration

The time-series of concentration for the test Desert Tortoise 1 are now discussed. A similar discussion could be reproduced for the other Desert Tortoise tests. The time-series obtained with the HEM and Euler-Lagrange approaches are compared with the experimental time-series. The wind is aligned with the direction of the release and thus the plume is symmetric with respect to the plane $y = 0$ m. We start the discussion with the time-series at the row of sensors located 100 m downstream of the exit orifice, Figures 7.7 and 7.8. We note that the time-series can be split in two time zones. The first time zone has a high concentration value and a duration which is about the duration of the release. The second time zone has a lower concentration value but a longer duration. In the first time zone, the concentrations, 1 m above the ground, predicted by the Euler-Lagrange approach are larger than the concentrations predicted by the HEM approach and the experimental concentrations. However, at 2.5 m above the ground, the Euler-Lagrange approach gives the lowest predictions. We may therefore deduce from these observations that in the Euler-Lagrange simulations the mass fraction of liquid ammonia droplets close to the ground (or at least 1 m above the ground) is too high. More droplets should be transported and vaporized at higher altitudes (for example at 2.5 m above the ground). Enhancing the transport of liquid droplets to higher altitudes would decrease the ammonia concentrations close to the ground and increase them at higher altitudes. The modification of the shape of the size distribution would certainly allow a better transport of droplets to higher altitudes.

The second time zone seen on Figures 7.7 and 7.8 corresponds to the vaporization of the pool resulting from liquid deposition on the ground. It is important to note that the duration of the hazard is greatly increased by the rain-out process. Indeed, long after the release stopped and the primary gas cloud has travelled through the 100 m row of sensors, ammonia is still evaporating from the pool. A secondary gas cloud is forming and the concentrations measured at the 100 m row are non-negligible: 1 m above the ground, the peak concentration of the secondary gas cloud is around 3 %, about half of the peak concentration associated with the primary gas cloud.

Figures 7.9 and 7.10 show the concentrations at the row of sensors 800 m downwind of the release point. The predictions of both models are in very good agreement with experimental observations. The only discrepancy concerns the concentration of the secondary gas cloud predicted by the HEM approach. It may indicate that the rain-out is over-estimated in the HEM simulations. This is confirmed by the results shown in Table 7.8. The amount of rain-out predicted with the Euler-Lagrange model is in good agreement with the experimental observations.

Results: time-series of temperature

The time-series of temperature 100 m downwind of the release point are shown on Figures 7.11 and 7.12. As expected the temperatures predicted by the Euler-Lagrange model 1 m above the ground, are lower than the experimental observations and the predictions of the HEM approach since the concentrations were in excess. For the HEM approach, the concentration is in good agreement with experimental observations at the sensor G05, 1 m above the ground and thus is the temperature at the same sensor. It illustrates the strong link between temperature and concentration. It is interesting to

Table 7.8: *Predicted and observed rain-out as a percentage of the total mass released for the four Desert Tortoise tests.*

Test	EXP (%)	HEM (%)	EUL-LAG (%)
1	20	49	40
2	36	57	42
3	39	56	43
4	30	53	37

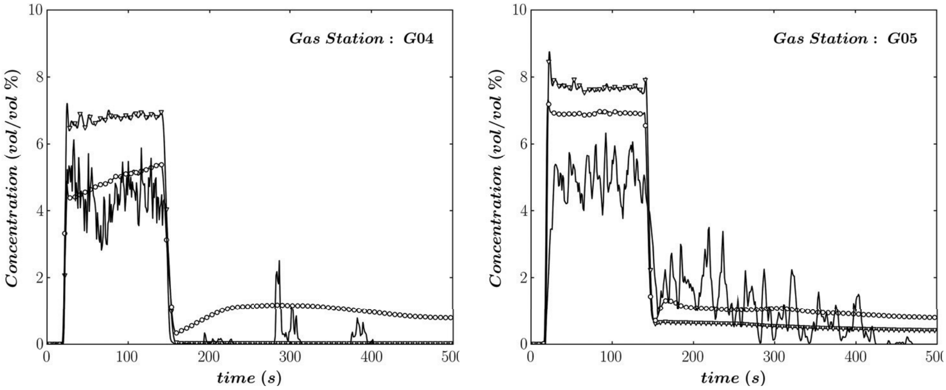

Figure 7.7: *Concentration time-series for the test Desert Tortoise 1. The sensors are located 100 m downstream of the release point at 1 m above the ground. Sensor G04 is at* $Y = 15.24\,m$ *and sensor G05 is at* $Y = 0\,m$*. The black line represents experimental data, (◯) represents the HEM simulation and (∇) represents the Euler-Lagrange simulation.*

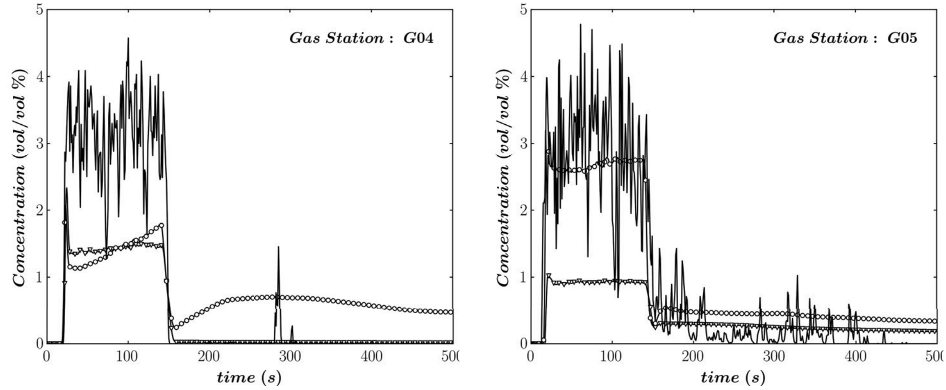

Figure 7.8: *Concentration time-series for the test Desert Tortoise 1. The sensors are located 100 m downstream of the release point at 2.5 m above the ground. Sensor G04 is at* $Y = 15.24\,m$ *and sensor G05 is at* $Y = 0\,m$*. The black line represents experimental data, (◯) represents the HEM simulation and (∇) represents the Euler-Lagrange simulation.*

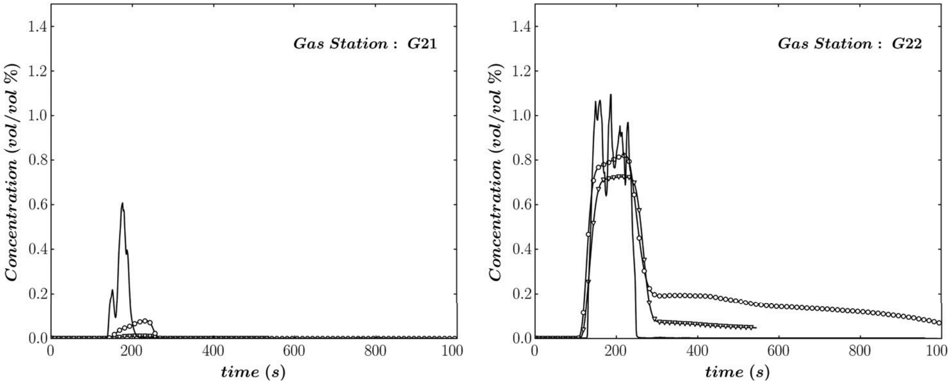

Figure 7.9: *Concentration time-series for the test Desert Tortoise 1. The sensors are located 800 m downstream of the release point at 1 m above the ground. Sensor G21 is at $Y = 100$ m and sensor G22 is at $Y = 0$ m. The black line represents experimental data, (◯) represents the HEM simulation and (∇) represents the Euler-Lagrange simulation.*

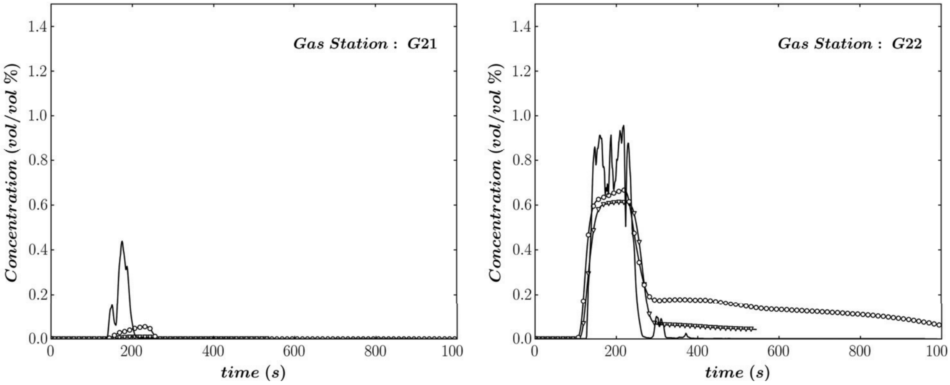

Figure 7.10: *Concentration time-series for the test Desert Tortoise 1. The sensors are located 800 m downstream of the release point at 3.5 m above the ground. Sensor G21 is at $Y = 100$ m and sensor G22 is at $Y = 0$ m. The black line represents experimental data, (◯) represents the HEM simulation and (∇) represents the Euler-Lagrange simulation.*

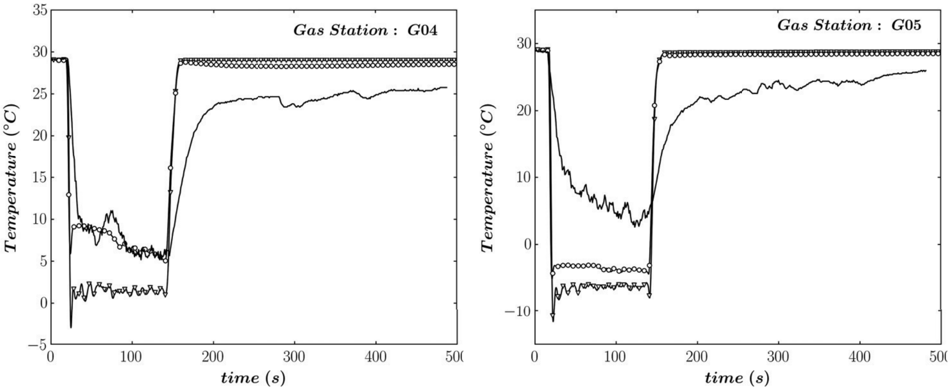

Figure 7.11: *Temperature time-series for the test Desert Tortoise 1. The sensors are located 100 m downstream of the release point at 1 m above the ground. Sensor G04 is at* $Y = 15.24\,m$ *and sensor G05 is at* $Y = 0\,m$*. The black line represents experimental data, (◯) represents the HEM simulation and (∇) represents the Euler-Lagrange simulation.*

note that in our computations, at 1 m above the ground the temperature goes back to the ambient temperature faster than in reality. One explanation could be that due to the presence of the cold gas cloud the ground is cooling down. The air located near the ground stays cold longer than the air at higher altitudes. This is confirmed by the time-series of temperature at 2.5 m above the ground. The heat transfer between the gas cloud and the ground is not taken into account in our computations.

Results: concentration contours

The contours of ammonia concentration 100 m downwind, 100 s after start of release are shown on 7.13. The contours are for the test 1. The experimental contours were derived from the concentration measurements at given sensor locations by means of linear and quadratic interpolations (Goldwire et al., 1985). Close to the ground the width of the gas cloud compares well with the experimental observation. As expected from the time-series of concentration the height of the gas cloud obtained with the Euler-Lagrange model is under-estimated. A better prediction is obtained with the HEM approach. However, both methods exhibit a too strong dense gas behaviour illustrated by the 4 % contour. There is a lack of turbulent mixing. Increasing turbulence mixing would decrease the size of the 4 % contour and increase the size of the 0.5 % contour. Several options can be considered in order to improve the quality of the results. The first options concerns the representation of the pseudo-source term. In the current computations the release is aligned with the x-direction. However, the strong expansion of the jet associated with the flashing process may generate a radial momentum. Imposing a radial momentum at the source may help decreasing the maximum concentrations at the 100 m row. The second option could deal with humidity effects and chemical reaction between water and ammonia. Condensation of the water vapour present in the air would release heat favouring buoyancy effects and a better mixing of the gas cloud would occur.

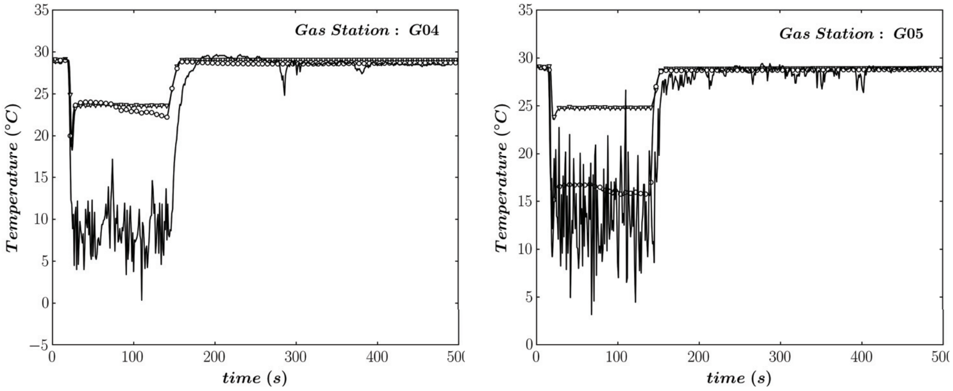

Figure 7.12: *Temperature time-series for the test Desert Tortoise 1. The sensors are located 100 m downstream of the release point at 2.5 m above the ground. Sensor G04 is at* $Y = 15.24$ *m and sensor G05 is at* $Y = 0$ *m. The black line represents experimental data, (◯) represents the HEM simulation and (∇) represents the Euler-Lagrange simulation.*

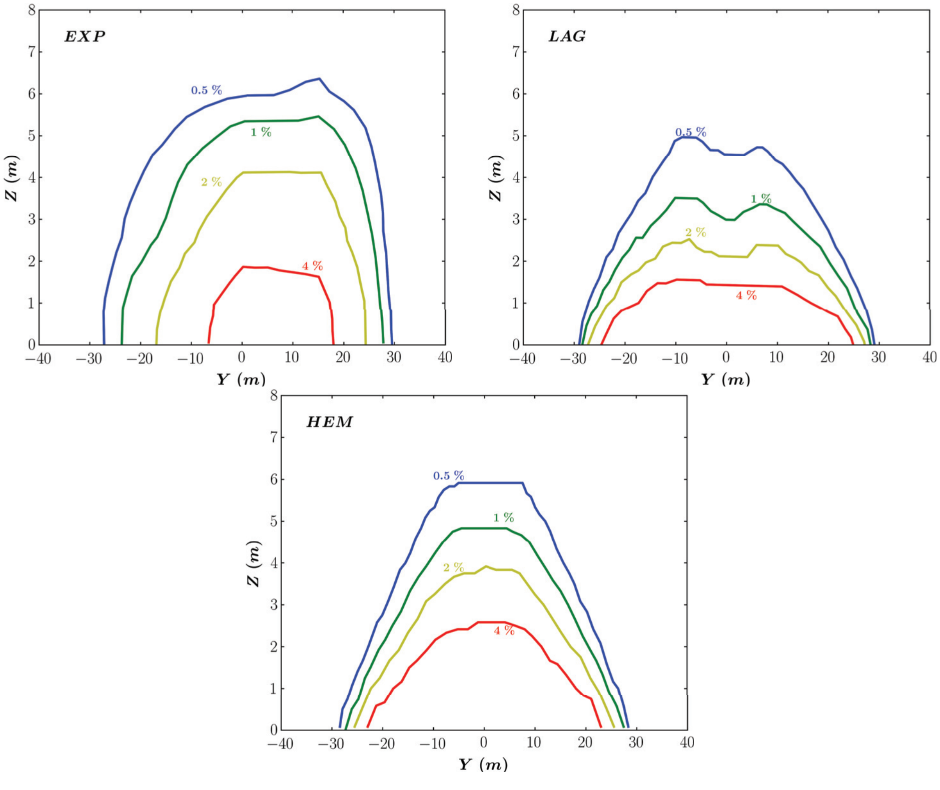

Figure 7.13: *Concentration contours for the test Desert Tortoise 1, 100 s after start of release, 100 m downwind of release point.*

7.5 The Falcon experiments

Description of the experiments

The Falcon test series consisted of five large-scale LNG spill tests performed by the Lawrence Livermore National Laboratory in 1987 at Frenchman Flat, Nevada (Brown et al., 1990). The purpose of the tests was to evaluate the effectiveness of vapour fences as a mitigation technique for accidental LNG releases as well as to provide a data set for model validation purposes. For this reason, LNG was spilled onto a specially designed water pond equipped with a circulating system to maximize evaporation of the LNG pool. LNG was delivered through a spill "spider" consisting of four pipes (each 11.6 m long) spaced at 90 degrees intervals in order to distribute the LNG pool over the water pond. The ends of the spider arms pointed downward and were fitted with splash plates at the water surface, to prevent the LNG from sinking into the water, see Figure 7.14. Gas concentration and temperature sensors were mounted on towers distributed in three rows at 50 m, 150 m and 250 m from the fenced area.

Previous simulations of the Falcon tests

In previous simulations, the FLACS pool model was used to calculate the spreading and vaporization of the LNG pool formed by the spill (Hansen et al., 2010a). The main geometry features, including the spill pond, vapour fences and walls were included in the model. In these simulations the predicted gas concentrations at the first row of sensors (50 m downwind) were much lower than the experimental results. For example, for the test Falcon 1, the maximum gas concentration observed 50 m downwind was 35.9 % for the short averaging time (1 s) and 14.6 % for the long averaging time (50 s). The predicted maximum concentrations were 3.6 % and 3.16 % for the short and long averaging times respectively. The strong under-estimation is most likely due to the different way the LNG source term was represented in the simulations versus the actual LNG spill mechanism in the experiments. As indicated above, the FLACS simulations used the pool model to calculate the LNG vapour generation from the spill. In the Falcon tests, the tall vapour fence shields the LNG pool from the ambient wind and the characteristics of the LNG release control the growth of the vapour cloud within the fenced area (Gavelli et al., 2008). Based on a review of videos from the Falcon 5 test (see Figure 7.15), the LNG release appears to be a high-pressure jet with associated

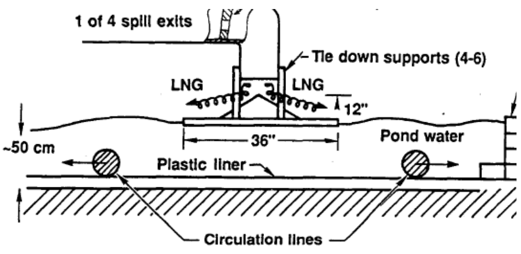

Figure 7.14: *Schematic of the release device used in the Falcon tests (taken from Brown et al. (1990)).*

Figure 7.15: *Photograph of the test Falcon 5 (courtesy of Ron Koopman).*

flashing and aerosol formation. The HEM approach is used to test the assumption that the LNG is released as a high-pressure two-phase jet.

Set-up of the simulations

The test Falcon-1 is simulated with the HEM approach. Several assumptions need to be made in order to model the flow through the release system illustrated on Figure 7.14. Different options are tested. The best option is to model the release as four 45 degree horizontal two-phase jets. The four leaks are located in the first grid cell above the water surface. The areas of the leaks are fixed by the geometrical constraints (see Figure 7.14). The diameter of the leaks is 12 inches. The release configuration can be seen on Figure 7.16. The computation of the mass fraction of vapour generated by the flashing process and/or vaporization of the liquid in the release system is not an easy task. A sensitivity study was performed on the source term. Several values for the mass fraction of gas at the source were tested and three of the values tested are reported in Table 7.10. One test gives satisfying predictions for the concentrations downwind of the fence, the two other tests (one with a lower gas mass fraction and one with a higher gas mass fraction) give poor results. The tests conditions and the parameters of the pseudo-source are summarized in Table 7.9 and 7.10. The size of the simulation domain goes from -150 m to 400 m in the x-direction, from -200 m to 155 m in the y-direction and from 0 m to 50 m in the z-direction. The total number of grid cells is 630000.

Results and discussions

The predictions of the HEM approach are compared with experimental data. Time series of concentration are shown on Figure 7.17. Four sensors 1 m above the ground are considered. The best predictions are obtained with the set-up 1a and the concentration time-series compare well with the experimental ones. The simulations performed with

Table 7.9: *Meteorological data for the test Falcon 1.*

Test	U_{ref} (m/s)	z_{ref} (m)	T_a (K)	z_0 (m)	Stability Class (−)	Monin-Obukhov length (m)
1	1.7	2	306	0.008	G	4.963

Table 7.10: *The release conditions and parameters of the pseudo-source terms for the test Falcon 1.*

	Release conditions					Pseudo-source	
Test	D_{ori} (mm)	T_0 (K)	P_0 (bar)	$\dot{m}$ (kg/s)	t_{dur} (s)	x_g (−)	A (m^2)
1a	114.3	-	-	200.0	131	0.807	0.073
1b	114.3	-	-	200.0	131	1.000	0.073
1c	114.3	-	-	200.0	131	0.455	0.073

the set-up 1b and 1c are not able to reproduce experimental observations. Figure 7.18 contains an explanation for the failure of the set-up 1b and 1c.

LNG is a mixture of different chemicals with 90-95 % of methane in volume and thus the mixture is often approximated as pure methane. Methane has a molecular weight of 16.043 g/mol. In its gaseous form methane is lighter than air. However, it has been observed experimentally (Koopman and Ermak, 2007) that a LNG gas cloud is dispersing as a dense gas cloud. The dense gas behaviour of a LNG gas cloud is due to its cold temperature. Indeed, the normal boiling point of methane is around 111 K and at this temperature the density of methane vapour is 1.819 kg/m^3 versus 0.86 kg/m^3 at 288 K. The density of air at 288 K is 1.22 kg/m^3.

We now discuss the features of the temperature field obtained in the simulations 1a, 1b and 1c. On Figure 7.18 we observe that for the simulation 1b, the temperature of the gas cloud is around 270 to 280 K which is not cold enough for the LNG vapour to behave as a dense gas. Consequently, the vapour is more buoyant than it should be and disperse too quickly in the atmosphere. In order to improve the predictions the gas cloud needs to be cooled down. One way to achieve this is to include some liquid droplets at the source. The vaporization of the droplets will continuously cool down the gas cloud and due to their high density they will increase the dense gas behaviour of the gas cloud. This is the case 1c. On Figure 7.18 we note that the LNG vapour is trapped inside the fence. The introduction of liquid droplets at the source has decreased the momentum of the two-phase LNG jets and the LNG vapour does not have enough momentum to flow over the fences. The correct combination of liquid fraction and momentum at the source has to be found. The correct behaviour is obtained with set-up 1a. This sensitivity study on the mass fraction of gas at the source illustrates the importance of source and pseudo-source term predictions. In this example, by increasing the amount of gas at the source by less than a factor of two, the situation, from a risk analysis point of view, went from a "zero-risk" scenario (no flammable gas cloud was formed outside the fences) to a critical scenario.

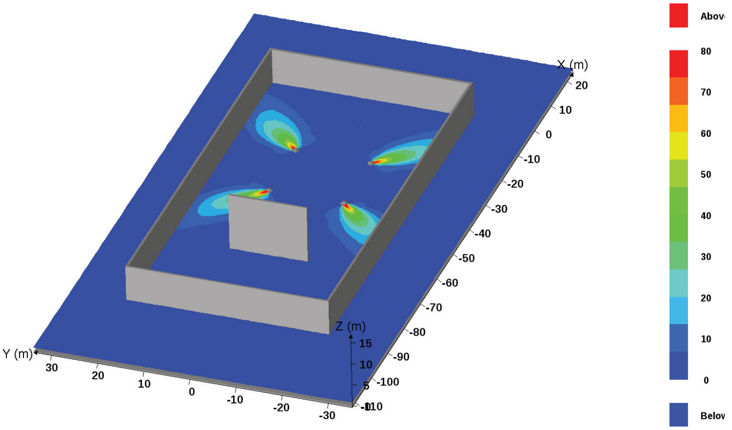

Figure 7.16: *Cut plane showing the mean velocity of the released LNG for the test Falcon 1.*

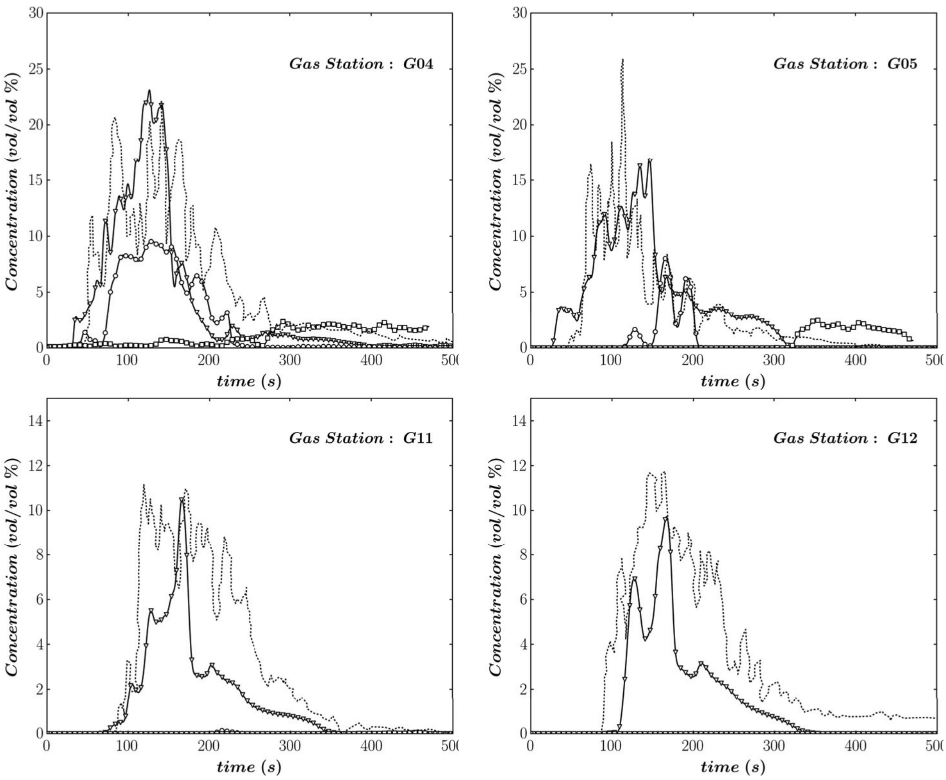

Figure 7.17: *Concentration time-series for the test Falcon 1. Sensors G04 and G05 are located 50 m downstream of the release point and sensors G11 and G12 are 150 m downstream. 1 m above ground for the four sensors. The black line represents experimental data, (∇) represents the HEM simulation with set-up 1a, (◯) with set-up 1b and (□) with set-up 1c.*

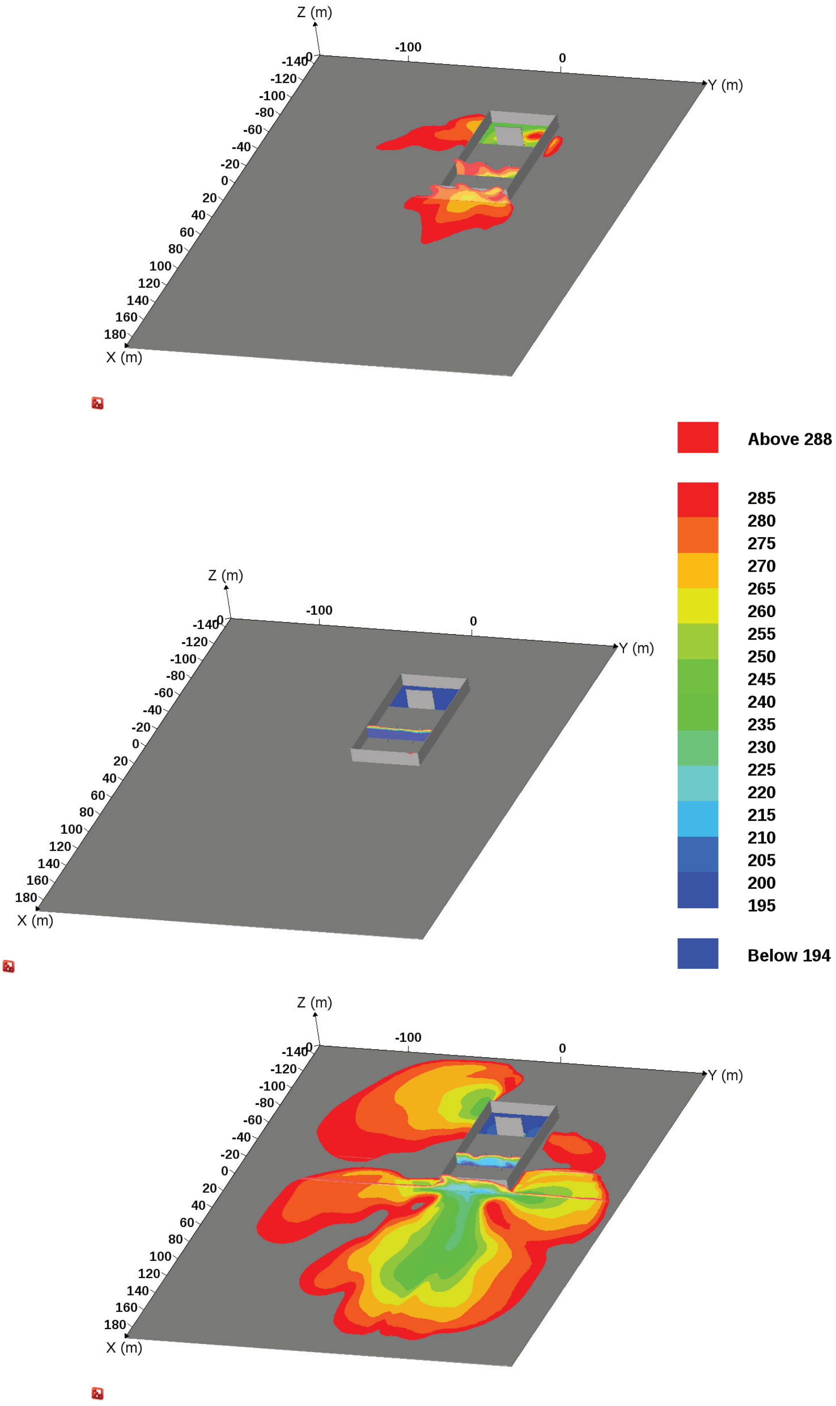

Figure 7.18: *3D cut planes of temperature for the test Falcon 1.* ***Top plot****, is for set-up 1b,* ***middle plot*** *is for set-up 1c and* ***bottom plot*** *is for set-up 1a.*

7.6 Application to consulting projects

HFO-1234 Indoor dispersion study

This project is currently conducted in the US office of GexCon. The HEM approach is used to perform CFD simulations of indoor dispersion of HFO-1234 refrigerants, an alternative series of refrigerants being evaluated for residential HVAC applications. The customer initiated this project as a response to a Request For Proposals issued by the Air-Conditioning, Heating and Refrigeration Institute (AHRI) for a project titled “Risk Assessment of Residential Heat Pump System Using 2 L Flammable Refrigerants”. A generic residential unit was defined: a two-level (main floor and basement), two-bedroom single-family home with attic space and an attached garage; and the dispersion of three (3) different refrigerants (HFO-1234yf, HFO-1234ze and HFC-32) in this generic residential unit was computed. The thermodynamic properties and storage conditions of the refrigerants resulted in the formation of a flashing jet in a confined and obstructed environment; a scenario requiring the use of two-phase flow models.

FLNG cryogenic leak dispersion analysis

This project is currently conducted in the US office of GexCon. The customer and his co-research partners are intended to clarify the risk of asset damage and plant unavailability of FLNG triggered by cryogenic embrittlement. The primary objective of the study is to perform a Cryogenic Leak Dispersion Analysis. The HEM approach is used to compute the dispersion of two-phase flashing jets in obstructed environment. The amount of rain-out and subsequent pool formation on the hull deck is a major stake of this project.

The Jack Rabbit test series

The Jack Rabbit test series were performed in 2010 and consisted of a series of experiments involving releases of ammonia and chlorine from pressurized tanks of $2\,m^3$ nominal capacity (Storwold et al., 2011). The scope of the tests was to provide experimental data that may be used to better understand the behaviour of the flashing jet release, as well as to help validate atmospheric dispersion models that may be later used to predict the consequences of accidental releases. The downward two-phase jets were impacting within 1 m or so on the ground. These experiments were simulated with the HEM approach (Gavelli et al., 2011b). A research proposal was issued by Mr Koopman and intended to further define with the help of HEM simulations, what happens to the vapour / liquid / aerosol jet source as it travels from the tank outlet and impacts the flat plate on the ground. The end point of the proposed analysis is the source for an atmospheric dispersion model that will be used to predict the consequences of such a release. The proposal was accepted.

Simulations to predict flame inhibitor concentrations during release tests in the Carling steamcracker facility

A proposal was issued to Total Petrochemicals describing the work needed to perform CFD-predictions of flame inhibitor concentrations to be expected during flame inhibitor release tests planned to be performed in the abandoned Carling steamcracker facility in France. The proposed work is part of the ongoing development of a flame inhibitor injection system for reducing the consequences of vapour cloud explosions. The simulations would be performed in connection with experiments to be conducted on 1 and 2 February 2012 in Carling with a first version of the flame inhibitor injection system. The proposal outlines two project phases. The first phase deals with the verification of the CFD-tool on the basis of the concentration measurements performed during the experiments and the second phase concerns the extrapolation of the results investigating variation of weather conditions and properties of the flame inhibitor injection system.

7.7 Conclusions

Large scale releases of pressurized liquefied gas into the atmosphere were simulated with the HEM and Euler-Lagrange approaches. The HEM approach can be used with confidence when simulating releases of volatile liquids into the atmosphere. The predictions of liquid deposition with the model proposed in association with the HEM approach are found to be of satisfying accuracy when compared to experimental data. The results obtained with the Euler-Lagrange approach compare well with experimental data and are very encouraging. The Euler-Lagrange approach can be used to test assumptions for the source term of flashing releases. Different types of size distribution for the droplets and even velocity distribution could be tested and the impacts on the percentage of rain-out at vapour concentration downstream of the release point could be assessed. A better understanding of flashing releases would follow.

Chapter 8

Conclusions and further work

8.1 Conclusions

In this thesis a CFD methodology for the simulation of releases of pressurized liquefied gas into the atmosphere has been developed and used to simulate large-scale experiments. Both obstructed and non-obstructed experiments were considered, including the CCPS (Johnson and Woodward, 1999), FLIE-INERIS (Bonnet et al., 2005), Desert Tortoise (Goldwire et al., 1985) and Falcon (Brown et al., 1990) experiments. Two different approaches for simulating two-phase turbulent flows can be employed: the Homogeneous Equilibrium Model (HEM) approach and the Euler-Lagrange approach.

It has been shown that the rain-out process could greatly increase the duration of the hazard associated with releases of pressurized liquefied gas. Therefore, any realistic simulations of pressurized liquefied gas releases should be able to account for the rain-out process and subsequent evaporation of the liquid on the ground. The presence of obstacles in the near field of the release increases the amount of liquid that deposits on the ground. The CFD model FLACS with the new two-phase models is able to account for the effects of obstacles. The importance of accurate predictions for the source term of flashing releases was emphasized in the simulations of the Falcon tests. The validation of the methodology with both modelling approaches was successful.

The HEM approach assumes thermal and kinematic equilibrium between the two phases, and the disperse phase is fully characterized by the specification of its volume fraction at the source. Its simplicity of use makes the HEM approach very attractive for industrial applications. However, the HEM approach have some limitations associated with the assumption of infinitely fast inter-phase transport rates, and may fail when the normal boiling point of the substance is close to the ambient temperature.

The Euler-Lagrange approach has a wider range of physical applications and provides more options for characterizing the dispersed phase and its interaction with the continuous phase. The Euler-Lagrange formulation could also be used to test assumptions regarding the source term of flashing releases such as the shape of size and velocity distributions. New experimental investigations of the source term of flashing liquids should also provide additional knowledge on the dispersion of flashing liquids. Finally, the Euler-Lagrange approach, as implemented in the FLACS model, is a tool which can be employed in many other domains such as the evaluation of water spray systems, testing of release systems for flame inhibitors or dust explosions.

8.2 Further work

The work presented in this thesis may be extended along various avenues including:

- Advanced models such as the Homogeneous Relaxation Model of Bilicki and Kestin (1990); Downar-Zapolski et al. (1996) or the model proposed by Saurel et al. (2008) could be used to compute flashing of liquids inside pipes and nozzles.
- Laboratory experiments should be carried out to obtain more data on particle size distributions and help developing models for the pseudo-source term of flashing liquids.
- Models for particle-wall interactions need to be implemented in the Euler-Lagrange approach.
- Humidity effects on the dispersion of two-phase gas clouds need to be accounted for.
- With respect to computational efficiency, a parallelisation of the Euler-Lagrange code might be necessary.

Bibliography

Aamir, M. and Watkins, A. Numerical analysis of depressurisation of highly pressurised liquid propane. *International Journal of Heat and Fluid Flow*, 21(4): 420 – 431, 2000.

Abbasi, T. and Abbasi, S. The boiling liquid expanding vapour explosion (BLEVE): Mechanism, consequence assessment, management. *Journal of Hazardous Materials*, 141(3):489 – 519, 2007.

Abramzon, B. and Sirignano, W. A. Droplet vaporization model for spray combustion calculations. *International Journal of Heat and Mass Transfer*, 32(9):1605 – 1618, 1989.

Aggarwal, S. K. and Peng, F. A review of droplet dynamics and vaporization modeling for engineering calculations. *Journal of Engineering for Gas Turbines and Power*, 117(3):453–461, 1995.

Aggarwal, S. K., Sirignano, W. A., and Tong, A. Y. A comparison of vaporization models in spray calculations. *AIAA Journal*, 22:1448–1457, 1984.

Allen, J. Laser-based measurements in two-phase flashing propane jets. Part one: velocity profiles. *Journal of Loss Prevention in the Process Industries*, 11(5):291 – 297, 1998a.

Allen, J. Laser-based measurements in two-phase flashing propane jets. Part two: droplet size distribution. *Journal of Loss Prevention in the Process Industries*, 11 (5):299 – 306, 1998b.

Amielh, M., Djeridane, T., Anselmet, F., and Fulachier, L. Velocity near-field of variable density turbulent jets. *International Journal of Heat and Mass Transfer*, 39(10):2149 – 2164, 1996.

Appleton, P. R. A study of axi-symmetric two-phase flashing jets. Technical Report SRD-R-303, U.K.A.E.A., Culcheth, Warrington, Cheshire, United Kingdom, 1984.

Armenio, V. and Fiorotto, V. The importance of the forces acting on particles in turbulent flows. *Physics of Fluids*, 13(8):2437–2440, 2001.

Arntzen, B. J. *Modelling of turbulence and combustion for simulation of gas explosions in complex geometries*. PhD thesis, NTNU, Trondheim, 1998.

Arya, S. *Introduction to micrometeorology*. International geophysics series. Academic Press, 2001. ISBN 9780120593545.

Babinsky, E. and Sojka, P. Modeling drop size distributions. *Progress in Energy and Combustion Science*, 28(4):303 – 329, 2002.

Bakke, J. R. and Brewerton, R. Buncefield explosion analysis. Technical Report GexCon-08-40419-RA-1, GexCon AS, 2008.

Bakke, J. R., van Wingerden, K., Hoorelbeke, P., and Brewerton, B. A study on the effect of trees on gas explosions. *Journal of Loss Prevention in the Process Industries*, 23(6):878 – 884, 2010.

Ball, C. G. and Pollard, A. A review of experimental and computational studies of flow from the round jet. Technical Report CEFDL/2007/01, Computational and Experimental Fluid Dynamics Laboratory, Department of Mechanical and Materials Engineering, Queen's University, Kingston, Ontario, Canada, 2007.

Basset, A. B. *A treatise on hydrodynamics*. Cambridge: Deighton, Bell and Co (originally published by George Bell and Sons, London, 1888), 1984.

Batchelor, G. *An introduction to fluid dynamics*. Cambridge mathematical library. Cambridge University Press, 2000, 1967. ISBN 9780521663960.

Bigot, J. P., Touil, A., Bonnet, P., and Lacome, J. M. Rain-out investigation: Initial droplet size measurement. *Journal of Loss Prevention in the Process Industries*, 18 (4–6):433 – 442, 2005.

Bilicki, Z. and Kestin, J. Physical aspects of the relaxation model in two-phase flow. *Proceedings of the Royal Society of London. A. Mathematical and Physical Sciences*, 428(1875):379–397, 1990.

Blewitt, D. N., Yohn, J. F., Koopman, R. P., and Brown, T. C. Conduct of anhydrous hydrofuoric acid spill experiments. In *Proc Int Conf on Vapour Cloud Modelling*, pages 1–38, 1987. (AIChE, New York).

Boersma, B. J., Brethouwer, G., and Nieuwstadt, F. T. M. A numerical investigation on the effect of the inflow conditions on the self-similar region of a round jet. *Physics of Fluids*, 10(4):899–909, 1998.

Bonnet, P., Bricout, P., Jamois, D., and Meunier, P. Description of experimental large scale two-phase release tests. Technical Report No 41508, INERIS, 2005.

Boussinesq, J. *Theorie analytique de la chaleur*. Paris, 1903.

Brennen, C. *Fundamentals of multiphase flow*. Cambridge University Press, 2005. ISBN 9780521848046.

Bricard, P. and Friedel, L. Two-phase jet dispersion. *Journal of Hazardous Materials*, 59(2–3):287 – 310, 1998.

Britter, R. Dispersion of two phase flashing releases - FLADIS field experiment. A further note on modeling flashing releases. Technical Report FM89/3, Cambridge Environmental Research Consultants Ltd., 1995.

Britter, R., Weil, J., Leung, J., and Hanna, S. Toxic industrial chemical (TIC) source emissions modeling for pressurized liquefied gases. *Atmospheric Environment*, 45 (1):1 – 25, 2011.

Brown, T. C., Cederwall, R. T., Chan, R. T., Ermak, S. T., Koopman, R. P., and Lamson, K. C. Falcon series data report: 1987 LNG vapor barrier verification field. Technical Report GRI-89/0138, Gas Research Institute, 1990.

Buevich, Y. A. Motion resistance of a particle suspended in a turbulent medium. *Fluid Dynamics*, 1:119–119, 1966.

Calay, R. and Holdo, A. Modelling the dispersion of flashing jets using CFD. *Journal of Hazardous Materials*, 154(1–3):1198 – 1209, 2008.

Chen, C. J. and Rodi, W. Vertical turbulent buoyant jets: A review of experimental data. *NASA STI/Recon Technical Report A*, 1980.

Cleary, V., Bowen, P., and Witlox, H. Flashing liquid jets and two-phase droplet dispersion: I. Experiments for derivation of droplet atomisation correlations. *Journal of Hazardous Materials*, 142(3):786 – 796, 2007.

Clift, R., Grace, J., and Weber, M. *Bubbles, drops, and particles*. Dover books on engineering. Dover Publications, 2005. ISBN 9780486445809.

Corrsin, S. and Lumley, J. On the equation of motion for a particle in turbulent fluid. *Applied Scientific Research*, 6:114–116, 1956.

Crowe, C. *Multiphase flow handbook*. Mechanical engineering series. CRC, 2006. ISBN 9780849312809.

Crowe, C., Schwarzkopf, J., Sommerfeld, M., and Tsuji, Y. *Multiphase Flows With Droplets and Particles*. Taylor and Francis, 1998. ISBN 9781439840504.

Csanady, G. T. Turbulent diffusion of heavy particles in the atmosphere. *Journal of Atmospheric Sciences*, 20:201–208, 1963.

Darby, R., Meiller, P., and Stockton, J. Select the best model for two-phase relief sizing. *Chemical Engineering Progress*, 97(5):56–64, 2001.

Dharmavaram, S., Hanna, S. R., and Hansen, O. R. Consequence analysis—using a CFD model for industrial sites. *Process Safety Progress*, 24(4):316–272, 2005.

Djeridane, T., Amielh, M., Anselmet, F., and Fulachier, L. Velocity turbulence properties in the near-field region of axisymmetric variable density jets. *Physics of Fluids*, 8(6):1614–1630, 1996.

Dowling, D. R. and Dimotakis, P. E. Similarity of the concentration field of gas-phase turbulent jets. *Journal of Fluid Mechanics*, 218:109–141, 1990.

Downar-Zapolski, P., Bilicki, Z., Bolle, L., and Franco, J. The non-equilibrium relaxation model for one-dimensional flashing liquid flow. *International Journal of Multiphase Flow*, 22(3):473 – 483, 1996.

Dumouchel, C. The maximum entropy formalism and the prediction of liquid spray drop-size distribution. *Entropy*, 11(4):713–747, 2009.

Einstein, A. On the movement of small particles suspended in stationary liquids required by the molecular-kinetic of heat. *Ann. Phys.*, 17:549–560, 1905.

Elghobashi, S. On predicting particle-laden turbulent flows. *Applied Scientific Research*, 52:309–329, 1994.

Elias, E. and Lellouche, G. Two-phase critical flow. *International Journal of Multiphase Flow*, 20, Supplement 1(0):91 – 168, 1994.

EPA. Chlorine. `http://www.epa.gov/ttn/atw/hlthef/chlorine.html`, 2007.

Epstein, M., Fauske, H., and Hauser, G. A model of the dilution of a forced two-phase chemical plume in a horizontal wind. *Journal of Loss Prevention in the Process Industries*, 3(3):280 – 290, 1990.

Faeth, G. M. Evaporation and combustion of sprays. *Progress in Energy and Combustion Science*, 9(1–2):1 – 76, 1983.

Fauske, H. K. Flashing flows or: Some practical guidelines for emergency releases. *Plant/Operations Progress*, 4(3):132–134, 1985.

Fauske, H. K. and Epstein, M. Source term considerations in connection with chemical accidents and vapour cloud modelling. *Journal of Loss Prevention in the Process Industries*, 1(2):75 – 83, 1988.

Fellouah, H., Ball, C., and Pollard, A. Reynolds number effects within the development region of a turbulent round free jet. *International Journal of Heat and Mass Transfer*, 52:3943–3954, 2009.

FLACS. *FLACS v9.1 User's Manual*. GexCon AS, 2010.

Forester, H. K. and Zuber, N. Growth of a vapor bubble in a superheated liquid. *J. Applied Physics*, 25(4):474 – 478, 1954.

Fox, R. O. and Yeung, P. K. Improved lagrangian mixing models for passive scalars in isotropic turbulence. *Physics of Fluids*, 15(4):961–985, 2003.

Foysi, H., Mellado, J. P., and Sarkar, S. Large-eddy simulation of variable-density round and plane jets. *International Journal of Heat and Fluid Flow*, 31(3):307 – 314, 2010.

Fthenakis, V., Rohatgi, U., and Chung, B. A simple model for predicting the release of a liquid-vapor mixture from a large break in a pressurized container. *Journal of Loss Prevention in the Process Industries*, 16(1):61 – 72, 2003.

Gant, S. E., Heather, A., and Kelsey, A. CFD modeling of evaporating hydrocarbon sprays. Technical Report CM/07/04, Health and Safety Laboratory, Harpur Hill, Buxton, United Kingdom, 2007.

Gardiner, C. W. *Handbook of stochastic methods for physics, chemistry and the natural sciences*. 1985.

Gavelli, F., Bullister, E., and Kytomaa, H. Application of CFD (Fluent) to LNG spills into geometrically complex environments. *Journal of Hazardous Materials*, 159(1): 158 – 168, 2008.

Gavelli, F., Davis, S., Ichard, M., and Hansen, O. CFD simulation of gas dispersion from large-scale toxic chemical releases in complex environments. In *2011 Mary Kay O'Connor Process Safety Center*, International Symposium, pages 132–148, October 25-27, 2011a. College Station, Texas, USA.

Gavelli, F., Ichard, M., Davis, S., and Hansen, O. R. CFD simulations of the Jack Rabbit ammonia and chlorine release experiments using FLACS. In *91st American Meteorological Society Annual Meeting, Special Symposium on Applications of Air Pollution Meteorology*, January 23-27, 2011b. Seattle, WA, USA.

George, W. K. The self- preservation of turbulent flows and its relation to initial conditions and coherent structures. In *Advances in Turbulence*, pages 39–73. Springer Verlag, New York, 1989.

GexCon, U. S. `http://gexconus.com/FLACS_approval`, 2011.

Golder, D. Relations among stability parameters in the surface layer. *Boundary-Layer Meteorology*, 3:47–58, 1972.

Goldwire, H. C., Rodean, H. C., Cederwall, R. T., Kansa, E. J., Koopman, R. P., and McClure, J. W. Coyote series data report: LLNL/NWC 1981 LNG spill tests dispersion, vapor burn and rapid phase transition, vols 1-2. Technical Report UCID-19953, Lawrence Livermore National Laboratory., 1983.

Goldwire, H. C., McRae, T. G., Johnson, G. W., Hipple, D. L., Koopman, R. P., McClure, J. W., Morris, L. K., and Cederwall, R. T. Desert tortoise series data report: 1983 pressurised ammonia spills. Technical Report UCID-20562, Lawrence Livermore National Laboratory, Livermore, Calfornia, 1985.

Gouesbet, G. and Berlemont, A. Eulerian and lagrangian approaches for predicting the behaviour of discrete particles in turbulent flows. *Progress in Energy and Combustion Science*, 25(2):133 – 159, 1998.

Hahne, E. and Barthau, G. Evaporation waves in flashing processes. *International Journal of Multiphase Flow*, 26(4):531 – 547, 2000.

Han, J., Arya, S. P., Shen, S., and Lin, Y. L. An estimation of turbulent kinetic energy and energy dissipation rate based on atmospheric boundary similarity theory. Technical Report CR-2000-210298, NASA, 2000.

Hanjalic, K. and Launder, B. *Modelling Turbulence in Engineering and the Environment: Second-Moment Routes to Closure*. Cambridge University Press, 2011. ISBN 9780521845755.

Hanna, S. R., Briggs, G. A., and Hosker, R. P. *Handbook on atmospheric diffusion*. Technical Information Center, U.S. Department of Energy, 1982.

Hanna, S. R., Strimaitis, D. G., and Chang, J. C. Hazard response modelling uncertainty (a quantitative method), volume II: Evaluation of commonly-used hazardous gas dispersion models. Technical Report Volume II, Sigma Research Corporation, 1991.

Hanna, S. R., Hansen, O. R., and Dharmavaram, S. FLACS CFD air quality model performance evaluation with Kit Fox, MUST, Prairie Grass, and EMU observations. *Atmospheric Environment*, 38(28):4675 – 4687, 2004.

Hanna, S. R., Dharmavaram, S., Zhang, J., Sykes, I., Witlox, H., Khajehnajafi, S., and Koslan, K. Comparison of six widely-used dense gas dispersion models for three recent chlorine railcar accidents. *Process Safety Progress*, 27(3):248–259, 2008.

Hanna, S. R., Hansen, O. R., Ichard, M., and Strimaitis, D. CFD model simulation of dispersion from chlorine railcar releases in industrial and urban areas. *Atmospheric Environment*, 43(2):262 – 270, 2009.

Hansen, O. R., Melheim, J., and Storvik, I. CFD modeling of LNG dispersion experiments. In *AIChE Spring National Meeting and Forty-first Annual Loss Prevention Symposium*, 22-26 April, 2007. Houston, TX, USA.

Hansen, O. R., Gavelli, F., Ichard, M., and Davis, S. G. Validation of FLACS against experimental data sets from the model evaluation database for LNG vapor dispersion. *Journal of Loss Prevention in the Process Industries*, 23(6):857 – 877, 2010a.

Hansen, O. R., Hinze, P., Engel, D., and Davis, S. Using computational fluid dynamics (CFD) for blast wave predictions. *Journal of Loss Prevention in the Process Industries*, 23(6):885 – 906, 2010b.

Hardalupas, Y., Taylor, A. M. K. P., and Whitelaw, J. H. Velocity and particle-flux characteristics of turbulent particle-laden jets. *Proceedings of the Royal Society of London. A. Mathematical and Physical Sciences*, 426(1870):31–78, 1989.

Harms, F., Leitl, B., Schatzmann, M., and Patnaik, G. Validating LES-based flow and dispersion models. *Journal of Wind Engineering and Industrial Aerodynamics*, 99 (4):289 – 295, 2011.

Heinrich, M. and Scherwinski, R. Propane releases under realistic conditions. determination of gas concentrations considering obstacles. Technical Report 123UIOO780, Technischer Uberwachungs-Verein Nord-deutschland, 1990.

Hervieu, E. and Veneau, T. Experimental determination of the droplet size and velocity distributions at the exit of the bottom discharge pipe of a liquefied propane storage tank during a sudden blowdown. *Journal of Loss Prevention in the Process Industries*, 9(6):413 – 425, 1996.

Hjertager, B., Fuhre, K., Parker, S., and Bakke, J. Flame acceleration of propane-air in a large-scale obstructed tube. *Progress in Astronautics and Aeronautics*, 94:504 – 522, 1984.

Hjertager, B., Bjørkhaug, M., and Fuhre, K. Explosion propagation of non-homogeneous methane—air clouds inside an obstructed 50 m^3 vented vessel. *Journal of Hazardous Materials*, 19(2):139 – 153, 1988a.

Hjertager, B., Fuhre, K., and Bjørkhaug, M. Gas explosion experiments in 1:33 and 1:5 scale offshore separator and compressor modules using stoichiometric homogeneous fuel/air clouds. *Journal of Loss Prevention in the Process Industries*, 1(4):197 – 205, 1988b.

Hjertager, B. H. Computer simulation of turbulent reactive gas dynamics. *Modeling, Identification and Control*, 5(4):211 – 236, 1985.

Hjertager, B. H. Three-dimensional modelling of flow, heat transfer, and combustion. In *Handbook of Heat and Mass Transfer*, pages 1303–1350. Gulf Publishing Company, Houston, 1986.

Hubbard, G., Denny, V., and Mills, A. Droplet evaporation: Effects of transients and variable properties. *International Journal of Heat and Mass Transfer*, 18(9):1003 – 1008, 1975.

Hussein, H. J., Capp, S. P., and George, W. K. Velocity measurements in a high-reynolds-number, momentum-conserving, axisymmetric, turbulent jet. *Journal of Fluid Mechanics*, 258:31–75, 1994.

Ichard, M. and Melheim, J. Dispersion of heavy particles in turbulent-like flows. In *7th International Conference on Multiphase Flow*, May 30-June 4 2010. Tampa, FL, USA.

Ichard, M., Hansen, O., Middha, P., Royle, M., Willoughby, D., and Gavelli, F. CFD computations of liquid hydrogen releases. In *Fourth International Conference on Hydrogen Safety*, 2011. San Francisco, California, 12-14 September 2011: 13 pp.

Ivings, M., Jagger, S., Lea, C., and Webber, D. Evaluating vapor dispersion models for safety analysis of LNG facilities. Technical Report MSU/2007/04, Health and Safety Laboratory, London, United Kingdom, 2007.

Johnson, D. and Woodward, J. *Release: a model with data to predict aerosol rainout in accidental releases*. A CCPS concept book. American Institute of Chemical Engineers, 1999. ISBN 9780816907458.

Jones, W. and Launder, B. The prediction of laminarization with a two-equation model of turbulence. *International Journal of Heat and Mass Transfer*, 15(2):301 – 314, 1972.

Kay, P. J., Bowen, P. J., and Witlox, H. W. Sub-cooled and flashing liquid jets and droplet dispersion II. scaled experiments and derivation of droplet size correlations. *Journal of Loss Prevention in the Process Industries*, 23(6):849 – 856, 2010.

Koopman, R., Cederwall, R., Ermak, D., Jr., H. G., Hogan, W., McClure, J., McRae, T., Morgan, D., Rodean, H., and Shinn, J. Analysis of burro series $40 - m^3$ LNG spill experiments. *Journal of Hazardous Materials*, 6(1–2):43 – 83, 1982a.

Koopman, R. P. and Ermak, D. L. Lessons learned from LNG safety research. *Journal of Hazardous Materials*, 140(3):412 – 428, 2007.

Koopman, R. P., Baker, J., Cederwall, R. T., Goldwire, H. C., Hogan, W. J., and Kamppinen, L. M. Burro series data report: LLNL/NWC 1980 lng spill tests, vols 1-2. Technical Report UCID-19075, Lawrence Livermore National Laboratory., 1982b.

Kukkonen, J., Kulmala, M., Nikmo, J., Vesala, T., Webber, D., and Wren, T. The homogeneous equilibrium approximation in models of aerosol cloud dispersion. *Atmospheric Environment*, 28(17):2763 – 2776, 1994.

Kuznetsov, V. and Vitovskii, O. Evaporation waves in a metastable single-component liquid. *Journal of Engineering Thermophysics*, 16:169–174, 2007.

Langevin, P. Sur la theorie du mouvement brownien. *C. R. Acad. Sci. (Paris)*, 146: 530–533, 1908.

Launder, B. E. and Sharma, B. I. Application of the energy-dissipation model of turbulence to the calculation of flow near a spinning disc. *Letters Heat Mass Transfer*, 1:131–137, 1974.

Launder, B. E., Morse, A. P., Rodi, W., and Spalding, D. B. The prediction of free shear flows - a comparison of six turbulence models. Technical Report SP-311, NASA, 1972.

Leung, J. C. A generalized correlation for one-component homogeneous equilibrium flashing choked flow. *AIChE Journal*, 32(10):1743–1746, 1986.

Leung, J. C. and Grolmes, M. A. A generalized correlation for flashing choked flow of initially subcooled liquid. *AIChE Journal*, 34(4):688–691, 1988.

Lienhard, J. H. and Day, J. B. The breakup of superheated liquid jets. *Journal of Basic Engineering*, 92(3):515–521, 1970.

Loth, E. Numerical approaches for motion of dispersed particles, droplets and bubbles. *Progress in Energy and Combustion Science*, 26(3):161 – 223, 2000.

MacInnes, J. M. and Bracco, F. V. Stochastic particle dispersion modeling and the tracer-particle limit. *Physics of Fluids A: Fluid Dynamics*, 4(12):2809–2824, 1992.

Mandø, M., Lightstone, M., Rosendahl, L., Yin, C., and Sørensen, H. Turbulence modulation in dilute particle-laden flow. *International Journal of Heat and Fluid Flow*, 30(2):331 – 338, 2009.

Mashayek, F. and Pandya, R. Analytical description of particle/droplet-laden turbulent flows. *Progress in Energy and Combustion Science*, 29(4):329 – 378, 2003.

Maxey, M. R. and Riley, J. J. Equation of motion for a small rigid sphere in a nonuniform flow. *Physics of Fluids*, 26(4):883–889, 1983.

McDonell, V. G. Detailed dataset: PDI and IRES measurements in methanol sprays under reacting and non-reacting conditions: case A non-reacting simplex spray. Technical Report UCI-ARTR-90-17A, University of California, Irvine, CA, USA, 1990.

McDonell, V. G. and Samuelsen, G. S. An experimental data base for the computational fluid dynamics of reacting and nonreacting methanol sprays. *Journal of Fluids Engineering*, 117(1):145–153, 1995.

McGuirk, J. J. and Rodi, W. The calculation of three-dimensional turbulent free jets. In *1st Symposium on Turbulent Shear Flows*, pages 71–83, 1979.

Melheim, J., Ichard, M., and Storvik, I. Spill modeling in FLACS. Technical report, GexCon AS, 2008.

Mi, J., Nobes, D. S., and Nathan, G. J. Influence of jet exit conditions on the passive scalar field of an axisymmetric free jet. *Journal of Fluid Mechanics*, 432:91–125, 2001.

Middha, P., Hansen, O. R., and Storvik, I. E. Validation of CFD-model for hydrogen dispersion. *Journal of Loss Prevention in the Process Industries*, 22(6):1034 – 1038, 2009.

Middha, P., Ichard, M., and Arntzen, B. J. Validation of CFD modelling of LH_2 spread and evaporation against large-scale spill experiments. *International Journal of Hydrogen Energy*, 36(3):2620 – 2627, 2011.

Minier, J.-P. and Peirano, E. The pdf approach to turbulent polydispersed two-phase flows. *Physics Reports*, 352(1–3):1 – 214, 2001.

Minier, J.-P. and Pozorski, J. Derivation of a PDF model for turbulent flows based on principles from statistical physics. *Physics of Fluids*, 9(6):1748–1753, 1997.

Minier, J. P., Peirano, E., and Chibbaro, S. Weak first and second order numerical schemes for stochastic differential equations appearing in lagrangian two-phase flow modeling. *Monte Carlo Methods and Appl.*, 9:93–133, 2003.

Moen, I., Donato, M., Knystautas, R., and Lee, J. Flame acceleration due to turbulence produced by obstacles. *Combustion and Flame*, 39(1):21 – 32, 1980.

Moncalvo, D. and Friedel, L. A simple, explicit formula for the critical pressure of homogenous two-phase nozzle flows. *Journal of Loss Prevention in the Process Industries*, 23(1):178 – 182, 2010.

Morse, A. P. *Axisymmetric turbulent shear flows with and without swirl*. PhD thesis, London University, United Kingdom, 1977.

MRS. The prediction of single and two-phase release rates. Technical Report OTI92587, Document prepared by The steel Construction Institute for the Health and Safety Executive, London, United Kingdom, 1992.

NIOSH. Ammonia. `http://www.cdc.gov/niosh/ershdb/EmergencyResponseCard_29750013.html`, 2008.

Oesterlé, B. On heavy particle dispersion in turbulent shear flows: 3-d analysis of the effects of crossing trajectories. *Boundary-Layer Meteorology*, 130:71–95, 2009.

Oseen, C. W. *Neuer methoden and engebnisse inder hydidynamic*. Leipzig: Acd. Verglasgesellschaft, 1927.

Panchapakesan, N. R. and Lumley, J. L. Turbulence measurements in axisymmetric jets of air and helium. Part 1. air jet. *Journal of Fluid Mechanics*, 246:197–223, 1993a.

Panchapakesan, N. R. and Lumley, J. L. Turbulence measurements in axisymmetric jets of air and helium. Part 2. helium jet. *Journal of Fluid Mechanics*, 246:225–247, 1993b.

Papanicolaou, P. N. and List, E. J. Investigations of round vertical turbulent buoyant jets. *Journal of Fluid Mechanics*, 195:341–391, 1988.

Pasquill, F. The estimation of the dispersion of windborn material. *Meteorol. Mag.*, 90: 33 – 49, 1961.

Pattison, M., Martini, R., and Banerjee, S. Modelling of dispersion of two-phase releases: Part 2—numerical solution scheme and validation. *Process Safety and Environmental Protection*, 76(1):41 – 49, 1998a.

Pattison, M., Martini, R., Banerjee, S., and Hewitt, G. Modelling of dispersion of two-phase releases: Part 1—conservation equations and closure relationships. *Process Safety and Environmental Protection*, 76(1):31 – 40, 1998b.

Peirano, E., Chibbaro, S., Pozorski, J., and Minier, J.-P. Mean-field/PDF numerical approach for polydispersed turbulent two-phase flows. *Progress in Energy and Combustion Science*, 32(3):315 – 371, 2006.

Polanco, G., Holdø, A. E., and Munday, G. General review of flashing jet studies. *Journal of Hazardous Materials*, 173(1–3):2 – 18, 2010.

Pope, S. *Turbulent flows*. Cambridge University Press, 2000. ISBN 9780521598866.

Pope, S. B. An explanation of the turbulent round-jet/plane-jet anomaly. *AIAA Journal*, 16:279–281, 1978.

Pope, S. B. PDF methods for turbulent reactive flows. *Progress in Energy and Combustion Science*, 11(2):119 – 192, 1985.

Ramsdale, S. A. and Tickle, G. A. Review of RELEASE rainout model and CCPS data. Technical Report CRR 277/2000, Health and Safety Executive, London, United Kingdom, 2000.

Richards, C. D. and Pitts, W. M. Global density effects on the self-preservation behaviour of turbulent free jets. *Journal of Fluid Mechanics*, 254:417–435, 1993.

Richardson, S., Saville, G., Fisher, S., Meredith, A., and Dix, M. Experimental determination of two-phase flow rates of hydrocarbons through restrictions. *Process Safety and Environmental Protection*, 84(1):40 – 53, 2006.

Rodi, W. and for Hydraulic Research, I. A. *Turbulence models and their application in hydraulics: a state-of-the art review*. Monograph series. A.A. Balkema, 1993. ISBN 9789054101505.

Salim, S. M., Buccolieri, R., Chan, A., and Sabatino, S. D. Numerical simulation of atmospheric pollutant dispersion in an urban street canyon: Comparison between RANS and LES. *Journal of Wind Engineering and Industrial Aerodynamics*, 99 (2–3):103 – 113, 2011.

Salvesen, H. C. Modeling release of liquefied gas under high pressure. Technical Report CMR-95-F20062, Christian Michelsen Research, Bergen, Norway, 1995.

Saurel, R., Petitpas, F., and Abgrall, R. Modelling phase transition in metastable liquids: application to cavitating and flashing flows. *Journal of Fluid Mechanics*, 607:313–350, 2008.

Scardovelli, R. and Zaleski, S. Direct numerical simulation of free-surface and interfacial flow. *Annual Review of Fluid Mechanics*, 31(1):567–603, 1999.

Sheen, H., Jou, B., and Lee, Y. Effect of particle size on a two-phase turbulent jet. *Experimental Thermal and Fluid Science*, 8(4):315 – 327, 1994.

Sher, E., Bar Kohany, T., and Rashkovan, A. Flash-boiling atomization. *Progress in Energy and Combustion Science*, 34(4):417 – 439, 2008.

Simoes-Moreira, J. R. Oblique evaporation waves. *Shock Waves*, 10:229–234, 2000.

Simoes-Moreira, J. R. and Bullard, C. W. Pressure drop and flashing mechanisms in refrigerant expansion devices. *International Journal of Refrigeration*, 26(7):840 – 848, 2003.

Simoes-Moreira, J. R. and Shepherd, J. E. Evaporation waves in superheated dodecane. *Journal of Fluid Mechanics*, 382:63–86, 1999.

Simoes-Moreira, J. R., Vieira, M. M., and Angelo, A. Highly expanded flashing liquid jets. *Journal of Thermophysics and Heat Transfer*, 16(3), 2002.

Simonin, O., Deutsch, E., and Minier, J. P. Eulerian prediction of the fluid/particle correlated motion in turbulent two-phase flows. *Applied Scientific Research*, 51: 275–283, 1993.

Sirignano, W. *Fluid dynamics and transport of droplets and sprays*. Cambridge University Press, 1999. ISBN 9780521630368.

Snyder, W. H. and Lumley, J. L. Some measurements of particle velocity autocorrelation functions in a turbulent flow. *Journal of Fluid Mechanics*, 48(01): 41–71, 1971.

Sowa, W. A. Interpreting mean drop diameters using distribution moments. *Atomization and Sprays*, 2(1):1–15, 1992.

Sozzi, G. L. and Sutherland, W. A. Critical flow of saturated and subcooled water at high pressure. In *Nonequilibrium Two-phase Flows, ASHE Winter Annual Meeting*, 1975. Houston, TX, USA.

Storwold, D. P., Argenta, E. P., White, J. M., Pace, J. C., and Fox, S. B. The jack rabbit test program trial summary. In *91st American Meteorological Society Annual Meeting, Special Symposium on Applications of Air Pollution Meteorology*, January 23-27, 2011. Seattle, WA, USA.

Stull, R. *An introduction to boundary layer meteorology*. Atmospheric sciences library. Kluwer Academic Publishers, 1988. ISBN 9789027727688.

Tchen, C. M. *Mean value and correlation problems connected with the motion of small particles suspended in a turbulent fluid*. PhD thesis, University of Delft-Martinus Nijhoff, The Hague, Netherland, 1947.

Tryggvason, G., Bunner, B., Esmaeeli, A., Juric, D., Al-Rawahi, N., Tauber, W., Han, J., Nas, S., and Jan, Y.-J. A front-tracking method for the computations of multiphase flow. *Journal of Computational Physics*, 169(2):708 – 759, 2001.

Uchida, H. and Nariari, H. Discharge of saturated water through pipes and orifices. In *Proceedings of the 3rd International Heat Transfer Conference, vol. 5*, pages 1–12, 1966. Chicago, AssIChE, New York, NY.

Uddin, M. and Pollard, A. Self-similarity of coflowing jets: The virtual origin. *Physics of Fluids*, 19(6):068103, 2007.

van Den Akker, H., Snoey, H., and Spoelstra, H. Discharges of pressurized liquefied gases through apertures and pipes. In *Proceedings of 4th International Symposium, Loss Prevention and Safety Promotion in the Process Industries*, 1983. Harrogate, United Kingdom.

van den Bosch, C. and Weterings, R. *Methods for the calculation of physical effects due to the release of hazardous materials (liquids and gases)*. TNO yellow book (3rd ed.). The Hague, The Netherlands: TNO, 1997.

van Wingerden, C. Experimental investigation into the strength of blast waves generated by vapour cloud explosions in congested areas. In *Sixth Int. Symp. on Loss Prevention and Safety Promotion in the Process Industries*, June 19-22, 1989. Oslo, Norway.

Versteeg, H. and Malalasekera, W. *An introduction to computational fluid dynamics: the finite volume method*. Pearson Education Ltd., 2007. ISBN 9780131274983.

Walpot, R. J. E., van der Geld, C. W. M., and Kuerten, J. G. M. Determination of the coefficients of langevin models for inhomogeneous turbulent flows by three-dimensional particle tracking velocimetry and direct numerical simulation. *Physics of Fluids*, 19(4):045102, 2007.

Wang, P., Fröhlich, J., Michelassi, V., and Rodi, W. Large-eddy simulation of variable-density turbulent axisymmetric jets. *International Journal of Heat and Fluid Flow*, 29(3):654 – 664, 2008.

Wilcox, D. C. *Turbulence Modeling for CFD*. DCW Industries Inc., La Cañada, CA, 1993.

Witlox, H. W. and Bowen, P. J. Flashing liquid jets and two-phase dispersion a review. Technical Report HSE-CRR-403/2001, Health and Safety Executive, London, United Kingdom, 2002.

Witlox, H. W., Harper, M., Bowen, P., and Cleary, V. Flashing liquid jets and two-phase droplet dispersion: II. comparison and validation of droplet size and rainout formulations. *Journal of Hazardous Materials*, 142(3):797 – 809, 2007.

Witlox, H. W., Harper, M., Oke, A., Bowen, P. J., and Kay, P. Sub-cooled and flashing liquid jets and droplet dispersion i. overview and model implementation/validation. *Journal of Loss Prevention in the Process Industries*, 23(6):831 – 842, 2010.

Woodward, J. L. Validation of two models for discharge rate. *Journal of Hazardous Materials*, 170(1):219 – 229, 2009.

Woodward, J. L. and Papadourakis, A. Reassessment and reevaluation of rainout and drop size correlation for an aerosol jet. *Journal of Hazardous Materials*, 44(2–3): 209 – 230, 1995.

Woodward, J. L., Cook, J., and Papadourakis, A. Modeling and validation of a dispersing aerosol jet. *Journal of Hazardous Materials*, 44(2–3):185 – 207, 1995.

Wurtz, J., Bartzis, J., Venetsanos, A., Andronopoulos, S., Statharas, J., and Nijsing, R. A dense vapour dispersion code package for applications in the chemical and process industry. *Journal of Hazardous Materials*, 46(2–3):273 – 284, 1996.

Wygnanski, I. and Fiedler, H. Some measurements in the self-preserving jet. *Journal of Fluid Mechanics*, 38(03):577–612, 1969.

Yildiz, D., Rambaud, P., Vanbeeck, J., and Buchlin, J. A study on the dynamics of a flashing jet. Technical Report EAR0030/2002, von Karman Institute for Fluid Dynamics, 2004.